A Measurement of Forward-Backward Charge Asymmetry of Electron-Positron Pairs in Proton-Antiproton Collision at 1.96 TeV

by

Gregory Francisco Veramendi

B.S. (University of Rochester, New York) 2000

A dissertation submitted in partial satisfaction of the

requirements for the degree of

Doctor of Philosophy

in

Physics

in the

GRADUATE DIVISION

of the

UNIVERSITY OF CALIFORNIA, BERKELEY

Committee in Charge:

Professor Marjorie Shapiro, Co-chair
Professor Young-Kee Kim, Co-chair
Professor Robert Jacobsen
Professor Eugene E. Haller

Fall 2003

The dissertation of Gregory Francisco Veramendi is approved:

Co-chair Date

Co-chair Date

Date

Date

University of California, Berkeley

Fall 2003

Abstract

A Measurement of Forward-Backward Charge Asymmetry of Electron-Positron Pairs in Proton-Antiproton Collision at 1.96 TeV

by

Gregory Francisco Veramendi

Doctor of Philosophy in Physics

University of California, Berkeley

Professor Young-kee Kim, Co-chair

Professor Marjorie Shapiro, Co-chair

We present a measurement of the mass dependence of the forward-backward charge asymmetry for e^+e^- pairs resulting from γ^*/Z decays with mass $M_{ee} > 40$ GeV/c^2. The Run II data sample consists of 72 pb^{-1} of data, which was collected by the CDF detector in $\overline{p}p$ collisions at $\sqrt{s}$=1.96 TeV at the Fermilab Tevatron. The measurement is compared with predictions from the Standard Model.

Co-chair Date

Co-chair Date

This thesis is dedicated to

my wife, Maria Milagros Ruete Perez

Contents

List of Figures

List of Tables

Acknowledgments

When I think of the journey that got me to this point, I can't imagine how I ever made it! Were it not for the grace, patience, and support of so many people, I never could have.

I would like to thank my family for being supportive and always being so excited at each milestone that I have reached along the way. I am indebted to the Illinois Math and Science Academy, first of all for accepting me, and secondly for giving me that first spark of excitement about physics and working on experimental research.

I would like to thank Paul Tipton for taking me on as an undergrad the summer after my freshman year (1995), and introducing me for the first time to CDF. He has always given me the best, if occasionally cryptic, advice. His final advice for making a decision on graduate school was, "kill a cat, read the entrails, make a decision." It is through Paul that I knew I wanted to do HEP physics. I would also like to thank Richard Hughes and Brian Winer, who took me on to help them with the XFT. Their energy and enthusiasm taught me how to work in a large collaboration. The XFT work I did with them was probably my first real contribution to CDF.

I would like to thank the people who kept me sane through my first two years at Berkeley. Sudeep, Connie, Arun, Kirsten, "big" Mike, and others who spent countless nights working on problem sets and perfecting dart throwing techniques with me. I am forever indebted to Anne Takizawa and Donna Sakima, the graduate advisers; were it not for their extraordinary efforts to keep me in the Berkeley system, I would not have made it very far! To the Newman crew, especially Ed, Gil, and Amie, for their wonderful friendships and good times. They made my two years in Berkeley among the most special of my life.

I am indebted to the LBL group for the wealth of experiences that I have had as a graduate student and everything they have taught me. I had the opportunity to work with Tony Affolder, and others on the COT field sheet construction. I also worked with Aaron Dominguez, Jason Nielsen, Maurice Garcia-Sciveres, and others on the SVX hybrid construction. The LBL group has always been very constructive and given great advice and ideas on my analysis and all the different projects that I have worked on. I owe a special thanks to my fellow LBL graduate students, Erik Brubaker, Adam Gibson, Hung-Chung Fang, and Henri Bachacou. They were always there to help me figure something out, or just hang out. I owe much to Erik and Adam, who worked closely with me on this analysis in its early stages, and who were always willing to help me with the documentation, not the most exciting task. Last, but not least, thanks to Lina Galtieri, who was always so supportive, and encouraging. She helped, in no small way, to make our group almost feel like a family.

This analysis could not exist were it not for my CDF collaborators. It is impossible to name everyone who has taught me all that I know about the detector and collider physics. All of those who have spent so much of their time working on building, commissioning, and maintaining the detector. This analysis really belongs to all of them. There are a few people who played important roles in my time as a graduate student at CDF. If there is one thing I was involved in at CDF, that was most formational and that I am most proud of, it was being co-convener of the ETF group with Eva Halkiadakis. I'm not sure we had any idea what we were getting into when Pierre and Willis told us to form an electron group, but I am very grateful that I was able to do it with Eva. She was a great person to work with, and it would not have been the same or as successful had it been someone else. In addition, it would not have been possible, if it hadn't been for the advice and tutelage of the resident electron experts: Larry Nodulman, Willis Sakumoto, Barry Wicklund, Bob Wagner, and others from whom we learned all we know about electrons. I can't forget Sarah Demers, who also helped me keep my sanity when dealing with the trigger. I'd like to thank Kaori Maeshima for being a good friend and for making working on the consumers fun! I must thank Pasha Murat for being such a great and amusing neighbor for the last few years. He was always willing to take time out of his overflowing schedule to help me out and share his amusements with me. Finally, I owe a great deal of gratitude to my partner-in-crime (and friend), Giulia Manca.

She was always willing to work on different projects with me. She was always there to see how I was doing, and make sure I didn't get lost, a true friend.

Finally, I owe my graduate career to Young-kee Kim, my adviser. She was there from the day I got off the plane when visiting Berkeley until now sitting with me through marathon editing sessions. My first impression of her was my amazement that she was always willing to insert herself wherever necessary to make CDF a success, whether it was replacing a technician when someone was sick, or taking owl shifts during Christmas when no one else was willing to do it. Her drive, motivation, and intuition are large part of the reason that I became involved in so many different aspects of the experiment, and learned so much. I knew when choosing a graduate school that your graduate adviser is the single most important factor in your success and happiness as a graduate student. I have never doubted that I made the right choice.

I must thank one more person and that is my wife, Mila. We met when I was already two years into the process. Her role in my life has been essential to my success. Coming to live in a foreign country was hard enough, but having to be patient with my working long hours has demonstrated her resilience. She has been supportive every moment of this journey, and always comes to the rescue when I needed it. Gracias!

Chapter 1

Introduction

It was in 1896 that H. Becquerel accidentally discovered the weak interaction when he serendipitously placed a sample of uranium ore and a photographic plate in the same drawer. He recognized that the fogging of the photographic plate was caused by the ore, and later found that the ore was emitting β particles. It wasn't until 60 years later that Glashow [1], Salam [2], and Weinberg [3] developed the modern concept of the W and Z bosons and unified the weak and electromagnetic forces. Finally, in 1973 Weak Neutral Currents (WNC) were discovered essentially simultaneously by two neutrino experiments at CERN [4] and Fermilab [5], and within a few years the first measurements of $\sin^2\theta_W$ was made [6].

The unified electroweak theory describes the interactions of the spin-$\frac{1}{2}$ fermions (leptons and quarks) and the spin-1 gauge bosons (photon, Z, and $W^{\pm}$). To describe the neutral current interactions, the physical photon (A^0), and Z boson (Z^0) fields are written as a linear combination of the neutral gauge bosons W_3^0 and B, which correspond to the SU(2) and U(1) groups respectively, as follows

$$Z^0 = \cos\theta_W W_3^0 - \sin\theta_W B^0 \tag{1.1}$$

$$A^0 = \sin\theta_W W_3^0 + \sin\theta_W B^0 \tag{1.2}$$

where θ_W is the Weinberg or weak mixing angle. The theory unified the weak and electromagnetic forces, but left the fermions and bosons massless. A solution to this problem is given by the Higgs Mechanism, where the fermions, W and Z bosons acquire mass through the introduction of a weak doublet of scalar bosons, while the photon remains massless. Through the process of spontaneous local symmetry breaking, three members of the Higgs doublet form the longitudinal spin states of the massive gauge bosons. This leaves one massive neutral scalar particle, the Higgs boson H. The fermions acquire masses through fermion-Higgs field Yukawa couplings. Unfortunately, the theory makes no prediction as to the masses of the fermions or the Yukawa couplings, or the mass of the Higgs scalar (m_H). The weak mixing angle becomes an important parameter of the Standard Model (SM). At tree level it relates the masses of the W and Z bosons, $\sin^2\theta_W = 1 - m_W^2/m_Z^2$, and relates the couplings of the W and Z to the coupling of the photon, $e = g\sin\theta_W = g'\cos\theta_W$.

Experiments at CERN, SLAC, and Fermilab have provided increasingly precise tests [7, 8] of the SM. The LEP e^+e^-synchrotron collider at CERN took data at the Z pole between 1989 and 1995 (LEP 1 phase). There were lineshape scans, in which data were taken at a series of energy settings within ±3 GeV of the Z-pole. Over 200 cross-section and asymmetry measurements (see Section 1.1) were made among the four experiments, where 15.5 million hadronic Z decays and 1.7 million leptonic decays were recorded. The Stanford Linear e^+e^- Collider took data also at the Z pole between 1992 and 1998, and had polarized beams giving them unique opportunities to make precise asymmetry measurements. The Tevatron $\overline{p}p$ collider running at $\sqrt{s} = 1.8$ TeV was able to make precision measurements of the W mass and width, and uniquely measure the top mass. The LEP 2 phase, which took data with center of mass energies above the W-boson pair-production threshold (161 GeV), made a precision measurement of the W mass as well and placed a lower limit on the Higgs boson mass. The combination of the measurements coming from these large collider experiments and other smaller experiments have confirmed the SM to unprecedented accuracy (see Figure 1.1).

1.1 The Forward-Backward charge asymmetry

The electroweak interactions studied in collider experiments involve the scattering of two fermions i.e. $f_1 f_2 \to f_3 f_4$ (where $f_1, f_2 = e^+e^-$ or $\bar{q}q$, the incoming particles, and f_3, f_4 are the scattered fermions.). For the case of a neutral current interaction involving charged particles, both γ^* and Z exchange are possible, so there is a $\gamma^* - Z$ interference term. This latter term has an energy dependence proportional to the difference $(s - m_Z^2)$, where $\sqrt{s}$ is the center of mass energy. So this interference term and the asymmetry which depends on it changes sign in going from below to above the Z-pole. The presence of both vector and axial-vector couplings of electroweak bosons to fermions in the process $\bar{f}f \to Z/\gamma^* \to \ell^+\ell^-$ gives rise to an asymmetry in

Figure 1.1: *Pull distribution for the global electroweak fit [8].*

the polar angle with respect to the beam axis of the ℓ^- momentum in the rest frame of the lepton pair. At tree level, the angular differential cross section in the center of mass frame takes the form

$$\frac{d\sigma(\bar{f}f \to Z/\gamma^* \to \ell^+\ell^-)}{d\cos\theta} = A(1+\cos^2\theta) + B\cos\theta \tag{1.3}$$

where θ is the emission angle of the lepton (anti-lepton) relative to the fermion (anti-fermion) momentum in the center-of-mass frame, and A and B are functions dependent on the weak isospin and charge of the incoming fermions (f_1, f_2) and $Q^2 = M_{\ell\ell}^2$ of the interaction. If the number of forward events, N_F, are defined as the number of events with positive $\cos\theta$ and the number of backward events, N_B, as the number of events with negative $\cos\theta$, then the forward-backward charge asymmetry A_{FB} is:

$$\begin{aligned} A_{FB} &= \frac{N_F - N_B}{N_F + N_B} \\ &= \frac{\sigma(\cos\theta > 0) - \sigma(\cos\theta < 0)}{\sigma(\cos\theta > 0) + \sigma(\cos\theta < 0)} \\ &= \frac{3B}{8A} \end{aligned} \tag{1.4}$$

and A_{FB} is a direct probe of the relative strengths of the vector and axial-vector couplings over the range of Q^2 being considered.

By colliding polarized electron beams, the vector and axial-vector couplings can be measured directly, by measuring

$$A_{LR} = \frac{\sigma_L - \sigma_R}{\sigma_L + \sigma_R} = \mathcal{A}_e = \frac{2v_e a_e}{(v_e^2 + a_e^2)} \tag{1.5}$$

where σ_L (σ_R) is the total cross-section for the left-(right-)handed polarized incident electron beam, v_f (a_f) are the vector (axial-vector) couplings of the incoming fermion, and $\mathcal{A}_e$ is the left-right asymmetry. The vector and axial-vector couplings can be related to the effective weak mixing angle by

$$\frac{v_f}{a_f} = 1 - 4|q_f| \sin^2 \theta^f_{eff}. \tag{1.6}$$

The high values of polarization ($P_e \simeq 70 - 80\%$) achieved at the Stanford Linear Collider (SLC) allowed the Stanford Linear Detector (SLD) experiment to make the single most precise determinations of $\mathcal{A}_e$ (Figure 1.1) and $\sin^2 \theta^{lept}_{eff}$ (Figure 1.2).

Although the LEP accelerator had unpolarized beams, the LEP experiments had much larger data samples (15.5M (LEP) versus 0.55M (SLD) hadronic Z events). At LEP and SLD, the pole asymmetry ($A^{0,f}_{FB}$) in Equation 1.4 is measured. For e^+e^- colliders $A^{0,f}_{FB}$ reduces to

$$A^{0,f}_{FB} = \frac{3}{4}\mathcal{A}_e\mathcal{A}_f \tag{1.7}$$

In this way, both SLC and LEP measured the pole asymmetry for the three lepton species, light quarks, c quarks, and b quarks. In addition, it is possible to measure the polarization

$$\mathcal{P}_\tau = \frac{\sigma_L - \sigma_R}{\sigma_L + \sigma_R} \tag{1.8}$$

of the τ lepton from the angular distribution of its decay products. When averaged over all production angles, $\mathcal{P}_\tau$ gives a measurement of $\mathcal{A}_\tau$. Measurements of $\mathcal{P}_\tau(\cos\theta)$ (where θ is the angle between the incoming e^- and outgoing τ^-) provide nearly independent determinations of both $\mathcal{A}_\tau$ and $\mathcal{A}_e$. All of these methods for measuring the Neutral Current couplings are summarized in Figure 1.2 as measurements of $\sin^2\theta_{eff}^{lept}$ through Equation 1.6. Measurements of the asymmetries were also made at LEP 2 energies (130-209 GeV), and were found to be compatible with the SM (see Figure 1.3).

The analogous process at the Tevatron, $\bar{q}q \rightarrow Z/\gamma^* \rightarrow \ell^+\ell^-$, is called the Drell-Yan[1] process [9]. Extra complications arise for a $\bar{p}p$ collision. The center of mass in a hadron collider is given by the formula, $\hat{s} = p^2 = x_1 x_2 s$, where $x_{1,2}$ are the momentum fractions of the proton and antiproton carried by the quarks. The momentum distribution of the quarks and gluons in the proton is described by functions called Parton Distribution Functions (PDFs). Calculating the kinematics of the interaction involves convoluting the hard parton interaction with the q and $\bar{q}$ density functions.

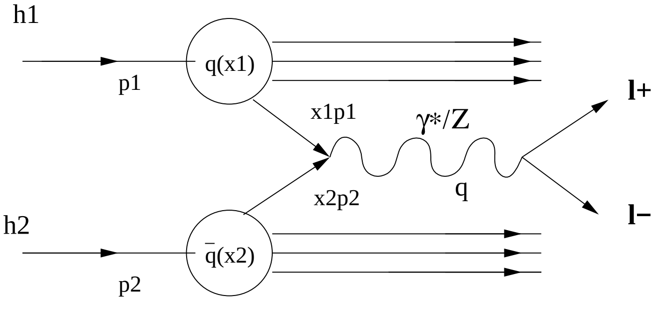

[1]

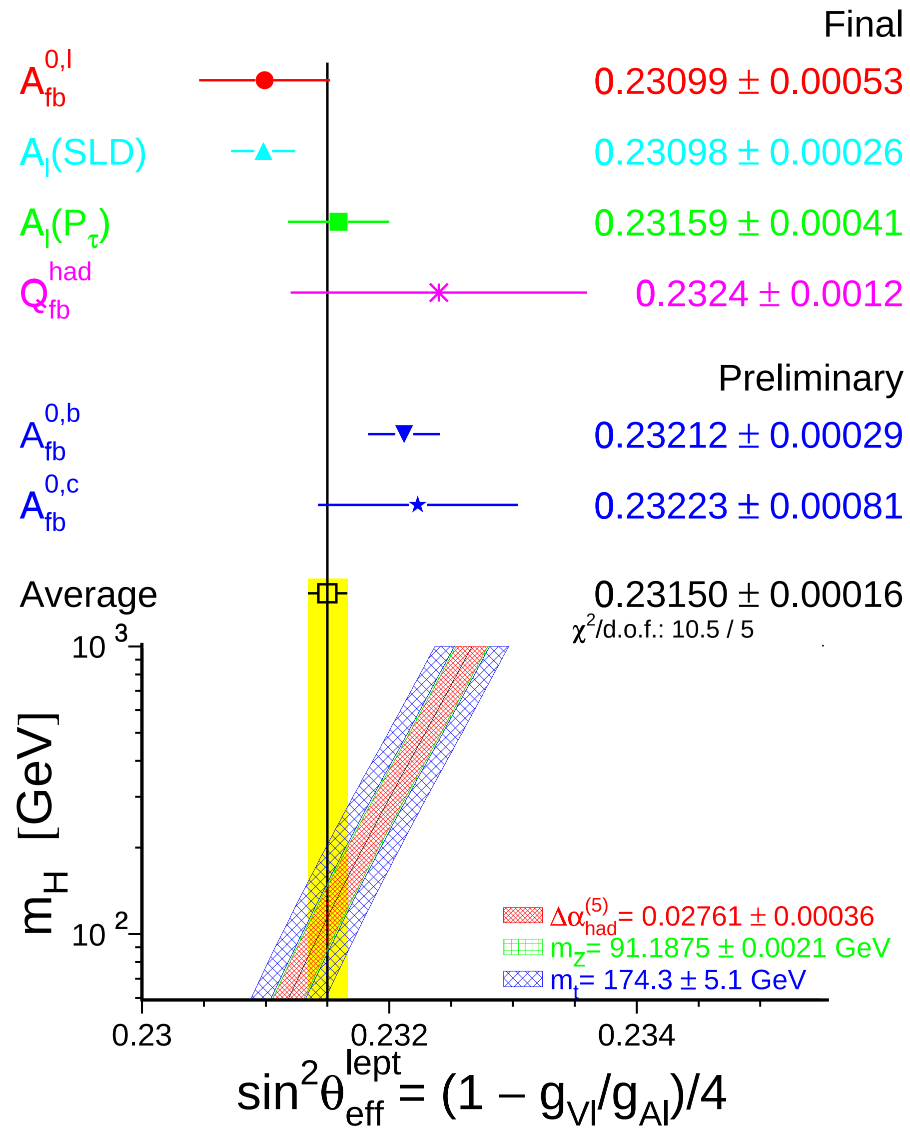

Figure 1.2: *Comparison of the determinations of* $\sin^2\theta_{eff}^{lept}$ *from LEP and SLC. Also shown is the SM expectation as a function of* m_H*, with the bands showing the uncertainties from other SM parameters.*

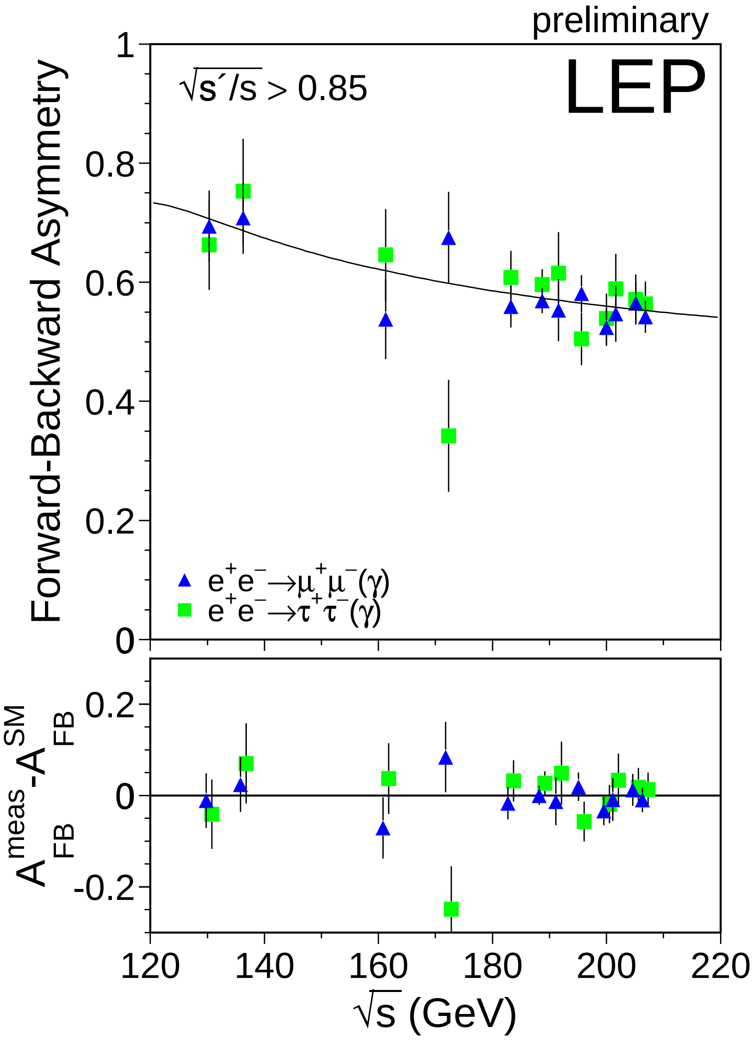

Figure 1.3: *Combined measurements of* A_{FB} *as a function of center of mass energy for* $\mu^+\mu^-$ *and* $\tau^+\tau^-$ *final states at the LEP II* e^+e^- *collider. The SM prediction, computed with ZFITTER, is shown as a curve. The lower plots show the difference between the measurements and the predictions for* A_{FB}.

So the momentum distributions of the various flavors of valence and sea quarks must be taken into account, and higher order QCD effects (e.g. initial state gluon radiation) must be included. Theoretical calculations [10] show that while higher order QCD effects strongly enhance the overall production cross section, they are not expected to significantly alter the angular distribution of the decay products. Therefore, to predict A_{FB} for a given range of $M_{\ell\ell}$, it is sufficient to convolve the tree-level differential cross section with a parton distribution function. The previous Collider Detector at Fermilab (CDF) measurement [11] is shown in Figure 1.4 with 110 pb^{-1} of data at $\sqrt{s} = 1.8$ TeV. Only the electron final state is considered, because the acceptance at CDF for μ and τ for $|\eta_{det}| > 1$ is limited. The interest in this measurement is in the high invariant mass (M_{ee}) region, above the region directly studied by LEP II. In order to compete with the LEP and SLC measurements at the Z pole, the Tevatron would have to accumulate 100 times the Run I dataset. Although there is a small discrepancy in the highest bin, the data are in good agreement with the SM predictions.

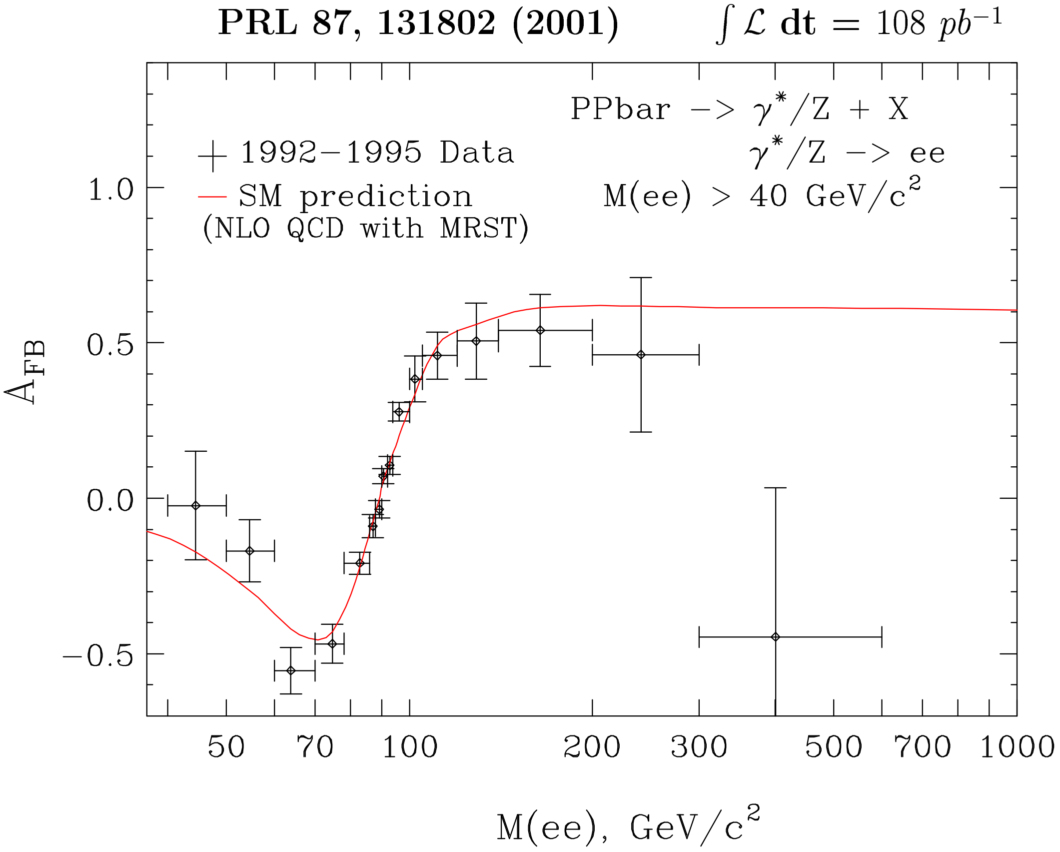

Figure 1.4: *A_{FB} as a function of center of mass energy from the Drell-Yan process from the CDF experiment for Run I.*

1.2 Beyond the Standard Model

Until recently, the measurements of electroweak observables gave very consistent fits with SM theory. Two $\geq 2.5\sigma$ measurements have evolved so that the Standard Model (SM) fit of the precision electroweak data has a poor confidence level, CL=0.02 [12]. The poor confidence level is dominated by two measurements. The measurement from LEP of $A_{fb}^{0,b}$ [8] is 2.4 σ from the fit, and the NuTeV measurement of $\sin^2\theta_W(\nu N)$ [13] is 2.9 σ from the fit (see Figure 1.1). One possibility is that the systematic uncertainty is underestimated for these two measurements. If the two measurements are ignored, then the CL of the global fit increases to 0.71, while at the same time giving a central Higgs mass of $m_H = 45$ GeV/c^2. But the CL drops to 0.05 when including the lower limit $m_H > 114 GeV$ [14] established by direct searches. Although there is general agreement between the experiment and theory, the fit has a low probability with or without the $A_{fb}^{0,b}$ and $\sin^2\theta_W(\nu N)$ measurements. The apparent discrepancy might be due to some combination of statistical and systematic fluctuations, or it may be a clue to new physics. The NuTeV experiment [13] probes a different energy scale than the study of on-shell Z boson decays at LEP I and SLC. One possible explanation is a Z' boson that mixes very little with the Z boson and would have very little effect on the LEP measurements but a significant effect on the NuTeV measurement [15].

The Standard Model has its own problems and limitations aside from comparisons with data. One of the four fundamental interactions, gravity, is not included. The Higgs mass receives radiative corrections that causes its mass to become unstable unless fine-tuning cancellations on the order of 10^{-13} occur (this is called the hierarchy problem). It is now known that neutrinos have mass, yet in the SM they are massless left-handed particles. There are a plethora of theories to solve many of these problems, but most sorely need experimental validation. Many of these theories predict new phenomena at the TeV scale, making the current experiments at the Tevatron, and the future experiments at the LHC very exciting.

Many theorists are looking for symmetries beyond the SM that will solve some of the problems with the theory, attempt to incorporate gravity, or both. Many of these extensions to the SM predict the existence of a new neutral gauge heavy boson, Z'. The existence of a Z' could lead to deviations of the A_{FB} and the cross section from that predicted in the standard model. We will concentrate on effects to the A_{FB}.

One family of theories which can predict the existence of a Z' is the family of grand unified theories (GUT), which attempt to unify the three interactions at the unification energy (typically 10^{15} GeV). $SU(2)$, $U(1)$, and $SU(3)$ symmetries could be incorporated into a more global gauge symmetry, SU(5) [16]. $SU(5)$ has no additional neutral gauge bosons, and is also excluded by precision data. $SU(5)$ may be part of a larger $SO(10)$ gauge group which does not contradict current experimental data, and predicts at least one extra neutral gauge boson [17]. Some string-theory models [18] suggest further embedding into an E_6 gauge group [19]. One of the possible breaking scenarios is

$$E_6 \rightarrow SO(10) \times U(1)_\Psi \rightarrow SU(5) \times U(1)_\chi \times U(1)_\Psi \tag{1.9}$$

The most general Z' within E_6 may be parametrized as

$$Z' = Z_\Psi \cos\theta + Z_\chi \sin\theta \tag{1.10}$$

where θ is the mixing angle and determines the coupling constants of the Z'. Assuming that the Z and Z' have very small mixing (due to LEP constraints), and that the Z' has a mass accessible to the Tevatron, its effect on the A_{FB} can be studied [20]. Figure 1.5 shows the A_{FB} when adding a 500 GeV/c^2 Z' with different mixing angles. E_6 may also break down to $SU(6)\times SU(2)_I$ ($\theta = \arctan(-\sqrt{5/3})$), where the subscript stands for "inert", since all gauge bosons of $SU(2)_I$ are neutral. The $I_{3I} = 0$ member of the $SU(2)_I$ triplet is called Z_I.

Other classes of theories also predict additional neutral gauge bosons. Extra Dimension theories try to solve the Hierarchy problem in the SM by lowering the Planck scale. Gauge bosons can exist in the extra dimension as Kaluza-Klein excitation states of the graviton [21]. The topcolor assisted Technicolor models also predict an extra neutral gauge boson [22]. Little Higgs [23, 24] is a class of theories of electroweak symmetry breaking, where additional extra neutral gauge bosons play a role in canceling the quadratic divergences of the SM. The simplest of these models, called the Littlest Higgs [24, 25], contains four extra gauge bosons.

In most models the masses of the extra gauge bosons are not constrained. Therefore A_{FB} constrains the properties of any additional non-Standard Model amplitudes contributing to $q\bar{q} \to \ell^+\ell^-$, and is complementary to a direct search for them via excesses in the total cross section. In addition, the Tevatron has the ability to probe much higher energies than were available at LEP II.

1.3 Strategy of Analysis

This analysis focuses on the dielectron decays of Z/γ^* bosons. The data sample has small background. The polar angle coverage of electrons is much better than that of muons, hence the dielectron decays yield a better measurement of the forward-backward charge asymmetry. The goal of this analysis is to measure A_{FB} as a function of the invariant mass of the Z/γ^* boson. Since the four momenta of the electrons are well measured, the invariant mass of the e^+e^- pair and the momentum of the Z/γ^* boson can be determined unambiguously within measurement uncertainties.

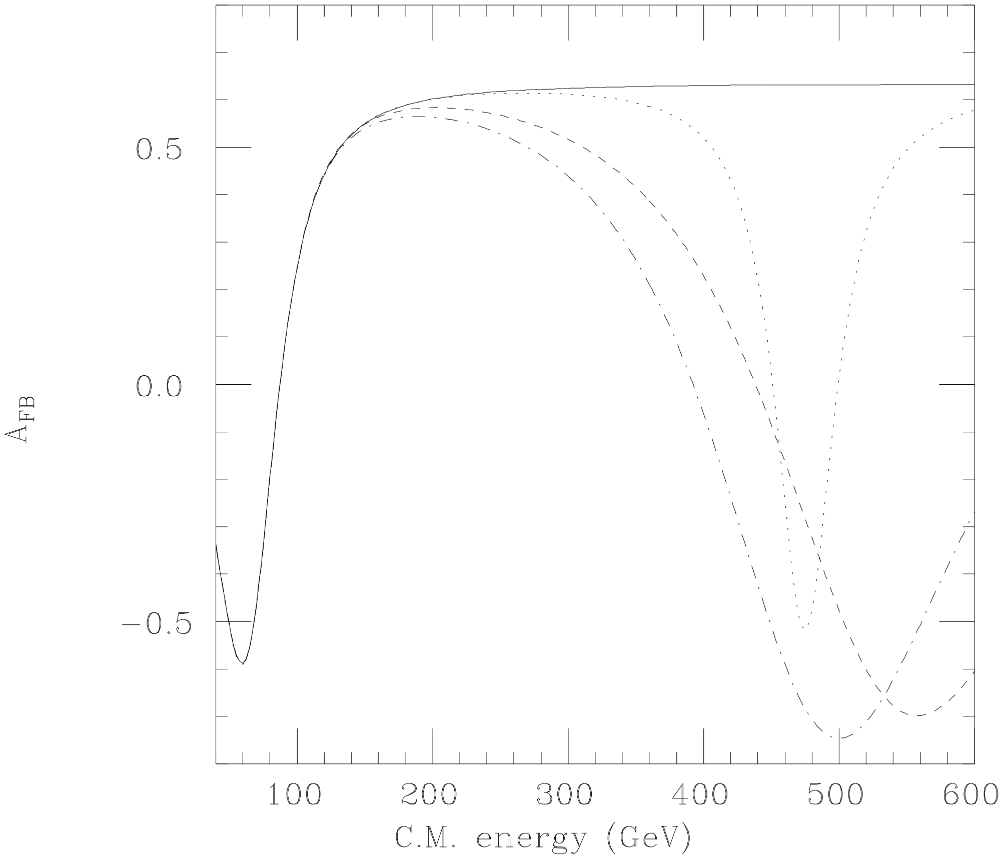

Figure 1.5: *Parton-level forward-backward asymmetries for* $\bar{d}d \to e^+e^-$ *when adding* Z' *with different mixing angles from an* E_6 *gauge group. Solid line: standard model. Dashed line: 500 GeV/*c^2 Z'_χ *added. Dotted line: 500 GeV/*c^2 Z'_Ψ *added. Dot-dashed line: 500 GeV/*c^2 Z'_I *added.*

When the incoming quarks participating in the Drell-Yan process have no transverse momentum relative to their parent baryons, θ in Equation (1.3) is determined unambiguously from the four-momenta of the electrons by calculating the angle that the electron makes with the proton beam in the center-of-mass frame of the electron-positron pair. When either of the incoming quarks has significant transverse momentum, however, there exists an ambiguity in the four momenta of the incoming quarks in the frame of the electron-positron pair, since one cannot determine the four momenta of the quark and anti-quark individually. The Collins-Soper formalism [26] is adopted to minimize the effects of the transverse momentum of the incoming quarks in Equation (1.3). In this formalism, the polar axis is defined as the bisector of the proton beam momentum and the negative of the anti-proton beam momentum when they are boosted into the center-of-mass frame of the electron-positron pair. The variable θ^* is defined as the angle between the electron and the polar axis. Let Q (Q_T) be the four momentum (transverse momentum) of the electron-positron pair, P_1 be the four momentum of the electron, and P_2 be the four momentum of the positron, all measured in the lab frame. Then $\cos\theta^*$ is given by

$$\cos\theta^* = \frac{2}{Q\sqrt{Q^2 + Q_T^2}}\,(P_1^+ P_2^- - P_1^- P_2^+) \tag{1.11}$$

where $P_i^{\pm} = \frac{1}{\sqrt{2}}(P_i^0 \pm P_i^3)$, and P^0 and P^3 represent energy and the longitudinal component of the momentum, respectively. The forward and backward events are defined using $\cos\theta^*$.

A_{FB} needs to be corrected for background contamination, kinematic acceptance (a_{kin}), geometric acceptance (a_{geom}), detector resolutions (a_{res}), internal and external bremsstrahlung (a_{rad}), and electron identification efficiency (ϵ_{ID}). The estimated number of forward and backward background events is subtracted from the data. The others, $(a_i^{\pm})_{sel}$, including the loss of events due to acceptance and efficiency and the shift in the dielectron invariant mass due to detector resolution and bremsstrahlung are calculated using Monte Carlo samples,

$$(a_i^{\pm})_{sel} = \frac{(N_i^{\pm})_{selected}}{(N_i^{\pm})_{generated}} = (a_i^{\pm})_{geom} * (a_i^{\pm})_{kin} * (a_i^{\pm})_{res} * (a_i^{\pm})_{rad} * (\epsilon_i^{\pm})_{ID}, \tag{1.12}$$

where $(N_i^+)_{generated}$ $[(N_i^-)_{generated}]$ is the number of forward [backward] events generated in the i-th mass bin, and $(N_i^+)_{selected}$ $[(N_i^-)_{selected}]$ is the number of forward [backward] events selected in the i-th mass bin. Equation (1.4) can then be rewritten:

$$A_{FB}^i = \frac{\left(\frac{d\sigma}{dM}\right)_i^+ - \left(\frac{d\sigma}{dM}\right)_i^-}{\left(\frac{d\sigma}{dM}\right)_i^+ + \left(\frac{d\sigma}{dM}\right)_i^-} \tag{1.13}$$

where

$$\left(\frac{d\sigma}{dM}\right)_i^{\pm} = \frac{(N_i^{\pm} - B_i^{\pm})}{\Delta M_i L (a_i^{\pm})_{sel}}. \tag{1.14}$$

In Equation (1.14), ΔM_i is the size of the i-th mass bin, and L is the luminosity. $N^+(N^-)$ and $B^+(B^-)$ are the number of candidate and estimated background events in the forward (backward) region, respectively. Canceling common factors, the forward-backward asymmetry can be written as

$$A^i_{FB} = \frac{\frac{N_i^+ - B_i^+}{(a_i^+)_{sel}} - \frac{N_i^- - B_i^-}{(a_i^-)_{sel}}}{\frac{N_i^+ - B_i^+}{(a_i^+)_{sel}} + \frac{N_i^- - B_i^-}{(a_i^-)_{sel}}}. \tag{1.15}$$

The uncertainties associated with systematic effects are estimated by varying the magnitude of these effects in the Monte Carlo simulation and recalculating the forward-backward asymmetry.

The paper is structured as follows. A description of the detector and samples are given in Chapter 2. Event selection and candidate events are discussed in Chapter 3. The estimation and characteristics of the backgrounds are described in Chapter 4, and the acceptance and corrections for detector effects are described in Chapter 5. The systematic uncertainties are summarized in Chapter 6. The results of the forward-backward asymmetry are presented in Chapter 7.

Chapter 2

Experimental Apparatus and Data Samples

The detector used in this analysis is the Collider Detector Facility (CDF) located at the Fermi National Accelerator Laboratory (Fermilab), in Illinois (USA). CDF uses proton-antiproton collisions generated at the Tevatron Accelerator complex. A map of the lab is shown in Figure 2.1. Until the Large Hadron Collider is completed at CERN, the Tevatron is the highest energy collider in the world. In this chapter the Tevatron and CDF are described.

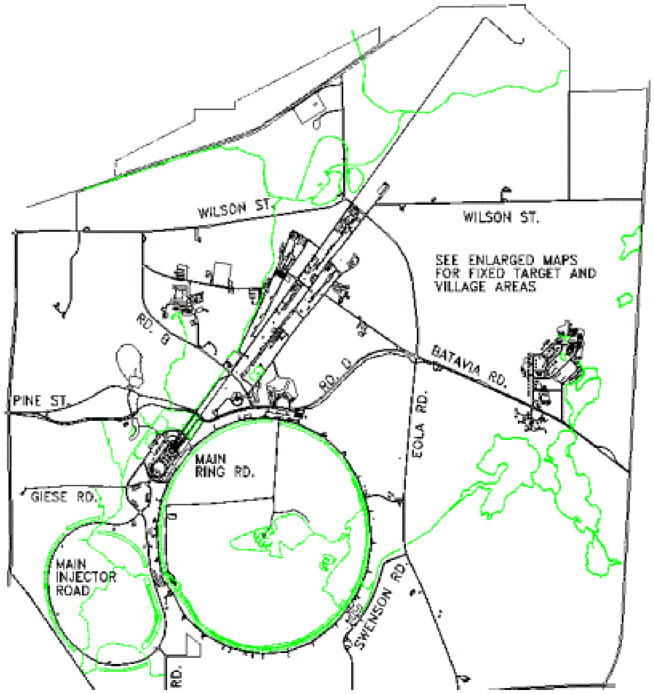

Figure 2.1: *Overview of the Tevatron accelerator chain at Fermilab.*

2.1 The Accelerator and Collider

The Tevatron is a circular accelerator of about 1 km of radius which collides bunches of protons and antiprotons accelerated in opposite directions with a total center-of-mass energy ($\sqrt{s}$) of 1.96 TeV. The acceleration happens in five stages and a schematic of the accelerator is shown in Figure 2.2. The protons used in the collisions start out as hydrogen atoms from a bottle of hydrogen gas. The hydrogen atoms are ionized (H^-) and accelerated in the Cockroft-Walton preaccelerator to 750 keV. They are then sent through a linear accelerator (LINAC) which increases their energy to 400 MeV. The electrons are stripped from the hydrogen ions by sending the ions through a carbon foil, resulting in a 400 MeV beam of protons. The beam of protons are sent to a 75 m synchrotron (Booster), which increases their energy to 8 GeV, and separates the protons into bunches. Finally they are sent through two more synchrotrons called the Main Injector and the Tevatron, where they reach energies of 150 GeV and 980 GeV respectively.

Antiprotons must be created in the lab by colliding protons with a fixed target. Protons exiting the Booster are sent toward a nickel target, and the antiprotons created in this collision are separated from other products. The antiprotons are "cooled" (reducing the phase space occupied), and accelerated so they can be sent to the Main Injector and be accelerated along with the protons.

The proton and antiproton beams are composed of 36 bunches each. The two beams are focused using quadrupole magnets at two points along the circumference of the ring, where the bunches cross about every 396 ns. These two regions are denominated D0, where the experiment of the same name is located, and B0, the center of the CDF experiment. The luminous region has a dispersion of about 30 cm in the direction of the beams ($\sigma_z \simeq 30$ cm) and the profile of the beam in the transverse plane is approximately circular and has a gaussian dispersion $\sigma_t^{beam} \simeq 30$ μm.

The Tevatron produced its first $\overline{p}p$ collisions in October of 1985, and since then has evolved, increasing the instantaneous luminosity. In 1996, after taking data on and off for about ten years (called "Run I"), the Tevatron was closed to undergo technical upgrades to improve both the center of mass energy, from 1.8 to 1.96 TeV, and the delivered luminosity for the new period of data taking called "Run II". A Comparison between some of the parameters in Run I and Run II are shown in table 2.1. At the present, the Tevatron is functioning with an instantaneous luminosity close to $4{\cdot}10^{31}$ cm^{-2}s^{-1}. The goal of Run II is to reach an instantaneous luminosity of $3{\cdot}10^{32}$ cm^{-2}s^{-1} and an integrated luminosity of 5-10 fb^{-1} by 2008.

The accumulation of total integrated luminosity over many stores is shown in Figure 2.3. After selecting data where the detector is running without major problems,

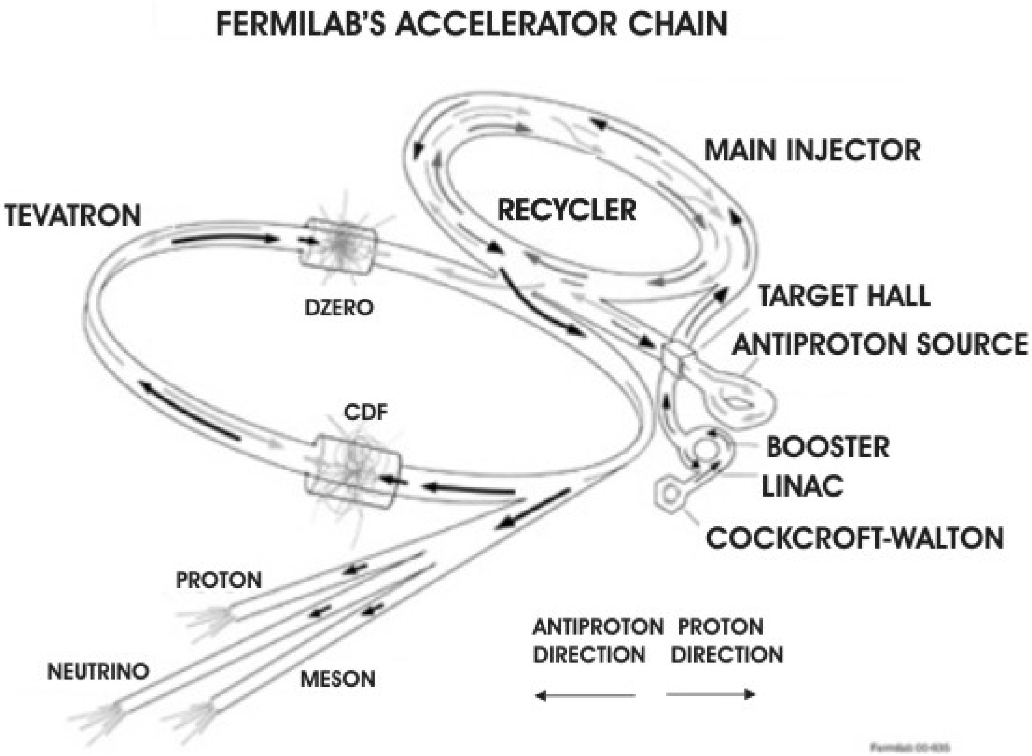

Figure 2.2: *Diagram of the several accelerators involved in the proton-antiproton collisions at the Tevatron.*

Run	**Run Ib**	**RunII**
bunches of p × bunches of $\bar{\mathrm{p}}$	6×6	36×36
p/bunch	$2.3\cdot10^{11}$	$2.1\cdot10^{11}$
$\bar{\mathrm{p}}$/bunch	$5.5\cdot10^{10}$	$2.5\cdot10^{10}$
total number of $\bar{\mathrm{p}}$	$3.3\cdot10^{11}$	$9.0\cdot10^{11}$
Energy (p+$\bar{\mathrm{p}}$) (GeV)	900+900	980+980
L ($\mathrm{cm}^{-2}\mathrm{s}^{-1}$)	$1.6\cdot10^{30}$	$4.1\cdot10^{31}$
Bunch spacing(ns)	∼3500	396
Number of interactions per collision	2.5	0.9

Table 2.1: *Parameters characteristic of different Runs at the Tevatron. The left column shows the operational performance of Run Ib, terminated in 1996; the right column shows the current parameters of Run II. (The values refer to the second best simultaneous performance.)*

there remains 72 $\text{pb}^{-1}$of data for this analysis. A list of the data accumulated by CDF in the different runs to date is shown in Table 2.2.

2.2 The CDF detector

The Collider Detector at Fermilab (CDF II) is a general purpose detector designed to study the physics of $\overline{p}p$ collisions at the Tevatron accelerator at Fermilab. Like most detectors used in high energy collision experiments it has a cylindrical geometry with axial and forward-backward symmetry. The innermost part of the detector contains an integrated tracking system with a silicon detector, and an open cell drift chamber immersed in a 1.4 T solenoidal magnetic field. The integrated tracking system is surrounded by calorimeters which cover 2π in azimuth, and from -3.6 to 3.6 in pseudorapidity, η_{det}[1].Outside of the calorimeters is a muon system with coverage from -1.5 to 1.5 in η_{det}. The CDF Run II detector is a major upgrade to the detector that took data until 1996. The entire tracking system subtending $|\eta_{det}| < 2$ and the plug calorimeter subtending $1.1 < |\eta_{det}| < 3.6$ have been replaced to handle a higher

---

[1] η is defined in two coordinate systems. The detector coordinate system (η_{det}), where θ is measured by making a vector from the center of the detector to the point at which the electron enters the calorimeter. η_{evt} is the true η of the electron measured using the angle of the electron track.

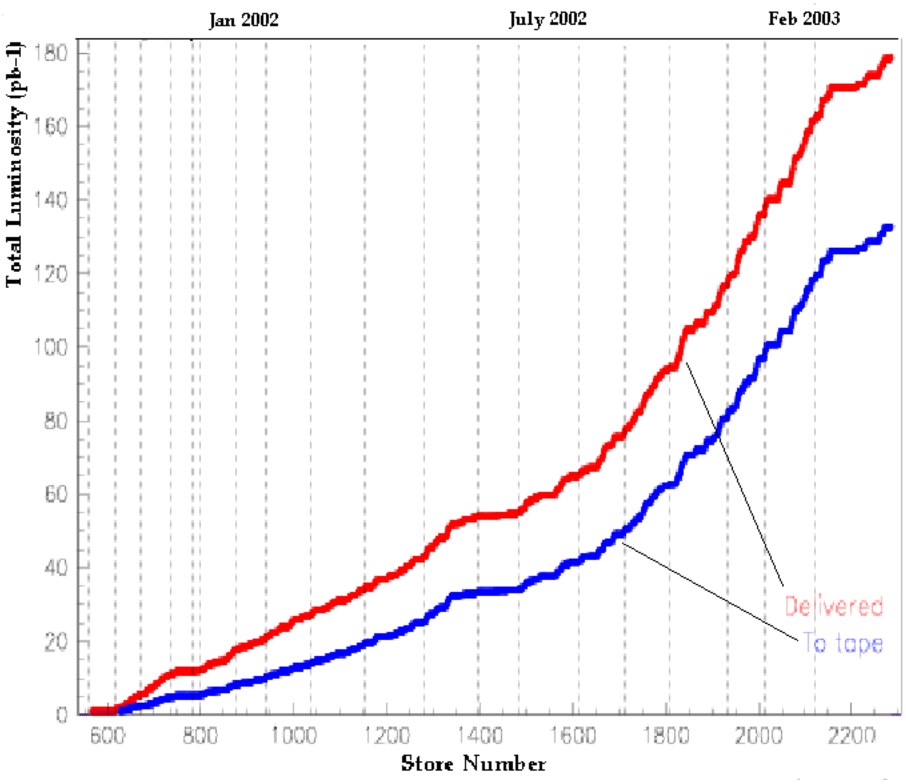

Figure 2.3: *Total integrated luminosity delivered by the accelerator and recorded by* CDF *in the period from July 2001 until January 2003, corresponding to 72.0* pb^{-1}. *The upper curve represents the luminosity delivered to the experiment, while the lower one is the luminosity effectively recorded on tape by the CDF experiment. A portion of the data taken in earlier stores was used to commission the detector and is not used for physics analyses.*

rate of collisions and to increase the capabilities for physics analyses for Run II. In this analysis the open cell drift chamber called the central outer tracker (COT) and the calorimeters are used. A more detailed detector description can be found in Refs. [27] [28], and a description of the upgraded detector can be found in Ref. [29].

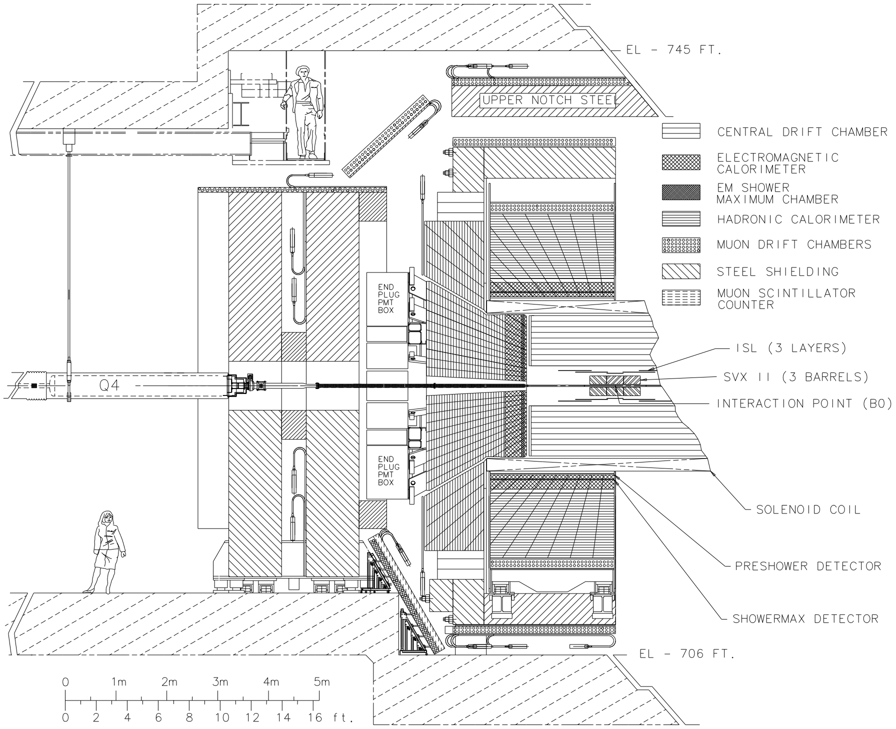

Figure 2.4: *Longitudinal view of the CDF Run II detector.*

Run	**Year**	**Integrated Luminosity ($\mathbf{pb^{-1}}$)**
	1987	0.025
Run 0	1988-89	4.5
Run Ia	1992-93	19.4
Run Ib	1994-96	90.4
Run IIa	2001-02	72.0*

Table 2.2: *Amount of data collected during the different periods of data-taking at CDF. *This is the Run IIa sample used in this analysis. Run IIa is continuing to take data.*

2.2.1 Coordinate System

CDF uses a spherical system of coordinates, with the z-axis oriented along the beam direction, where positive z is defined as the direction in which the protons are traveling. The origin is at the center of the detector. The polar angle θ is the angle measured from the positive z-axis. The angle ϕ is the angle measured from the vector lying in the plane of the accelerator pointing away from the center (shown in Figure 2.5). Since in hadron colliders the center of mass frame can be boosted along the z axis, it is useful to define quantities that are perpendicular to the z axis.

The transverse (or r–ϕ) plane is defined as the plane perpendicular to the z axis. Transverse quantities (such as E_T, p_T , etc.) are the components of those quantities in the transverse plane. The pseudorapidity η, indicated in Figure 2.6 is defined as

$$\eta = -log(tan(\frac{\theta}{2})). \tag{2.1}$$

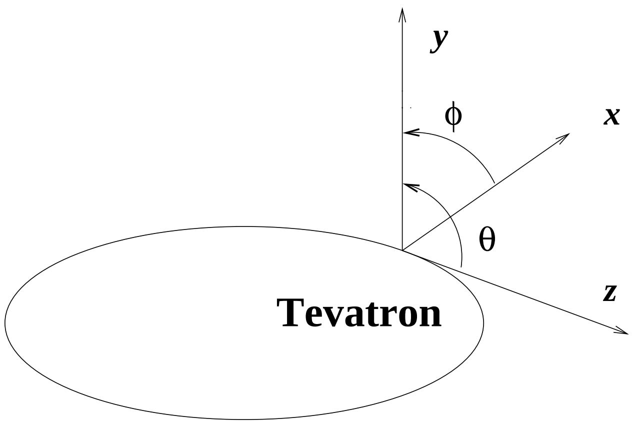

Figure 2.5: *Coordinate system used at CDF.*

2.2.2 Tracking System

The "integrated tracking system" at CDF, shown in Figure 2.6, involves a new open cell drift chamber, the Central Outer Tracker (COT), which covers the region of $|\eta| <1$ (central region), and the "silicon inner tracker" system, which provides coverage up to $|\eta| <2$. The "silicon inner tracker" consists of 3 independent structures, the L00 detector, the Silicon Vertex Detector (SVX), and the Intermediate Silicon

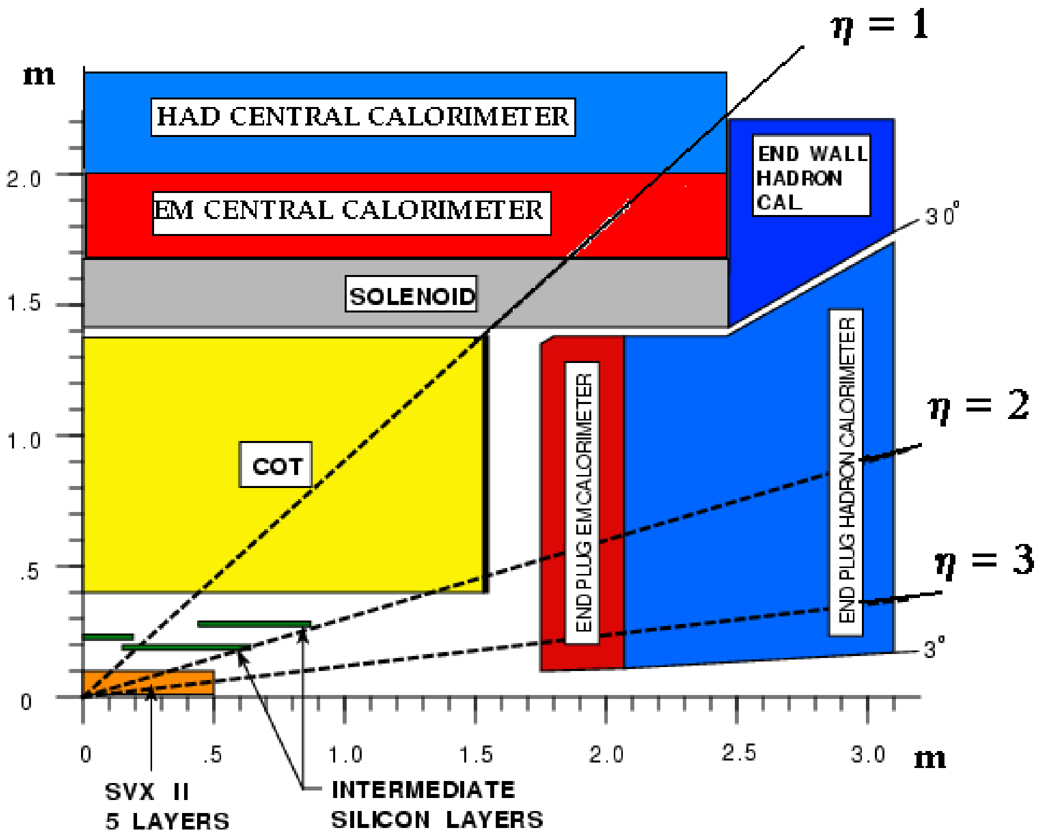

Figure 2.6: *Longitudinal view of the CDF tracking system, representing a quarter of the whole detector.*

Later (ISL). Both the SVX and ISL employ double sided silicon, where one side makes measurements in the transverse plane, and the other side is used to make measurements in the z direction.

Silicon detectors

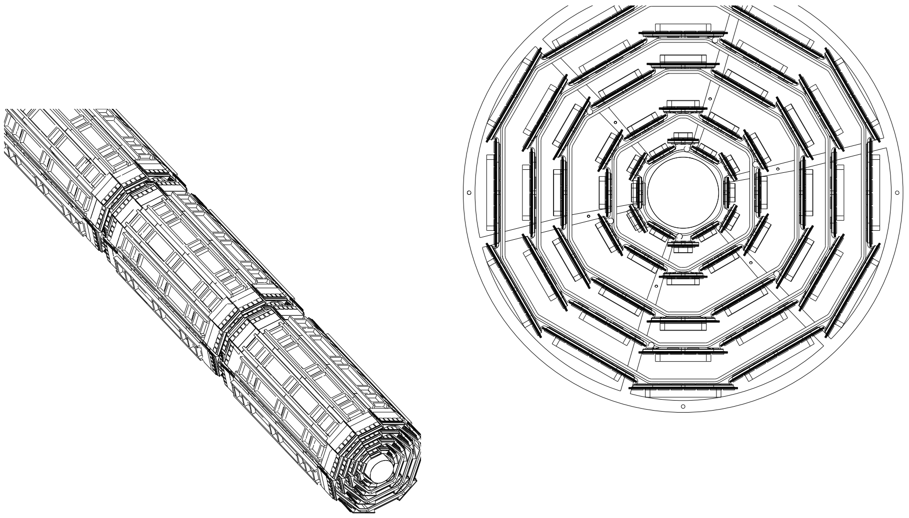

Figure 2.7: *On the left, view of the three barrels of the silicon detector. On the right, end view of one barrel showing the 12 wedges with the 5 layers.*

The silicon inner tracker consists of three concentric silicon detectors located at the very center of CDF.

The innermost one, Layer 00 (L00), is a single-sided, radiation-hard silicon layer attached to the outside of the beam pipe at a radius of 1.35 cm.

The Silicon Vertex Detector (SVX) consists of 5 layers of silicon with an inner radius of 2.4 cm and outer radius of 10.7. It is composed of three barrels, each 29 cm long, as shown in Figure 2.7; all together they extend about 45 cm in the z direction on each side of the interaction point covering 2.5σ of the luminous region. Each barrel is divided in 12 wedges in ϕ (Figure 2.7), where each wedge supports the five layers of double-sided silicon micro-strip detectors.

The Intermediate Silicon Layer (ISL) consists of three silicon layers placed at radii of 20, 22 and 28 cm respectively from the proton-antiproton beam. The layer at 22 cm covers the central region $|\eta| < 1$, while the two outer layers cover the forward region corresponding to $1 < |\eta| < 2$, where the coverage from the COT falls off. The "inner silicon tracker" when combined with the COT is designed to greatly improve the impact parameter resolution and also improve the momentum resolution.

Central Outer Tracker

Tracking in the central region is provided by the Central Outer Tracker [30], an open cell drift chamber which consists of eight superlayers (Figure 2.8) of cells placed between the radii of 40 and 132 cm from the beam pipe. Each superlayer consists of 12 layers of sense wires alternated with potential wires in a plane, as shown in Figure 2.8. Half of the superlayers are axial (for the measurements in the transverse plane), and the other half have stereo angles of $\pm 3°$. The superlayers alternate between stereo and axial, with the innermost superlayer being stereo. A summary of the COT characteristics is given in table 2.3. The design resolution[29] on the curvature is 0.68×10^{-4} cm^{-1} which corresponds to a momentum resolution of $\sigma_{p_T}/p_T^2 \simeq 3 \times 10^{-3}$ [GeV/c]$^{-1}$. The resolution on the impact parameter d_0 is about 600 μm, the resolution on $cot\theta$ is $\sim 6 \times 10^{-3}$.

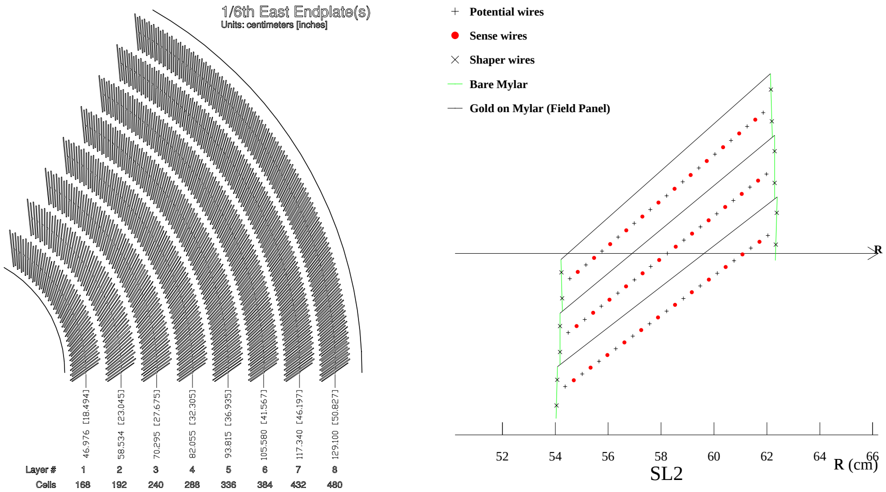

Figure 2.8: *On the left, the endplate slots are shown; in this figure the odd layers are stereo and the even layers are axial superlayers, according to the definition in the text. On the right, a single cell layout is shown.*

COT	
radial coverage	44 to 132 cm
number of superlayers	8
stereo angle	+3, 0, -3, 0, +3, 0, -3, 0^o
layers per superlayer	12
drift field	2.5 kV/cm
maximum drift distance	0.88 cm
maximum drift time	100 ns
resolution per measurement	180 μm
rapidity coverage	$\|\eta\|$ <1
number of channels	30,240
material thickness	1.6%X_0

Table 2.3: *Design parameters of the Central Outer Tracker at CDF.*

The tracking system is a crucial element in the identification of the electrons in the central region, as electron candidates are formed by energy clusters in the electromagnetic calorimeter which match a track in the COT. The electron identification algorithms use the curvature information and the direction of the track. Since the impact parameter is not used in this analysis, the silicon measurements are not used. The curvature resolution is improved by constraining the track to pass through the beam line. This improves the momentum resolution for COT tracks from 3×10^{-3}

$[\mathrm{GeV/c}]^{-1}$ to 1×10^{-3} $[\mathrm{GeV/c}]^{-1}$ which is equivalent to the improvement achieved by adding silicon hits.

2.2.3 Calorimeters

Located immediately outside the solenoid, the calorimetry system at CDF is used to measure the energy of charged and neutral particles produced in the $p\bar{p}$ collisions. The calorimeter is divided into two physical sections: the Central ($|\eta| < 1$), which is the same detector as in Run I, and the brand new Plug ($1.1 < |\eta| < 3.64$) detector. Each section is subdivided into an electromagnetic (CEM,PEM) and hadronic portion (CHA,PHA). The end-wall hadronic calorimeter(WHA) covers a gap between the central and plug hadronic sections, as shown in Figure 2.6. The properties of each calorimeter are summarized in table 2.4. The central calorimeter is divided at η=0 in two halves; each half consists of 24 wedges in ϕ, giving a total of 48 wedges. A wedge, as shown in Figure 2.9, is segmented into ten towers, subtending 0.1 in η and 15^o in ϕ. The CEM is a sampling calorimeter made of lead sheets interspersed with polystyrene scintillator. The CHA and WHA use acrylic scintillator sandwiched between sheets of iron with a similar readout scheme to that of the CEM. Where the central calorimeter is retained mostly unchanged from Run I [31], the plug detector (Figure 2.10) [32] is a major component of the Run II upgrade, and largely follows the design of the central detector. The major difference between the central and plug calorimeters is that the tower size (measured in $\Delta\phi$ and $\Delta\eta$) increases as the towers get closer to the beamline(Figure 2.10). Since the calorimeter segmentation is rather large compared to the dimensions of an electron shower, proportional chambers (CES and PES) are embedded near the shower maximum about six radiation lengths (X_0) within the EM calorimeters. The purpose of the shower maximum detector is to measure the position of the showers and to differentiate electrons from jets faking the signature of an electron using the shower shape. This information determines the location of the shower centroid within a tower and allows shower-track matching to be performed. A second set of proportional chambers is placed in between the front face of the EM calorimeters and the magnet coil. Acting as a shower presampler, this chamber can be very useful in the pion-photon separation and in the identification of the electrons. The characteristics of the CES and the CPR are summarized in table 2.5.

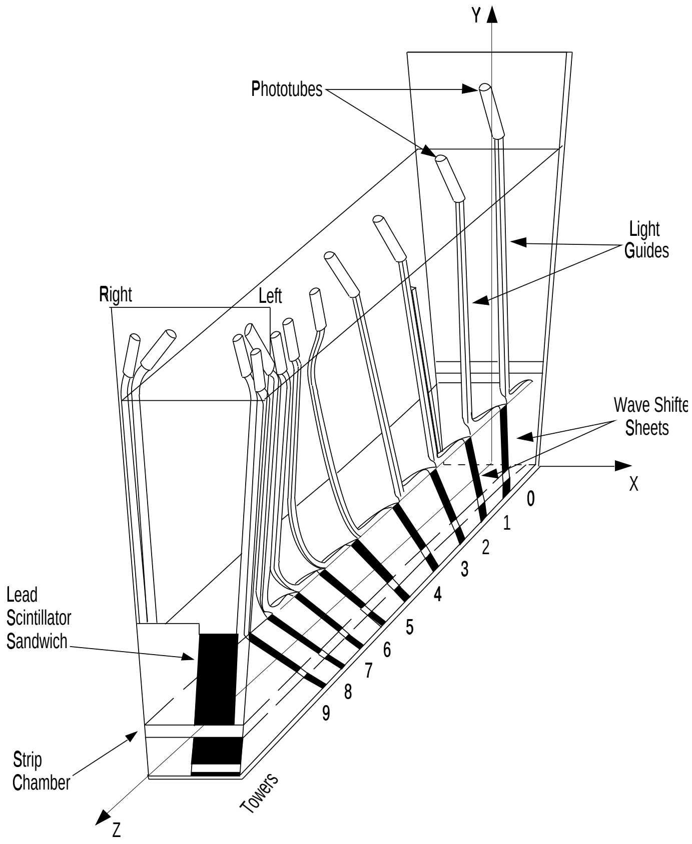

Figure 2.9: *View of one wedge of the central calorimeter. Each wedge covers 1 tower in the azimuthal direction ($\Delta\phi = 15^o$) and ten towers in the η direction (0< $|\eta|$ <1.1). The proportional chamber(CES), referred as "Strip Chamber" in the figure, can be seen embedded at shower maximum. Both edges are uninstrumented in order to leave space for light guides that connect the scintillator to the PM tubes.*

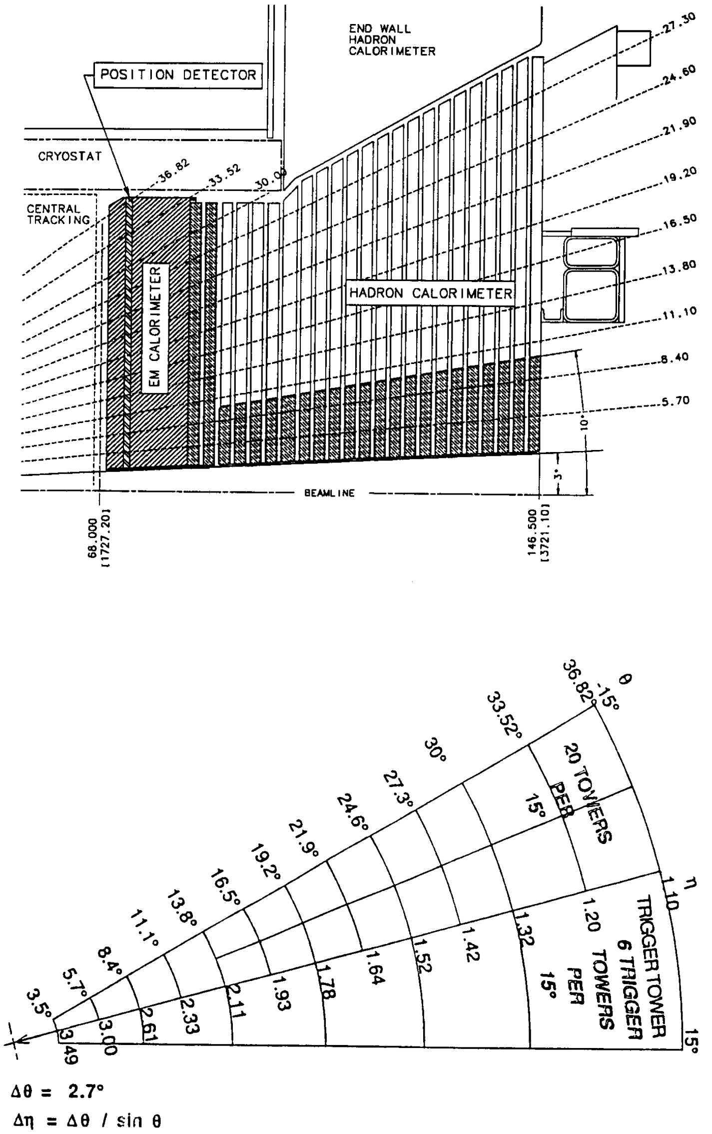

Figure 2.10: *Cross section of upper part of plug calorimeter (above), and transverse segmentation, showing physical and trigger towers in a* 30° *section (below). The logical segmentation for clustering purposes is the same except in the outer two rings* ($\theta > 30°$)*, where two neighboring (in azimuth)* 7.5° *towers are merged to match the* 15° *segmentation of the central and wall calorimeters behind them.*

2.2.4 Muon detectors

Muons are minimum ionizing, and tend to lose very little energy while traveling through the calorimeter. The characteristic signature for a muon in the CDF detector is a charged particle track, minimum ionizing energy in the calorimeters, and an additional track found in the chambers outside of the detector. For muon detection CDF uses four systems of absorbers, scintillators and proportional chambers in the detection of muons over the region $|\eta| \leq 2.0$. They are the Central Muon detector(CMU), the Central Muon Upgrade detector(CMP), the Central Muon Extension(CMX) detector and the Barrel Muon Detector(BMU). All four detectors are composed of layers of single wire drift chambers, of which alternating layers are staggered, in order to eliminate hits position ambiguities. An overview of their η and ϕ coverages at CDF is shown in Figure 2.11, and their characteristics are briefly summarized in table 2.6. None of the muon detectors are used in this analysis.

2.2.5 Trigger systems

The trigger system has also undergone a complete redesign as a result of the accelerator and detector upgrades. The CDF trigger is a three-level system that selects events out of a 1.7 MHz crossing rate and writes events to magnetic tape at a rate of 75 Hz. The first two levels [33] are composed of dedicated electronics with

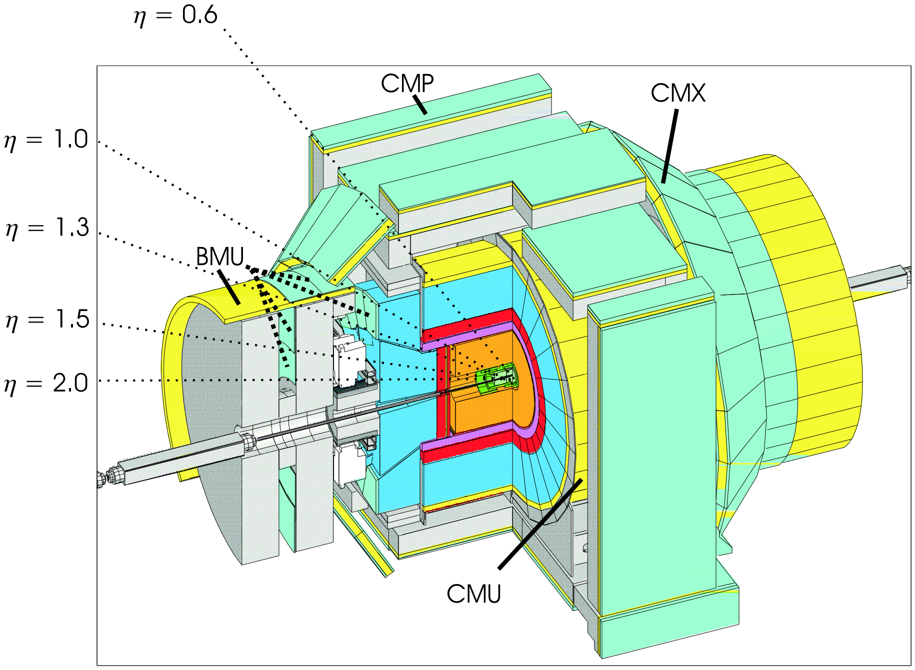

Figure 2.11: *Three dimensional view of the CDF detector, where the muon chambers are indicated with their respective coverage in pseudorapidity.*

data paths separate from the data acquisition system. The third level [34] receives the full data from the data acquisition system and runs a version of the reconstruction software that is optimized for speed on a farm of commercial computers. Figure 2.12 shows a functional block diagram of the data acquisition system, while the block diagram of the trigger system is shown in Figure 2.12.

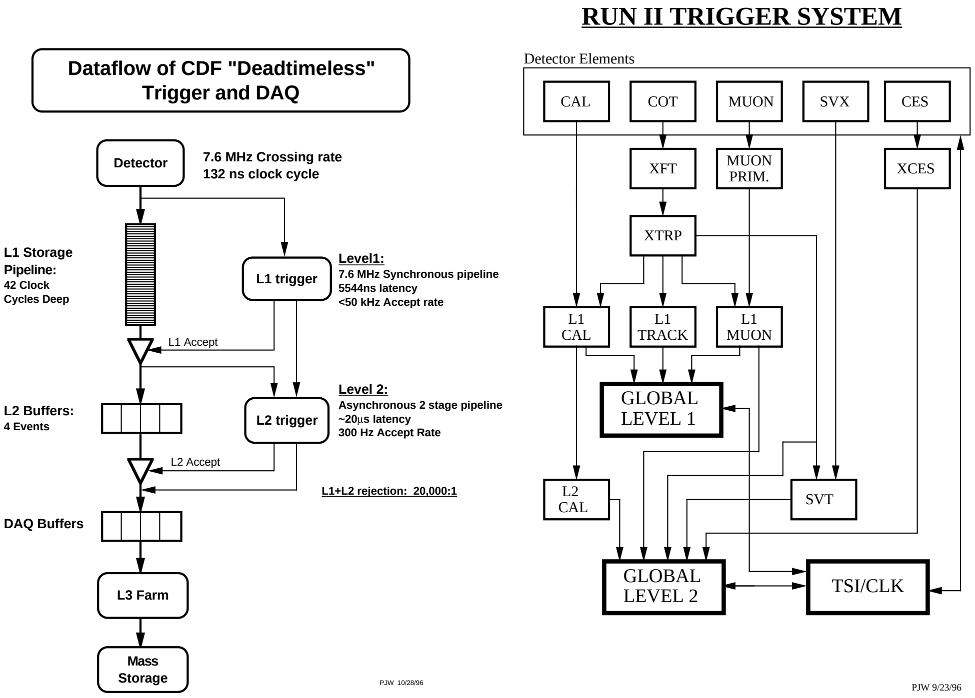

Figure 2.12: *The readout functional block diagram (left) and the trigger system block diagram (right).*

<table>
<tr><th></th><th>CEM</th><th>CHA,WHA</th><th colspan="2">PEM</th><th colspan="2">PHA</th></tr>
<tr><td>Energy Resolution</td><td>$14\%/\sqrt{E}$</td><td>$75\%/\sqrt{E}$</td><td colspan="2">$16\%/\sqrt{E} \oplus 1\%$</td><td colspan="2">$80\%/\sqrt{E} \oplus 5\%$</td></tr>
<tr><td>Angular Coverage (in $|\eta|$)</td><td><1.1</td><td><1.3</td><td colspan="2">$1.1 < |\eta| < 3.6$</td><td colspan="2">$1.2 < |\eta| < 3.6$</td></tr>
<tr><td rowspan="3">Segmentation ($|\eta|$ range, $\Delta\eta \times \Delta\phi$)</td><td></td><td></td><td colspan="2"></td><td colspan="2"></td></tr>
<tr><td colspan="2">< 1.1</td><td>1.1-1.8</td><td colspan="2">1.8-2.1</td><td>2.1-3.6</td></tr>
<tr><td colspan="2">0.1×15^o</td><td>0.1×7.5^o</td><td colspan="2">0.16×7.5^o</td><td>$0.2\text{-}0.6 \times 15^o$</td></tr>
<tr><td>Absorber, Active Medium</td><td>lead, scintillator</td><td>iron, scintillator</td><td colspan="2">lead, scintillator</td><td colspan="2">iron, scintillator</td></tr>
<tr><td>Position Resolution $(r - \phi \times z)^{(a)}$</td><td>$0.2\,\text{cm} \times 0.2\ \text{cm}^{(b)}$</td><td>$10\,\text{cm} \times 5\ \text{cm}$</td><td colspan="2"></td><td colspan="2"></td></tr>
<tr><td>Longitudinal Depth</td><td>$19\ \text{X}_0, 1\lambda$</td><td>4.5λ</td><td colspan="2">$21\ \text{X}_0, 1\lambda$</td><td colspan="2">7λ</td></tr>
</table>

$^{(a)}$ At 50 GeV incident energy $^{(b)}$ Using the CES chambers

Table 2.4: *Characteristics of the CDF RunII calorimeters.* X_0 *is the radiation length and* λ *is the hadronic interaction length.*

	CES		**CPR**
	(2 per 15^o wedge)		(2 per 15^o wedge)
	wires	strips	wires
	(r-ϕ view)	(z view)	(r-ϕ view)
number of channels	64	64	32
spacing (cm)	0.63	1.8	1.0
spatial resolution (cm)	0.2	0.2	0.5
chamber length in z(cm)	115		103
chamber width in $\phi(^o)$	12.4		10.2

Table 2.5: *Description of the Shower-Max (CES) and the Preshower (CPR) central detectors.*

	CMU	**CMP**	**CMX**	**BMU**
pseudorapidity coverage	$\vert\eta\vert < 0.6$	$\vert\eta\vert < 0.6$	$0.6 \leq \vert\eta\vert \leq 1.0$	$1.0 \leq \vert\eta\vert \leq 1.5$
drift tube length	226 cm	640 cm	180 cm	363 cm
drift tube width	6.35cm	15 cm	15 cm	8.4 cm
max drift time	800 ns	1.4μs	1.4μs	800 ns
total drift tubes	2304	1076	2208	1728
scintillation counter thickness		2.5 cm	1.5 cm	2.5 cm
scintillation counter width		30 cm	30-40 cm	17 cm
scintillation counter lengths		320 cm	180 cm	180 cm
total counters		269	324	864
pion interaction length	5.5	7.8	6.2	6.2-20
minimum detectable muon p_T	1.4 GeV/c	2.2 GeV/c	1.4 GeV/c	1.4-2.0 GeV/c
multiple scattering resolution	12 cm/p	15 cm/p	13 cm/p	13-25 cm/p

Table 2.6: *Design parameters of the CDF II Muon Detectors. Pion interaction lengths and multiple scattering are computed at a reference angle of* $\theta = 55^o$ *in CMX, and show a range of values for the BMU.*

Level-1

The goal of the Level-1 (L1) trigger is to process information on every beam crossing (1.7 MHz), and reduce the rate to less than 50 kHz. It does this by using a pipeline 42 clock cycles deep (clock cycle = 132 ns). In this time three parallel synchronous streams process a simplified subset of the data to reconstruct COT tracks, energy depositions above threshold in a calorimeter tower, and muon tracks in the muon chambers. COT tracks are matched to calorimeter towers and to muon tracks. This information is fed into a single Global Level-1 decision unit, which makes decisions based on the number of these objects that satisfy certain trigger requirements. If an event satisfies any one of a number of trigger requirements it is passed on to Level-2.

Level-2

The goal of the Level-2 (L2) trigger is to reduce the rate from L1 (<50 kHz) to 300 Hz. Events accepted by L1 are processed by the second level of trigger, which is composed by several asynchronous subsystems. L2 collects the information available at L1 and does some further reconstruction. It identifies displaced vertices seeded by the L1 tracks, collects nearby towers with energy depositions into calorimeter clusters, and measures the amount of energy deposited in the CES detector in each wedge. All of this information is sent to the programmable L2 processors in the Global Level-2 crate, which evaluate if any of the Level-2 triggers are satisfied.

Level-3

The goal of the Level-3 (L3) trigger is to assemble the event fragments from each subdetector's readout, reconstruct the objects in the event using the full data of the detector and reduce the rate from 300 Hz to 75 Hz. The L3 trigger subsystem is composed of two main components, the Event Builder (EVB) and the L3 Farm. After an event is accepted by L2, the Event Builder assembles all event fragments from the Front End crates into one data block. The L3 Farm takes the assembled event and runs an optimized analysis level reconstruction program. The L3 algorithms take advantage of the full detector information and improved resolution not available to the lower trigger levels. The events are then passed to a trigger algorithm that categorizes the event and makes the decision as to whether to be permanently stored. The selected events are passed to the Data-Logger subsystem.

2.3 Data Samples

Four data samples are employed in this analysis. These are described briefly below and in more detail in subsequent sections.

- *The $Z/\gamma^* \rightarrow e^+e^-$ sample:* A sample of 5.2 k dielectron candidates is used to measure A_{FB}, to calibrate the energy scale and resolution of the EM calorimeter, and to study the material in the tracking volume.

- *The $W \to e\nu$ sample:* A sample of 38 k $W \to e\nu$ candidates, where electrons are in the central region, is used to study the material in the tracking volume, to calibrate the relative calorimeter response within a central tower, and to check charge biases in measuring electrons.

- *The inclusive electron sample.* A sample of 3 million central electron candidates with $E_T > 8$ GeV is used to calibrate the relative response of the central EM calorimeter towers.

- *The dijet samples.* A sample of 1 million dijet events (events with at least two jets with $E_T > 15$ GeV) is used to measure the rate at which a jet fakes an electron signature and to estimate the dijet background. Triggers for the sample require a calorimeter tower with $E_T > 5$ GeV at Level 1, a calorimeter cluster with $E_T > 15$ GeV at Level 2, and a reconstructed jet with $E_T > 20$ GeV at Level 3. Due to the high cross section, only 1 in 384 events were randomly selected to be recorded for this trigger (average prescale). Jet samples with higher trigger thresholds (50 GeV, 70 GeV, and 100 GeV at Level 3) are also used to cross-check the fake rate, and to understand the jet trigger bias in the fake rate.

2.4 Monte Carlo Generation and Simulation

The Monte Carlo generation and simulation are used to estimate the acceptance for the Drell-Yan process and the effect of QED final state radiations and detector resolutions, to determine the characteristics and amount of background in the data sample, and to understand the systematic uncertainties on the A_{FB} measurement. PYTHIA [35] and HERWIG [36] generators with the CTEQ5L [37] PDFs (see Section 1.1) are used for most of the samples. These generate processes at the leading order and incorporate initial and final state QCD and QED [2] radiation via their parton shower algorithms. PYTHIA is tuned so that the underlying event and p_T spectrum of Z bosons agree with the CDF data [38]. The detector simulation models the decay of generated particles and their interactions with the various elements of the CDF detector. The amount of material between the collision point and the outer cylinder of the COT is tuned so that the electron variables which are sensitive to external bremsstrahlung match between the data and the simulation (see Section 3.7). The calorimeter energy scale and resolution in the simulation are tuned so that the mean and width of the $Z \to e^+e^-$ peak in the simulation match with those from the data (see Section 3.6). Two matrix element generators, WGAMMA [39] and ALPGEN [40], are used to check the $W + X \to e\nu + X$ background where X is a photon

---

[2] Initial and final state QED radiations are not incorporated in HERWIG.

or a parton. The generator WGAMMA calculates the cross section of $\overline{p}p \rightarrow W\gamma$ processes. It uses electroweak helicity amplitudes for $W\gamma$ production and radiative W boson decays, including all interference terms. ALPGEN performs the calculation of the matrix elements for W + partons. In this analysis ALPGEN is used to generate W + one-parton processes. There are nine Monte Carlo samples used in this analysis, which are briefly described below.

- *The $Z/\gamma^* \rightarrow e^+e^-$ sample:* A sample of 1.7 M events generated with PYTHIA is used to calculate the corrections due to acceptance, QED radiation, and energy resolution and to estimate the systematic uncertainties due to the energy scale and resolution. A quarter of these events were generated with $M_{Z/\gamma*} >$ 105 GeV to reduce the statistical uncertainties of the Monte Carlo sample in the high mass region.

- *The $Z/\gamma^* \rightarrow e^+e^-$ sample for material systematics:* Three PYTHIA samples of 700 k events are used to estimate the change in A_{FB} between the default simulation and adding or subtracting 1.5% radiation length (X_0) of copper in a cylinder in the central region and $\frac{1}{6}X_0$ of iron on the face of the plug calorimeter. Fragmentation is turned off for these samples in order to save CPU time.

- *The $Z/\gamma^* \rightarrow \tau^+\tau^-$ sample:* A PYTHIA sample of 500 k events is used to estimate the background due to $Z/\gamma^* \rightarrow \tau^+\tau^-$.

- *The dijet sample:* A PYTHIA sample of 750 k events with all $2 \rightarrow 2$ processes is used to understand the characteristics of the dijet background. A lower limit of $p_T > 18$ GeV on the transverse momentum in the rest frame of the hard interaction is applied.

- *The $t\bar{t}$ sample:* A HERWIG sample of 400 k events is used to estimate the background due to $t\bar{t}$ production.

- *The diboson samples:* A sample of 800 k events with WW production and a sample of 50 k events with WZ production are generated using PYTHIA and used to estimate the diboson backgrounds.

- *The $W \rightarrow e\nu$ sample:* A PYTHIA sample of 1.5 M events is used to estimate the background due to the inclusive W production.

- *The $W\gamma \rightarrow e\nu\gamma$ sample:* A WGAMMA sample of 210 k events is used to cross-check the background due to $W + \gamma$ production.

- *The $Wp \rightarrow e\nu p$ sample:* A ALPGEN sample of 275 k events is used to estimate the background due to W + one-parton production.

Chapter 3

Electron Identification and Event Selection

This analysis requires two electrons in the event, one in the central region, and the other in the central or plug region. This chapter describes the identification of central and plug electrons, the event selection criteria, the energy scale and resolution, and the charge identification of electrons.

3.1 Electron Candidates

The electron identification in the central region is almost identical to the algorithm used in Run I, since the calorimeter is unchanged and the new drift chamber has a very similar geometry to the previous one. For a more detailed description of the central electron reconstructed variables see Ref. [28]. An electron candidate is reconstructed if there is a central tower with $E_T > 2$ GeV and a track that extrapolates to the tower. The adjacent towers on either side in η_{det} are added to the cluster, and the cluster is not accepted if the energy in the hadronic part is more than 12.5% of the energy in the EM part. An electron is considered within the fiducial region of the detector when its track begins within 60 cm in z of the center of the detector and extrapolates to the calorimeter away from any tower boundaries. The η_{det} range of electrons in the central region is $|\eta_{det}| < 1.0$. The energy of the electron is determined by the total energy it deposits in the EM calorimeter. The electron direction, used to calculate the transverse component of energy (E_T) and the invariant mass of two electrons, is determined by the direction of the highest p_T track associated with the EM cluster. The charge of the electron (Q) is determined from the curvature of the track.

The electron clusters in the plug region, subtending $1.2 < |\eta_{det}| < 3.0$, are limited to 2×2 towers (two towers in pseudorapidity by two towers in azimuth). Since the Moliere radius of a typical electron shower is significantly smaller than the size of the plug EM towers, the clusters fully contain electron energies. As with the central clusters, plug electron clusters are accepted if $E_{had}/E_{em} < 12.5\%$. The major difference between central and plug electrons is the tracking. In the central region, the COT tracking is very efficient[1] (99.6%), whereas in the plug region the efficiency rapidly falls off as $|\eta_{det}|$ increases due to the acceptance of the COT. In this analysis no tracking is used for plug electrons. The z position of the collision for the event (z_{vertex}) is provided by the z position of the central electron's track. The electron's shower centroid is determined from a fit of the energy distribution among the calorimeter towers. The direction of the plug electron is determined by z_{vertex} and the shower centroid. The unmeasured charge of the plug electron is assumed to be the opposite

---

[1] This is measured in the $W \rightarrow e\nu$ sample where the electrons are triggered and selected without any tracking requirements.

of the central electron.

3.2 Central Electron Identification

The "tight" and "loose" selection criteria of electrons are listed in Table 3.1. The variables that are used to discriminate electrons from hadrons, some of which are shown in Figure 3.1, are:

- *Electromagnetic(EM) cluster and* E_T

  This is defined by two towers in pseudo-rapidity ($\Delta\eta \simeq 0.2$) and one tower in azimuth ($\Delta\phi \simeq 15°$). The transverse electromagnetic energy E_T is calculated as the EM cluster energy times $sin\theta$, where θ is measured by using the COT track associated with the electron.

- E_{had}/E_{em}

  This variable is the ratio of the total energy in the hadron calorimeter to the total energy in the EM calorimeter for the towers included in the electron cluster. Electron showers of very high energies are less likely to be completely contained in the EM portion of the calorimeter. In order to maintain high efficiency for all electrons, the E_{had}/E_{em} cut is scaled with energy by adding an energy dependent term to the cut value.

- *Isolation*

  This variable is defined as

  $$E_T^{iso} = E_T^{0.4} - E_T^{cluster} - E_T^{expected},$$

  where $E_T^{0.4}$ is the energy in a cone of radius $\Delta R = \sqrt{\Delta\eta^2 + \Delta\phi^2} \leqslant 0.4$ around the electron cluster, $E_T^{cluster}$ is the energy of the electron cluster, and $E_T^{expected}$ is the amount of electron energy that is expected outside of the electron cluster.

- χ^2_{strip}

  This variable compares the shower profile measured with the Central Electromagnetic Shower-Max (CES) detector to the shape measured with test beam data. A χ^2 test comparison is made on the energy of each of the 11 strips in z of the CES detector.

- L_{shr}

  This variable is a comparison of the lateral sharing of energy among the calorimeter towers with that of test beam electrons. This is done by comparing the observed sharing of energy deposition between towers in the CEM to that expected for a "true" electromagnetic shower, taken with test-beam data. L_{shr} is defined as

  $$L_{shr} = 0.14\Sigma_i \frac{E_i^{adj} - E_i^{expected}}{\sqrt{(0.14\sqrt{E})^2 + (\Delta E_i^{expected})^2}},$$

where the sum is only over towers in the electron cluster, and

  - E_i^{adj} is the measured energy (in GeV) in a tower adjacent to the seed tower,
  - $E_i^{expected}$ is the expected energy (in GeV) in the adjacent tower, calculated using a parametrization from test beam data,
  - $0.14\sqrt{E}$ (E in GeV) is the error on the energy measurement, and
  - $\Delta E_i^{expected}$ is the error on the energy estimate.

- *E/p and p_T*

  These quantities use the momentum of the track associated with the electron. E/p is the ratio of the transverse electromagnetic energy of the electron cluster measured in the CEM to the transverse momentum of the track measured in the COT. While in an environment with no material E/p would peak at one, electrons lose energy through external bremsstrahlung while passing through material. Most of the photons are emitted colinearly and fall into the same tower as the electron, but the electron itself loses energy, leaving a track with lower p_T . The E/p distribution has a long tail for $E/p > 1$, which is sensitive to the amount of material the electron traversed.

- $Q * \Delta X$ and ΔZ

  The track associated with the electron is extrapolated to the CES plane, and the extrapolated position is compared to the shower centroid position as measured in the CES. The variable ΔZ is the separation in the z direction between the extrapolated track position and the CES cluster centroid. The variable ΔX is the corresponding separation in the r-ϕ direction. An asymmetric cut is made on $Q * \Delta x$ because photonic radiation can distort the shower shape in the $r - \phi$ direction. Since the magnetic field bends an electron's trajectory but not a photon's, the bremsstrahlung photons tend to enter the calorimeter to the side of the primary electron opposite the bending, which is determined by the electron's charge. By multiplying the charge by Δx, most of the distortion from bremsstrahlung photons is isolated to negative $Q * \Delta x$ as seen in Figure 3.1.

3.3 Plug electron identification

The selection criteria of plug electrons are listed in Table 3.1. The following variables are used to discriminate electrons from hadrons in the plug region (see Figure 3.1):

- *EM cluster and* E_T

  The transverse electromagnetic energy E_T is calculated using the z_0 of the COT track associated with the highest-E_T central electron in the same event.

- E_{had}/E_{em}

  This variable is the ratio of the total energy in the hadron calorimeter to the total energy in the EM calorimeter for the towers included in the electron cluster. The new plug EM calorimeter is deeper (in radiation lengths) than the central EM calorimeter 2.4, and penetration of electron showers into the hadron portion can be ignored for our cut. and

- *Isolation*

  This variable is defined as

  $$E_T^{iso} = E_T^{0.4} - E_T^{cluster} - E_T^{expected},$$

  where $E_T^{0.4}$ is the energy in a cone of radius $\Delta R = \sqrt{\Delta\eta^2 + \Delta\phi^2} \leqslant 0.4$ around the electron cluster, $E_T^{cluster}$ is the energy of the electron cluster, and $E_T^{expected}$ is the amount of electron energy that is expected outside of the electron cluster.

- *PEM* $\chi^2_{3\times3}$

  This variable is a χ^2 comparison of the energy distribution in 3×3 towers around the seed tower to the energy distributions from test beam electrons The χ^2 is thus a measure of how electron-like the shower is, using only PEM information.

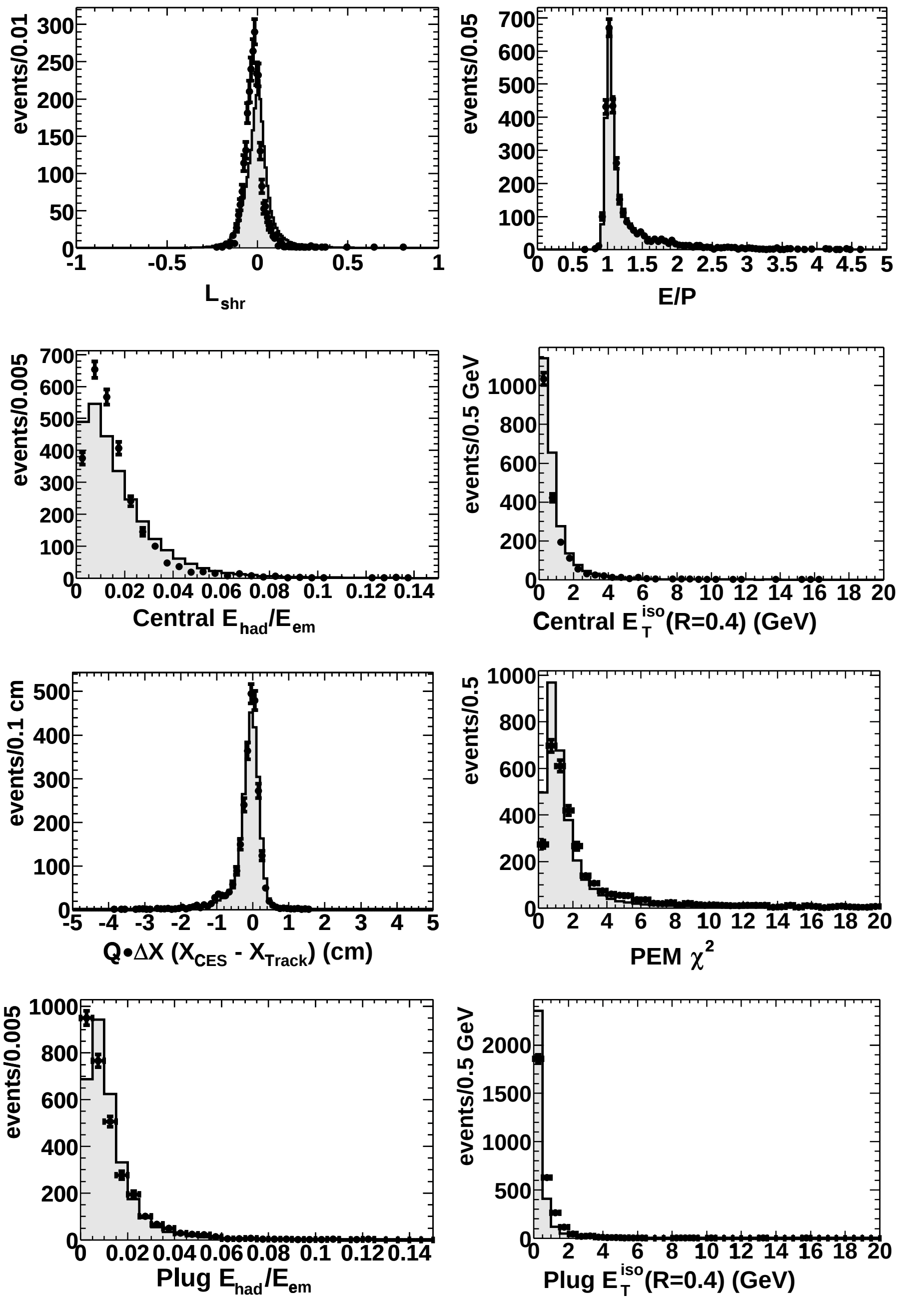

Figure 3.1: *Electron identification variables from* $Z/\gamma^* \to \ e^+e^-$*with* $75 < M_{ee} < 105$. *Points and histograms are Run II data and Monte Carlo simulation, respectively.*

Table 3.1: *Criteria for electron candidates.* $Z/\gamma^* \rightarrow\ e^+e^-$ *candidates require at least one "tight" central electron and at least one "loose" central electron or one "loose" plug electron in the event.*

Variable	"Tight" Central	"Loose" Central	"Loose" Plug
E_T	> 20 GeV	> 20 GeV	> 20 GeV
E_{had}/E_{em}	$< 0.055 + 0.00045 * E$	$< 0.05 + 0.00045 * E$	< 0.05
E_T^{iso}	< 4 GeV	< 4 GeV	< 4 GeV
p_T	> 10 GeV	> 10 GeV	
E/p	< 2 for $E_T < 50$ GeV		
L_{shr}	< 0.2		
χ^2_{strip}	< 10		
$Q * \Delta x$	> -3 cm, < 1.5 cm		
$\|\Delta z\|$	< 3 cm		
$PEM\chi^2_{3x3}$			< 10

3.4 Central Electron trigger

At Level 1, electrons are selected by the presence of an EM calorimeter tower with $E_T > 8$ GeV and a matching two-dimensional ($r-\phi$ plane) COT track reconstructed by the eXtremely Fast Tracker (XFT) [41] with $p_T > 8$ GeV/c. At Level 2, an EM cluster of towers is reconstructed and required to have $E_T > 16$ GeV. At Level 3, a reconstructed EM cluster with $E_T > 18$ GeV and a matching track with $p_T > 9$ GeV/c are required. At each level, the transverse energy in the hadronic towers just behind the EM tower or cluster is required to be less than 12.5% of EM E_T. Another trigger path that does not require a hadronic energy fraction is added to this measurement in order to improve the trigger efficiency of very high E_T central electrons. It requires a calorimeter tower (hadronic and EM combined) with $E_T > 10$ GeV at Level 1, a calorimeter cluster of towers with $E_T > 100$ GeV at Level 2, and a reconstructed electron with $E_T > 70$ GeV and $p_T > 15$ GeV at Level 3.

3.5 Event selection

$Z/\gamma^* \rightarrow e^+e^-$ candidate events are required to have two electrons with $E_T > 20$ GeV. One of the electrons is required to be in the central region passing the full set of identification cuts (see Table 3.1). This electron is called the "tight" central electron. The second “loose” electron is allowed to be in either the central or plug regions and has relaxed identification cuts for higher efficiency (see Table 3.1). Based on these selection criteria two topologies are defined for dielectron events: central-central topology, where one “tight” and one “loose” central electron are required, and central-plug topology, where one “tight” central electron and one “loose” plug electron are required. In the central-central topology, the two electrons are required to have opposite charge. In the central-plug topology, no charge requirement is made since the plug electron’s charge is not measured.

The absolute identification efficiencies are measured in the $Z/\gamma^* \rightarrow\ e^+e^-$ data[2] and are found to be $(83.4 \pm 0.8)\%$ for “tight” central electrons, $(94.3 \pm 0.5)\%$ for “loose” central electrons, and $(87 \pm 2)\%$ for “loose” plug electrons. The relative efficiency for forward and backward events and the dependence on M_{ee} are estimated from the Monte Carlo simulation. Ultimately, the absolute efficiency gets canceled in the ratio, and only the relative difference in efficiency between forward and backward events matters. The difference is largest below the Z pole, where radiative effects have a large impact. Electrons in events from the Z pole radiate photons, leading

---

[2] This is measured in the $Z/\gamma^* \rightarrow\ e^+e^-$ sample, where one tight central electron is selected, and the other electron has only kinematic requirements. The other electron whether in the central or the plug is then tested to find the efficiency of each cut or set of cuts.

to mismeasurements of the invariant mass. Since the A_{FB} is larger at the Z pole than below it, many of the forward events found below the Z pole tend to be mismeasured events. These events have a lower electron identification efficiency because of the radiation. Figure 3.2 shows the relative identification efficiency per event. The radiation due to bremsstrahlung is tuned so that the Monte Carlo simulation matches the data (see Section 3.7).

The number of events in the data passing these requirements with the dielectron invariant mass greater than 40 GeV is 1,892 for central-central $Z/\gamma^* \rightarrow e^+e^-$ candidates and 3,319 for central-plug $Z/\gamma^* \rightarrow e^+e^-$ candidates. The invariant mass distribution is shown in Figure 3.3 and the number of events is summarized in Table 3.2. Figure 3.4 shows the distribution of η_{det} for electrons in the $Z \rightarrow e^+e^-$ candidate data sample compared with the Monte Carlo simulation prediction. The discrepancies seen in Figure 3.4 are studied as a systematic on the fiducial acceptance (see Section 6).

3.6 Electron energy scale and resolution

Both local and global energy scale corrections are applied to the electron energy. Local corrections are applied to improve resolution by correcting for variations in the

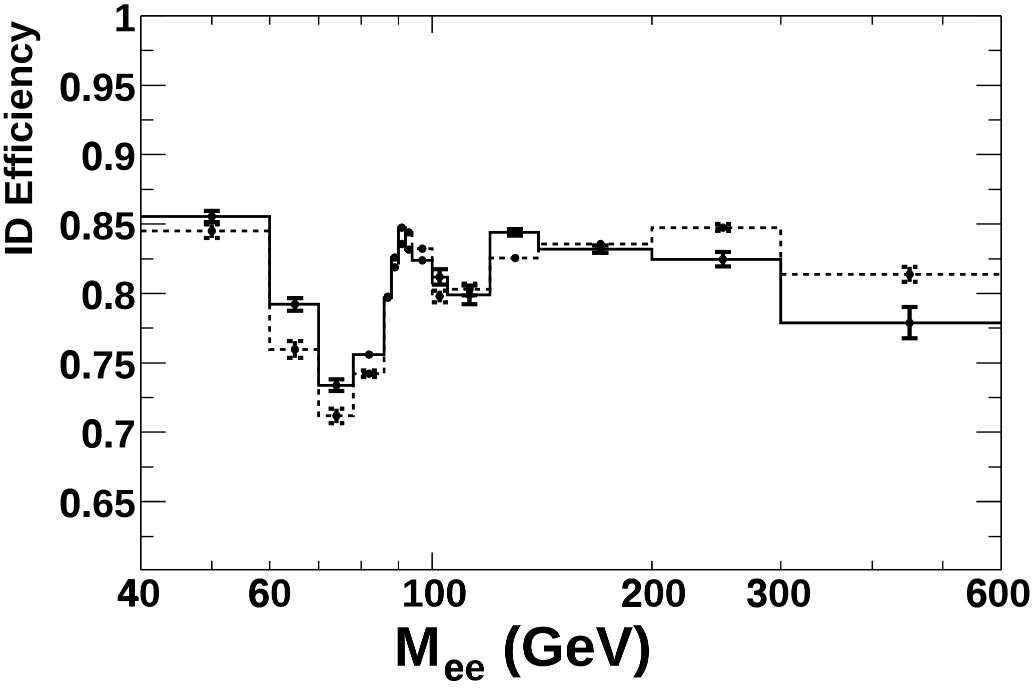

Figure 3.2: *Event electron identification efficiency ($(\epsilon_i^{\pm})_{ID}$) dependence with M_{ee} for $Z/\gamma^* \rightarrow e^+e^-$ events measured in the simulation. The dashed line is for forward events and the solid line is for backward events. The dip in efficiency below 90 GeV/c^2 is due to radiation effects (see Section 3.5). Forward and backward events are defined in Section 1.1.*

Table 3.2: *The number of central-central (C-C) and central-plug (C-P)* $Z/\gamma^* \rightarrow e^+e^-$ *candidates for each mass region.*

Mass Region	Data C-C	Data C-P
$40 < M_{ee} < 60$ GeV	69	85
$60 < M_{ee} < 70$ GeV	42	72
$70 < M_{ee} < 78$ GeV	48	119
$78 < M_{ee} < 86$ GeV	204	329
$86 < M_{ee} < 88$ GeV	151	299
$88 < M_{ee} < 90$ GeV	301	512
$90 < M_{ee} < 92$ GeV	416	610
$92 < M_{ee} < 94$ GeV	330	543
$94 < M_{ee} < 100$ GeV	243	545
$100 < M_{ee} < 105$ GeV	30	68
$105 < M_{ee} < 120$ GeV	29	61
$120 < M_{ee} < 140$ GeV	13	31
$140 < M_{ee} < 200$ GeV	9	36
$200 < M_{ee} < 300$ GeV	6	8
$300 < M_{ee} < 600$ GeV	1	1

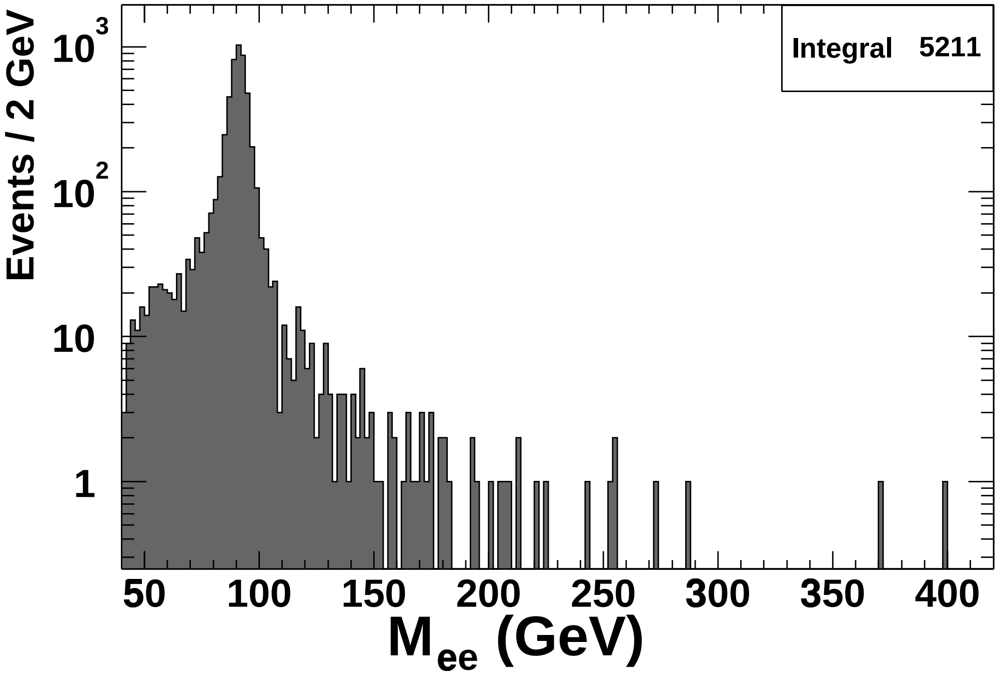

Figure 3.3: *Invariant mass distribution of* $Z/\gamma^* \rightarrow\ e^+e^-$ *candidates in 72* pb^{-1} *of Run II data.*

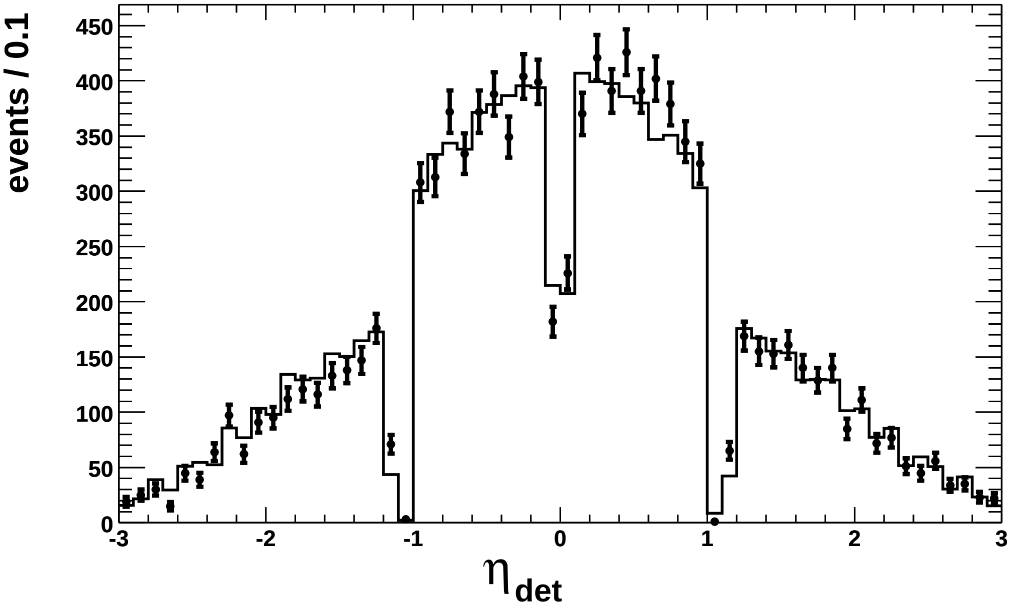

Figure 3.4: *The distribution of* η_{det} *for electrons in the* $Z \rightarrow\ e^+e^-$ *candidate sample. Points and histograms are data and Monte Carlo simulation, respectively. Monte Carlo simulation is normalized to the number of entries in the data.*

energy response of the calorimeter. They include corrections for time dependence, variations in the response at different points within a calorimeter tower[42], and variations in the gains of the different calorimeter tower channels. Electrons from the W sample and the inclusive electron sample are used to calibrate these variations. The reference for correcting the electron energy is the track momentum as measured by the COT. Uniformity is achieved by adjusting the tower energy response (gain) until the mean E/p is flat as a function of time and ϕ, and agrees with the Monte Carlo simulation as a function of η. The global energy scale is set by requiring that the mean of a gaussian fit to the Z peak region (the invariant mass region between 86 GeV/c^2 and 98 GeV/c^2) is 91.1 GeV/c^2. The central value of 91.1 GeV/c^2, instead of 91.187 GeV/c^2, is chosen because the Z peak is slightly distorted toward the lower mass due to the Q^2 dependence of the parton density and QED radiation. This prescription defines the energy scale well within the energy scale systematic uncertainty of 0.5% (0.46 GeV/c^2 at the Z peak) used in this analysis. Figure 3.5 shows the invariant mass distributions near the Z peak for central-central and central-plug events for data and Monte Carlo simulation, and Table 3.3 shows the results of gaussian fits.

Table 3.3: *The mean and σ values of gaussian fits in the invariant mass range between 86 GeV/c^2 and 98 GeV/c2 for the data and the simulation. Local and global energy scale corrections are made before the fits. The mean of the data is set to 91.1 GeV/c^2, and the mean and width of the Monte Carlo simulation are tuned to match the data.*

Type	Mass Mean (GeV)	Mass σ (GeV)
C-C Data	91.11 ± 0.09	2.89 ± 0.09
C-C MC	91.09 ± 0.01	2.98 ± 0.01
C-P Data	91.12 ± 0.09	3.41 ± 0.10
C-P MC	91.09 ± 0.01	3.34 ± 0.01

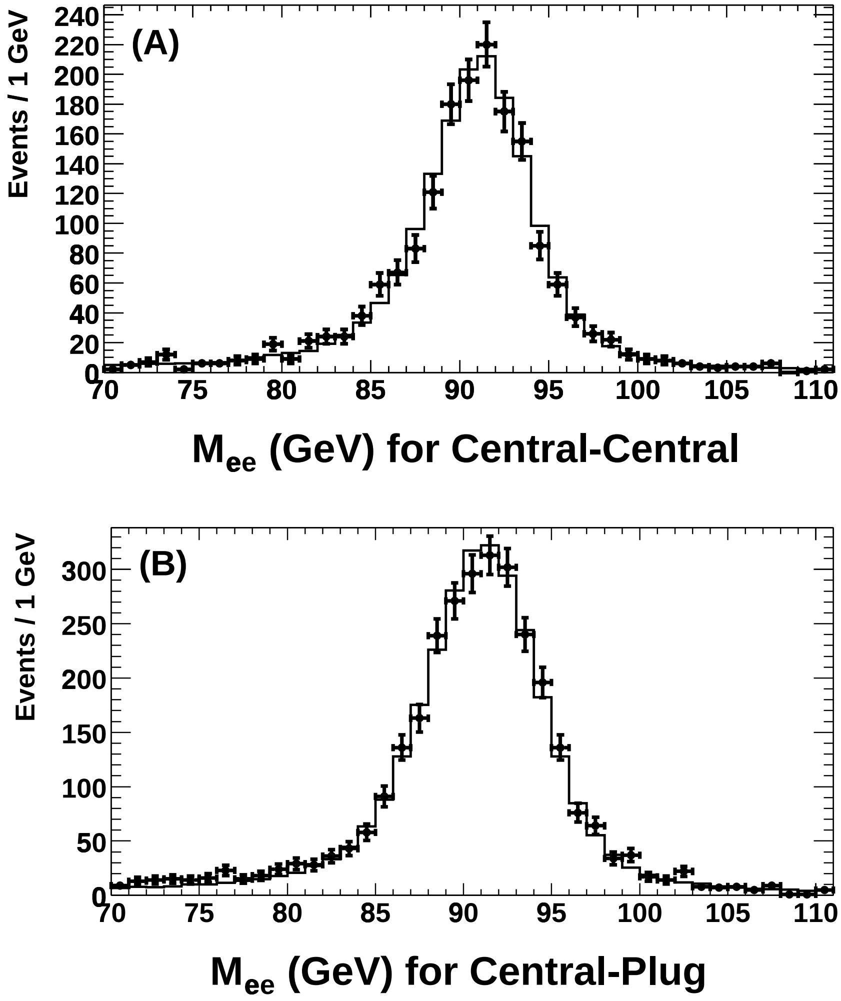

Figure 3.5: *Invariant mass distributions of* $Z/\gamma^* \to e^+e^-$ *candidates: two electrons in the central region (top), one electron in the central region and the other in the plug region (bottom). Points and histograms are data and Monte Carlo simulation, respectively. Energy scale corrections and extra smearing are applied so that the gaussian widths and peaks match as listed in Table 3.3.*

3.7 Electron Charge Identification

The charge measurement of electrons is essential for this analysis, since the events are determined as forward or backward depending on the charge of the electron. In the central-central topology, we measure the charge of both electrons and the opposite-sign requirement of the two removes major issues on the forward-backward measurement due to the charge misidentification. For events with a central-plug topology, however, the charge of two electrons is determined by one measurement from the central electron and the charge misidentification needs to be properly understood.

We use the $Z/\gamma^* \rightarrow e^+e^-$ Monte Carlo sample[3] with the central-central topology to study the sources of the charge misidentification and to measure the misidentification rate. The misidentification rate is determined by counting the number of events where both electrons have the same charge. If the rate is small, the probability of having same-sign events is approximately twice that of misidentifying the charge of a single electron. Figure 3.8 shows that above the Z pole ($M_{ee} > 100$ GeV/c^2), the rate of events with the same sign is approximately flat up to $M_{ee} \simeq 300$ GeV/c^2. It drops at the Z pole and almost doubles in the bin below it, which is caused by

---

[3] The Monte Carlo simulation is tuned using the tail of the E/p shown in Figure 3.6. The ratio between events in the tail and the peak is used to calibrate the material in the simulation and determine an uncertainty for the material in the detector.

QED radiation and e^+e^- pair production in the material. We refer this to as the charge misidentification due to "trident" electrons. Figure 3.7 demonstrates an example of "trident" electrons where a positron radiates a hard bremsstrahlung photon in the material, which converts into an electron-positron pair in the material. The electron from the photon conversion carries the highest momentum, and the charge of the primary electron (e^+) is assigned to be negative (e^-). The Monte Carlo sample shows that the charge misidentification rate coming from "trident" electrons is $(0.7 \pm 0.3)\%$. The other source of the charge misidentification is the tracking resolution ($\delta(\frac{1}{p_T}) \simeq 0.001$). At higher energies, the tracks become almost straight ($\frac{1}{p_T} \sim 0$) and the charge determination has a higher probability of being wrong. The last bin, which includes all events with $M_{ee} > 300$ GeV/c^2, has a misidentification rate of $(1.1 \pm 0.2)\%$. Corrections for the charge misidentification are included as part of the acceptance calculation via simulation. The dominant systematic uncertainty comes from the uncertainty in the amount of material between the interaction point and the tracking volume. A comparison of the same-sign events between data and Monte Carlo simulation is used to get an estimate on the background, but also shows agreement at the Z pole where there is little background (see Figure 4.5).

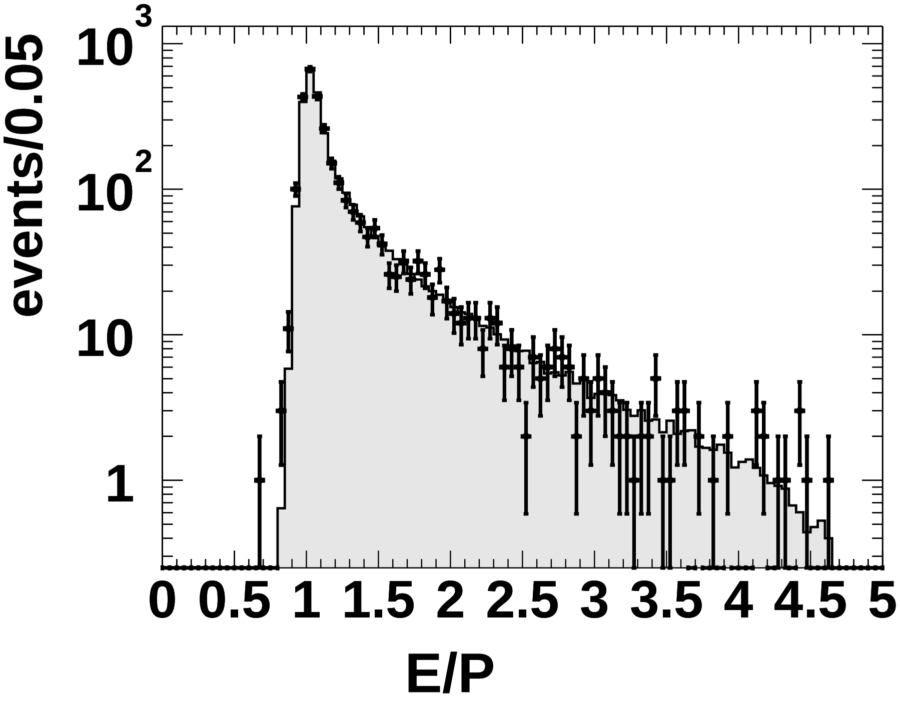

Figure 3.6: *E/p for central electrons in the $Z/\gamma^* \rightarrow e^+e^-$ candidate sample. This distribution is used to calibrate the amount of material in the Monte Carlo simulation.*

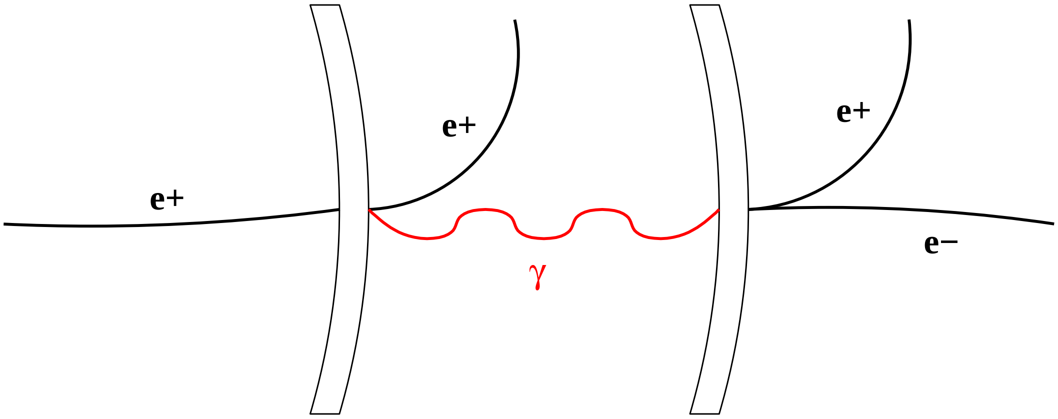

Figure 3.7: *A schematic diagram of a "trident" electron where a positron radiates a hard bremsstrahlung photon in the material and the photon converts into an electron-positron pair in the material. The electron from the photon conversion carries the highest momentum, thus the charge of the primary electron* (e^+) *is assigned to be negative* (e^-).

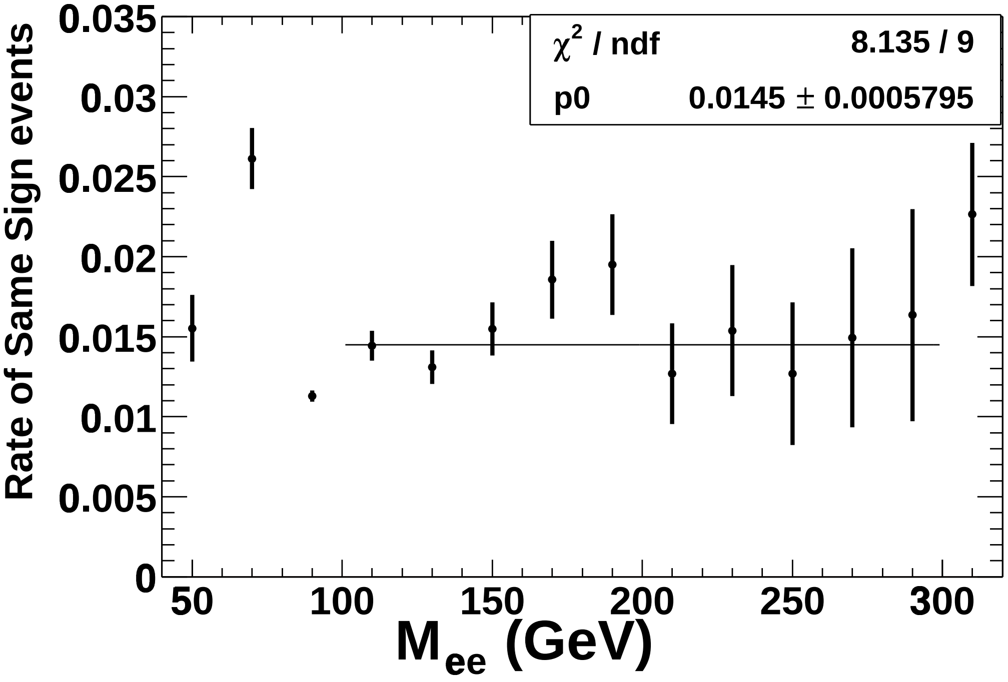

Figure 3.8: *The rate of same sign events as a function of the di-electron invariant mass from the* $Z/\gamma^* \rightarrow e^+e^-$ *Monte Carlo sample. The rate of charge misidentification is half of the same sign event rate. The last bin shows the rate for all events with* $M_{ee} > 300\ GeV/c^2$.

3.8 Charge Dependence of Electron Efficiencies

A systematic bias in the forward-backward asymmetry occurs if the detector response to electrons differs from that to positrons. We compare acceptances and efficiencies between electrons and positrons using the $W^{\pm} \to e^{\pm}\nu$ Monte Carlo and data samples. In Figure 3.9, the number of W^{+} events and the number of W^{-} are plotted as a function of $Q \cdot \eta_{det}$ of electrons. The yield difference between the $Q \cdot \eta_{det} < 0$ region and the $Q \cdot \eta_{det} > 0$ region comes from the intrinsic charge asymmetry between the W^{+} (W^{-}) production in the proton direction and that in the anti-proton direction. Because the average momentum of u ($\bar{u}$) quarks is larger than that of d ($\bar{d}$) quarks in the proton (anti-proton), W^{+} (W^{-}) events are enhanced in the proton (anti-proton) direction. Small differences seen between W^{+} yields (solid histograms) and W^{-} yields (dotted histograms) would be caused by either differences in the detector response between electrons and positrons or an asymmetric z_{vertex} distribution about 0. The latter leads to the observed acceptance difference between electrons and positrons. The average and width of the z_{vertex} distribution from the Gaussian fit are determined from the data and they are $+2.5$ cm and 28 cm, respectively. The effect due to the z_{vertex} distribution is determined by the Monte Carlo simulation (see the difference between the solid and dotted histograms in the top plot in Figure 3.9). Even after the effect of the z_{vertex} offset is taken into account, a small difference between W^{+}

yields and W^- yields remains at a level of 1σ. The impact on the forward-backward charge asymmetry due to this remaining difference is estimated to negligible.

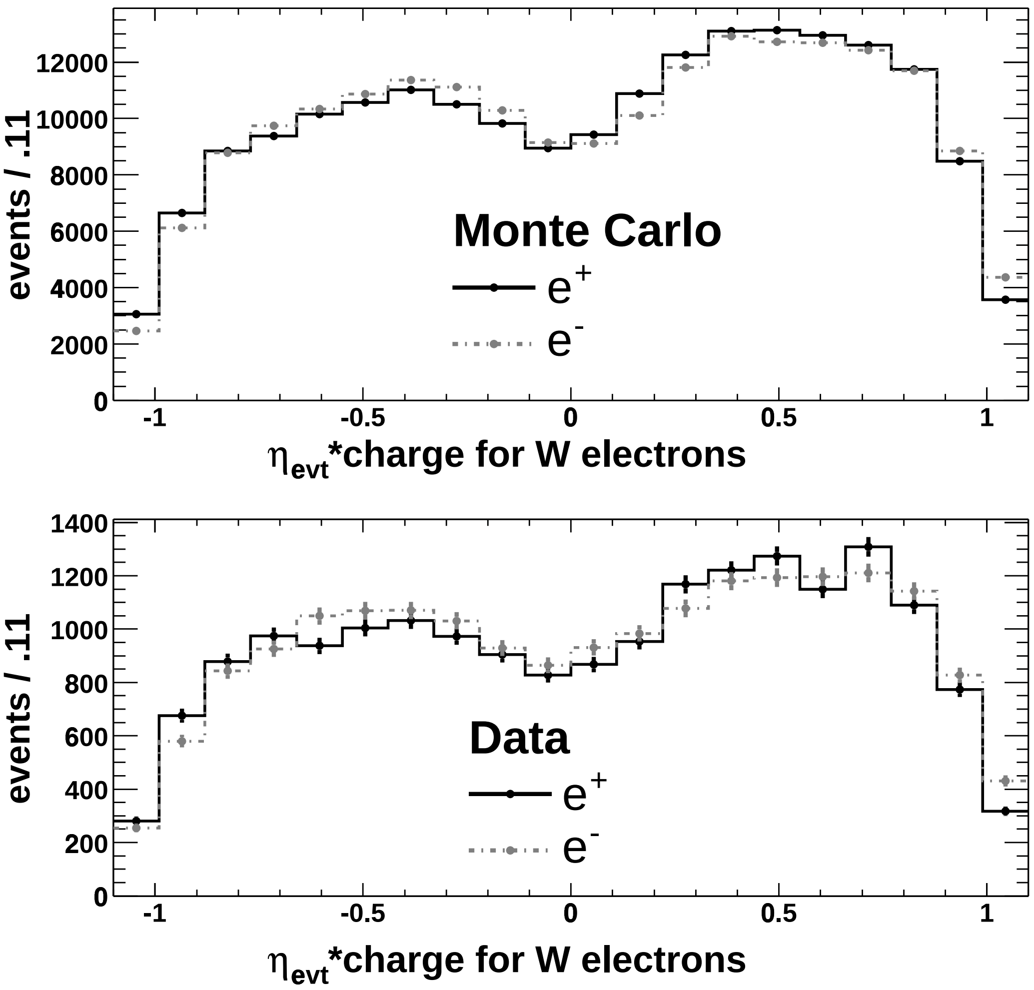

Figure 3.9: *The* $Q \cdot \eta_{evt}$ *of the electons in* W *events. The asymmetry about 0 is due to the charge asymmetry in the* W *production. The difference between* e^+ *and* e^- *is largely due to the asymmetric distribution of the event vertex* (z_{vertex}) *distribution. A* χ^2 *test between the Monte Carlo simulation and data distributions yields* $\chi^2/dof = 30.0/20$.

Chapter 4

Backgrounds

The dominant sources of background to the process $\bar{p}p \rightarrow Z/\gamma^* \rightarrow e^+e^- + X$, where $Z/\gamma^* \rightarrow e^+e^-$, are:

1. Dijets where the jets mimic electrons,
2. $W + X \rightarrow e\nu + X$, where X is a photon or a jet,
3. $Z/\gamma^* \rightarrow \tau^+\tau^- \rightarrow e^+e^-\nu_\tau\nu_e\bar{\nu}_\tau\bar{\nu}_e$,
4. $\mathrm{W}^+\mathrm{W}^- \rightarrow e^+e^- + \nu_e\bar{\nu}_e$,
5. $W^\pm Z$ where $Z \rightarrow e^+e^-$,
6. $t\bar{t} \rightarrow e^+e^-\nu_e\bar{\nu}_e + b\bar{b}$.

The determination of A_{FB} requires knowledge of the background rate and the forward-backward charge asymmetry from each background process. The dijet background is the dominant background for this measurement.

4.1 Dijet Background

The dijet background consists of events with two high p_T jets or events with one jet and one photon. Jets can either contain electrons via semi-leptonic heavy flavor decays or fake electrons. Photons from initial or final state QED radiation are identified as electrons in the plug region and central electrons can be originate from these photons converting into electron-positron pairs. Sources of electron candidates from jets are discussed in section 4.1.1. Forward-backward charge asymmetry of the dijet background is measured in section 4.1.2. In section 4.1.3, the rate of jets faking electrons is measured, resulting in the dijet background estimate. The invariant mass distribution of the dijet background is also extracted. The amount of the dijet background is also cross-checked using same-sign events in the Z/γ^* sample (section 4.1.4).

4.1.1 Sources of electron fakes from dijet Monte Carlo

The dijet Monte Carlo can be used to understand the sources of high p_T electron fakes that are seen in the data. Although the statistics are limited, a rough estimate can be made of the relative contributions from light quarks, heavy quarks, gluons and photons for faking a single high p_T electron. In approximately 750 k dijet events, 47 central tight electrons, 179 central loose electrons, and 1702 plug loose electrons are found. Partons are matched to these fake electrons by looking for the first parton in the event sequence whose direction matches the fake electron, and has at least $E_T > 15$ GeV. The fraction of events found in each category is shown in Figure 4.1. Photons (60% from initial state radiation, and 40% from final state radiation) and light quarks contribute roughly equally for tight electrons, but for the loose electrons the light quarks dominate, especially for plug electrons. Since only a single fake electron is required for this study, relative contributions may change when topological requirements are made on an event.

4.1.2 Charge correlation and A_{FB} distribution of dijet events

The dijet background is expected to have no charge correlation between the two fake electrons. Our assumption is checked using the hadronic-enriched data sample, where both electrons are "jet-like". Events are selected from the electron triggered sample by requiring two electromagnetic clusters that pass the kinematic cuts of our analysis and requiring that there is a significant amount of energy near these clusters (high E_T^{iso}; see Section 3.2). These selection criteria as summarized in Table 4.1 eliminate most of the events from Electroweak processes. An additional cut of $\not{E}_t < 10$ GeV eliminates a large fraction of possible $W \rightarrow e\nu$ contamination in the sample. The sample contains 8595 events where the two electrons have the same charge (same-sign events). In the same sample 8797 opposite-sign events are found. Although the difference is statistically significant (2.2 σ), there are only 2% more events in the opposite-sign sample than in the same-sign sample. This confirms the assumption that the dijet background is nearly charge symmetric, and that the charge

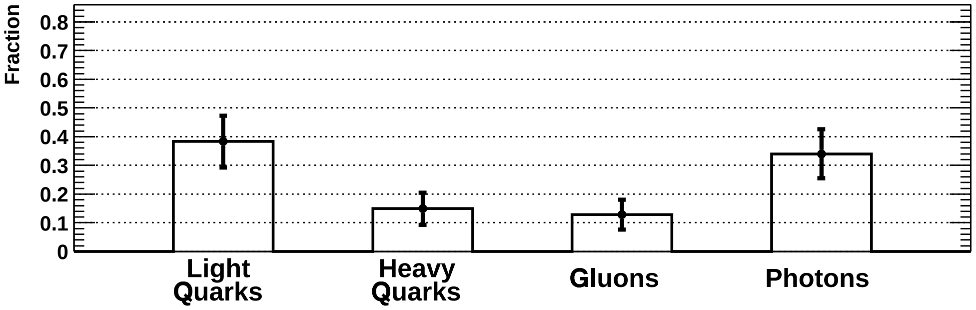

Partons Faking Cental Tight Electrons

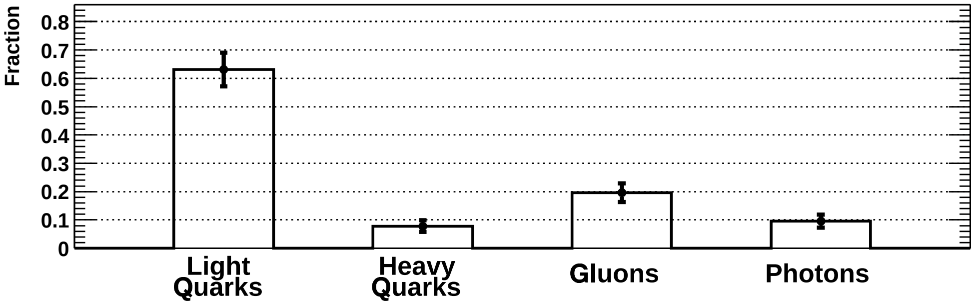

Partons Faking Cental Loose Electrons

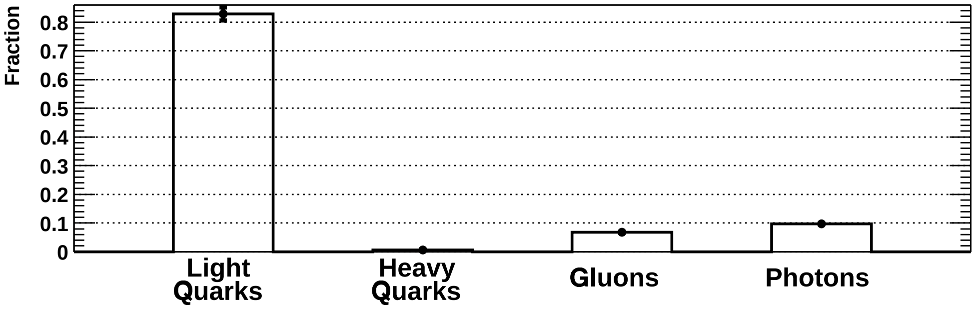

Partons Faking Forward Loose Electrons

Figure 4.1: *Sources of single electron fakes found in Monte Carlo dijet events, and their relative contributions.*

Table 4.1: *Selection criteria to make the hadronic-enriched data sample from the electron trigger sample. This sample is used to check that the dijet background is charge symmetric and forward-backward symmetric.*

Central	Plug
p_T > 10 GeV/c	not applied
$E_T^{corrected} > 20$ GeV	
$E_T^{iso} > 4$ GeV	
$\not{E}_t < 10$ GeV	

of these electrons are not correlated within an event.

Figure 4.2 shows the distributions of A_{FB} for the hadronic-enriched data sample in the 15 mass regions. Although the measured A_{FB} has a few points where the asymmetry is statistically significant, the asymmetry is still small, which is consistent with the symmetric angular distribution expected for dijet events. This analysis uses $A_{FB} = 0$ for the background subtraction and uses the asymmetries in Table 4.2 as a systematic uncertainty.

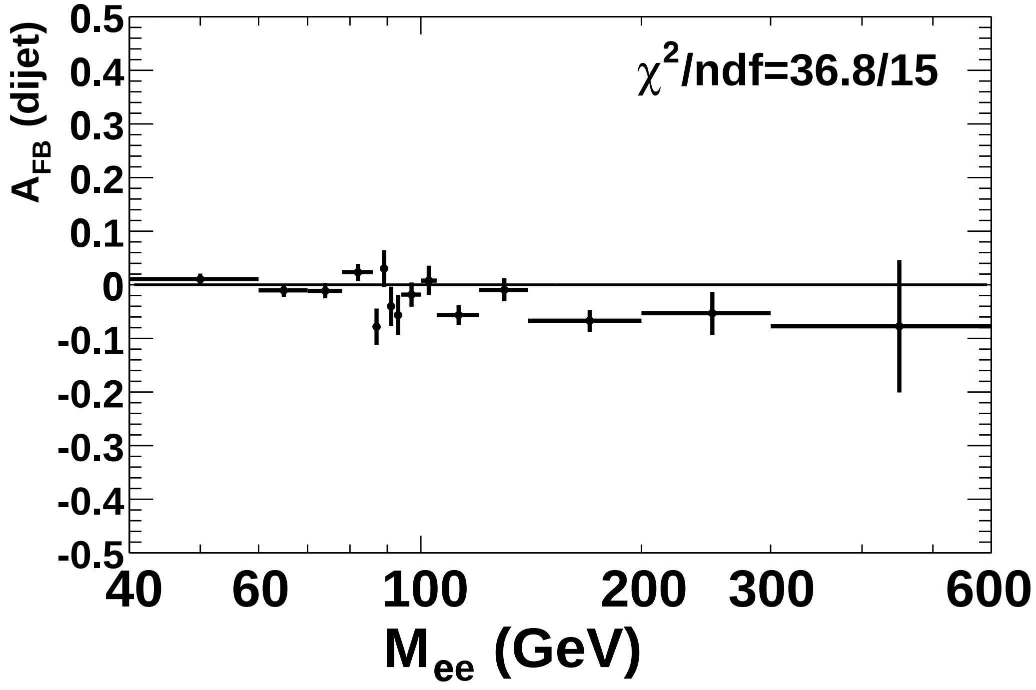

Figure 4.2: *Measured A_{FB} of dijet background, taken from the hadronic-enriched data sample.*

Table 4.2: *The estimated number of events and the measured* A_{FB} *of dijet background in each invariant mass bin. The number of events is estimated using electron fake rates.* A_{FB}*(dijet) is measured from the hadronic-enriched data sample. When calculating* $A_{FB}(Z/\gamma^* \to e^+e^-)$, A_{FB}*(dijet) = 0 is assumed. The measured* A_{FB}*(dijet) is used as a systematic uncertainty for the measurement.*

Mass Region	# Events		A_{FB}(dijet)
	C-C	C-P	
$40 < M_{ee} < 60$ GeV/c^2	9.0	46.4	$+0.01 \pm 0.01$
$60 < M_{ee} < 70$ GeV/c^2	2.5	24.1	-0.01 ± 0.01
$70 < M_{ee} < 78$ GeV/c^2	1.2	13.9	-0.01 ± 0.01
$78 < M_{ee} < 86$ GeV/c^2	0.7	9.6	$+0.02 \pm 0.02$
$86 < M_{ee} < 88$ GeV/c^2	0.1	1.8	-0.08 ± 0.03
$88 < M_{ee} < 90$ GeV/c^2	0.1	1.7	$+0.03 \pm 0.03$
$90 < M_{ee} < 92$ GeV/c^2	0.1	1.5	-0.04 ± 0.04
$92 < M_{ee} < 94$ GeV/c^2	0.1	1.4	-0.06 ± 0.04
$94 < M_{ee} < 100$ GeV/c^2	0.2	3.3	-0.02 ± 0.02
$100 < M_{ee} < 105$ GeV/c^2	0.2	2.1	$+0.01 \pm 0.03$
$105 < M_{ee} < 120$ GeV/c^2	0.3	3.8	-0.06 ± 0.02
$120 < M_{ee} < 140$ GeV/c^2	0.2	2.1	-0.01 ± 0.02
$140 < M_{ee} < 200$ GeV/c^2	0.2	1.4	-0.07 ± 0.02
$200 < M_{ee} < 300$ GeV/c^2	0.0	0.2	-0.05 ± 0.04
$300 < M_{ee} < 600$ GeV/c^2	0.0	0.0	-0.08 ± 0.12

4.1.3 Estimation of dijet background and M_{ee} distribution using electron fake rates.

The fraction of jets which fake elections, the single-jet fake rate, is calculated from the dijet sample. The sample uses 20 GeV single jet triggers. Jets are clustered using the cone size of $\Delta R = \sqrt{(\Delta\eta)^2 + (\Delta\phi)^2} = 0.4$. We require two jets with $E_T > 20$ GeV, missing transverse energy less than 10 GeV, and no more than one loose electron in the event. These requirements ensure that the electroweak contamination from W and Z electron decays is negligible. The fake rate is defined as the fraction of jets in the sample which pass the electron selection criteria. The rate is plotted as a function of the jet E_T in Figure 4.3. Due to the bigger cluster size of jets compared to electrons, jet energies are larger than fake-electron energies. For example, a jet E_T of 25 GeV corresponds to an electron E_T of 20 GeV. The points with $E_T <$ 25 GeV, therefore, are not included in the fit.

The single-jet fake rate is also measured with jets which are not used in trigger decision. For this purpose, jets with $E_T < 45$ GeV in the jet 50 GeV sample (50 GeV single jet triggers) and jets with $E_T < 95$ GeV in the jet 100 GeV sample (100 GeV single jet triggers) are used. In addition, Monte Carlo dijet events without triggers applied are used. Table 4.3 summarizes the rates in the four different samples. The fake rate for jets without trigger biases are roughly a half of the fake rate measured in the 20 GeV dijet sample that contains a mixture of triggered and non-triggered jets. The difference in rates is somewhat expected since the trigger requirements force jets to deposit a significant fraction of their energy into one tower.

The number of background events in the $Z/\gamma^* \rightarrow e^+e^-$ sample is estimated by applying single-jet fake rates to two jets in the 20 GeV dijet sample. We take the single-jet fake rates to be the average single-jet fake rates measured from the 20 GeV dijet sample. The systematic uncertainty in this estimation is determined by taking the simplified case where each event has two and only two jets, one triggered and one non-triggered. If the fake rate for the non-triggered jets is f and the average rate for the triggered and non-triggered jets is $2f$, then the fake rate for the triggered jets is $3f$. The event fake rate is estimated to be $4f^2$ if the average fake rate is applied to both jets, and it is $3f^2$ if the rates for the non-triggered and triggered jets are applied separately. The difference between these two, which corresponds to 25%, is taken as a systematic uncertainty due to the trigger bias.

The invariant mass distribution from the dijet background is determined by the 20 GeV dijet sample where one jet is in the central region and another in the central or plug region. A ratio is taken between the faked electron energy and the jet cluster energy, and a gaussian fit is made of the $\frac{E_T^e}{E_T^{jet}}$ distribution for the three types of

Table 4.3: *The rate at which a jet fakes an electron. The jets in the 20 GeV dijet sample are a mixture of triggered and non-triggered jets. The rate in the 50 GeV and 100 GeV dijet samples is measured only for jets with E_T below the trigger threshold, $E_T < 45(95)$ GeV for the 50 (100) GeV dijet sample.*

	Central Tight Rate ($\times 10^{-4}$)	Central Loose Rate ($\times 10^{-4}$)	Plug Loose Rate ($\times 10^{-4}$)
20 GeV dijet	$2.7 \pm 0.2 \pm 0.7$	$13.7 \pm 0.6 \pm 3.4$	$51.6 \pm 1.0 \pm 12.9$
50 GeV dijet	1.3 ± 0.2	6.5 ± 0.4	30.2 ± 1.2
100 GeV dijet	1.7 ± 0.3	5.5 ± 0.5	27.6 ± 1.8
Monte Carlo	1.3 ± 0.3	7.6 ± 0.9	24.8 ± 3.1

electrons. Jet energies are corrected to represent electron energies using the $\frac{E_T^e}{E_T^{jet}}$ distribution. Figure 4.4 shows the invariant mass distribution of all of the central-central and central-plug events, weighted by the probability that they could fake a dielectron candidate event. Table 4.2 shows the number of dijet events expected in each invariant mass bin. The total number of central-central dijet background candidates is estimated to be 9.0 ± 3 events, and that of central-plug dijet background candidates 128 ± 45 events. The invariant mass distribution of the dijet background along with the Monte Carlo $Z/\gamma^* \rightarrow e^+e^-$ prediction is shown in Figure 7.1.

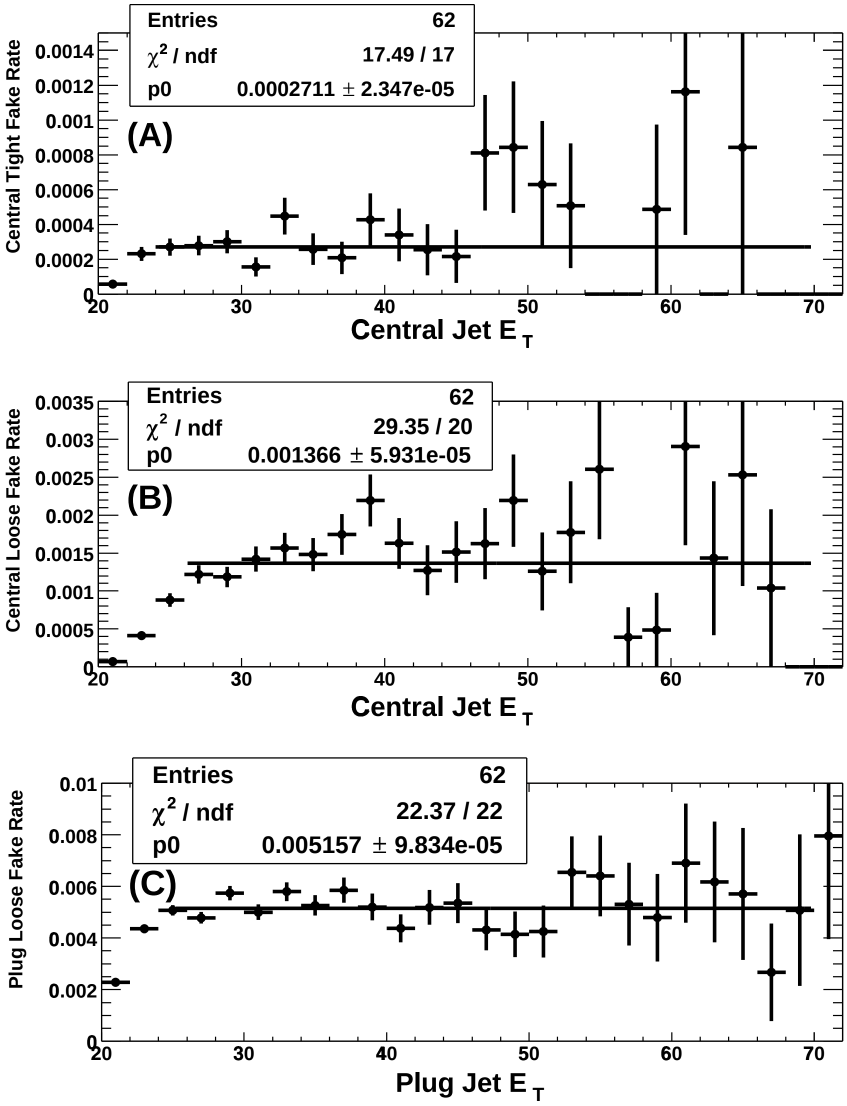

Figure 4.3: *The electron fake rate for central tight (A), central loose (B), and plug loose (C) requirements in the 20 GeV dijet sample. The fake rate is measured for jets above* $E_T^{jet} > 24$ *GeV for central tight and plug loose electrons, and* $E_T^{jet} > 26$ *GeV for central loose electrons to take into account of differences between the jet clustering and the electron clustering.*

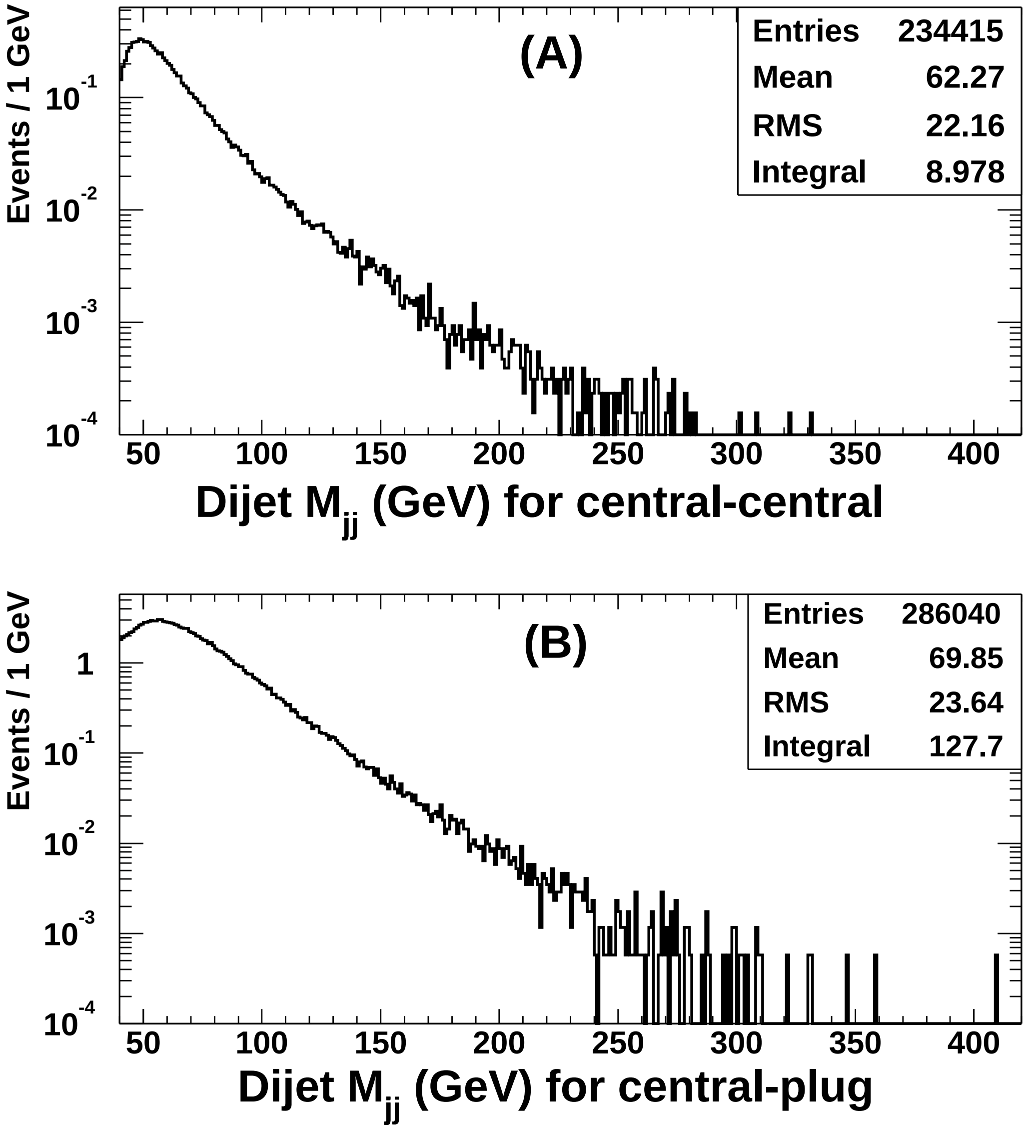

Figure 4.4: *The invariant mass distribution measured in the 20 GeV dijet sample. Event fake rates are applied to these samples.*

4.1.4 Check of dijet background using the charge of the di-electrons

The fact that dijet events are nearly charge symmetric can also be used to estimate the background with the central-central Z/γ^* sample, where charge identification is good for both electrons. If the charges of the two electrons are well measured, the number of same-sign events with electrons that pass all the selection criteria is a good estimate of the dijet background, and this can be used as a check for the dijet background estimation in the central-central topology.

If the charges are not well measured, signal events will contaminate the same-sign sample and lead to an overestimate of the dijet background. The dominant contribution to the charge misidentification of electrons comes from "trident" electrons except at very high energies where the curvature resolution is the dominant source (see section 3.7). The number of same sign $Z/\gamma^* \rightarrow e^+e^-$ events due to "trident" electrons can be estimated from the Monte Carlo simulation. The Monte Carlo samples are normalized such that the number of the opposite sign events in the Z peak is the same between the data and the Monte Carlo simulation. The top plot in Figure 4.5 shows the invariant mass distributions of the data and the Monte Carlo simulation for opposite-signed events and same-signed events. The number of same-sign events in the data is found to be 36, and that in the simulation 23, resulting in the estimation of 13 dijet background events in the central-central topology. The bottom plot shows the invariant mass distribution for the same-signed data events after the Monte Carlo events have been subtracted. The systematic uncertainty of 4 events is estimated by repeating this procedure with the Monte Carlo samples made with various amounts of material. Thus the dijet background in the central-central topology is estimated to be $13 \pm 6(\text{stat.}) \pm 4(\text{syst.})$ events. This is in good agreement with the estimate from the fake rate method.

4.2 Electroweak and Top Backgrounds

The electroweak and top background events are estimated using the Monte Carlo simulation. Table 4.4 shows the theoretical cross-section and the number of events expected in the sample of 72 pb^{-1} for each process. The systematic uncertainties on these background estimates reflect a 6% uncertainty on the integrated luminosity, a 5% uncertainty on the acceptance, and the theoretical uncertainty on the cross section. The events passing selection requirements in each process are used to determine both the invariant mass distribution, and the expected forward-backward asymmetry. The invariant mass distributions for $Z \to \tau^+\tau^-$ and $W + X \to e\nu + X$ are shown in

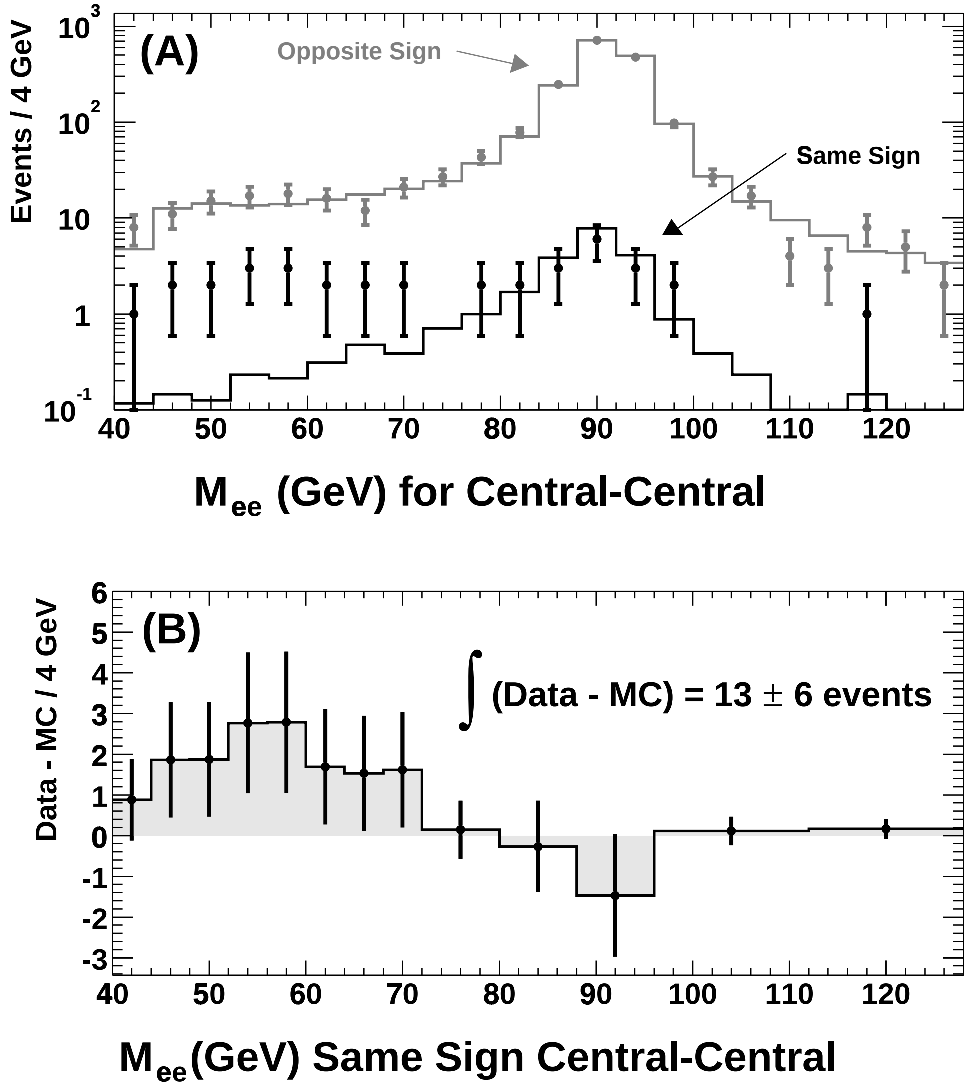

Figure 4.5: *(a) invariant mass distributions of central-central topology data (points) and Monte Carlo events (histogram) where the Monte Carlo sample is normalized to the data using opposite-signed events in the Z peak. (b) invariant mass distribution of central-central topology same-signed data after subtracting the MC distribution.*

Figure 4.6.

The dominant background source is the $W + X \rightarrow e\nu + X$ process where X is a gluon or a photon. Figure 4.7 shows the sources of the faked electrons in the $W + X$ sample, indicating that the dominant source is a photon faking an electron (mostly in the plug region). The number of $W+X$ background events estimated from PYTHIA is 27 ± 5. PYTHIA, using the parton shower algorithms to generate photons and jets, is expected to give lower cross sections than the Standard Model prediction for high p_T photon and jet production. We cross-check the PYTHIA calculation with two NLO matrix element calculations, $W + 1$ parton ALPGEN and $W + 1$ photon WGAMMA. The combination of ALPGEN and WGAMMA estimates the $W + X \rightarrow e\nu + X$ to be 24 ± 3 events, in good agreement with the PYTHIA expectation. The ALPGEN and WGAMMA estimates are used as a systematic uncertainty on the A_{FB}.

Table 4.4: *Summary of expected backgrounds, including cross-sections used for the non-dijet background estimates. Monte Carlo estimates are normalized to* 72 pb^{-1}*. Cross sections are taken from the following references: W, Z [43], Diboson [44], and top [45].*

Process	Generator	$\sigma \cdot BR$ (pb)	Events Expected	
			C-C	C-P
Dijet	Data	N/A	9.0 ± 3	127 ± 45
$W + g/\gamma \rightarrow e\nu + g/\gamma$	PYTHIA	2,690±100	1.8 ± 0.2	25.4 ± 2.4
$Z \rightarrow \tau^+\tau^-$	PYTHIA	251 ±4	5.6 ± 0.5	7.2 ± 0.7
$W^+W^- \rightarrow e^+e^-\nu_e\bar{\nu}_e$	PYTHIA	0.15 ±0.01	1.5 ± 0.1	1.8 ± 0.2
$W^\pm Z$ where $Z \rightarrow e^+e^-$	PYTHIA	0.15 ±0.01	1.4 ± 0.1	1.7 ± 0.2
$t\bar{t} \rightarrow e^+e^-\nu\bar{\nu} + b\bar{b}$	HERWIG	0.08 ±0.01	1.1 ± 0.1	0.7 ± 0.1

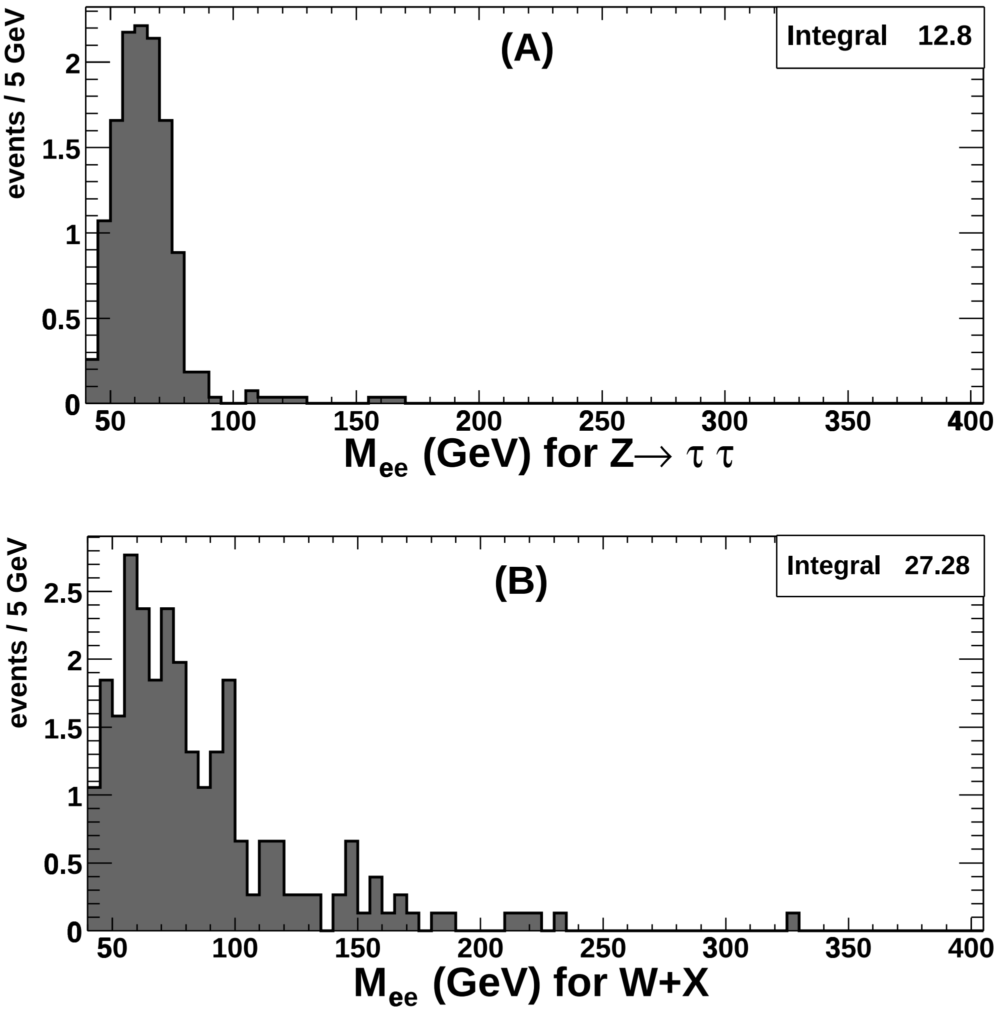

Figure 4.6: *Invariant mass distributions for (A)* $Z/\gamma^* \to \tau^+\tau^-$ *and (B)* $W + X \to e\nu + X$ *(*$X = g$ *or* γ*) backgrounds.*

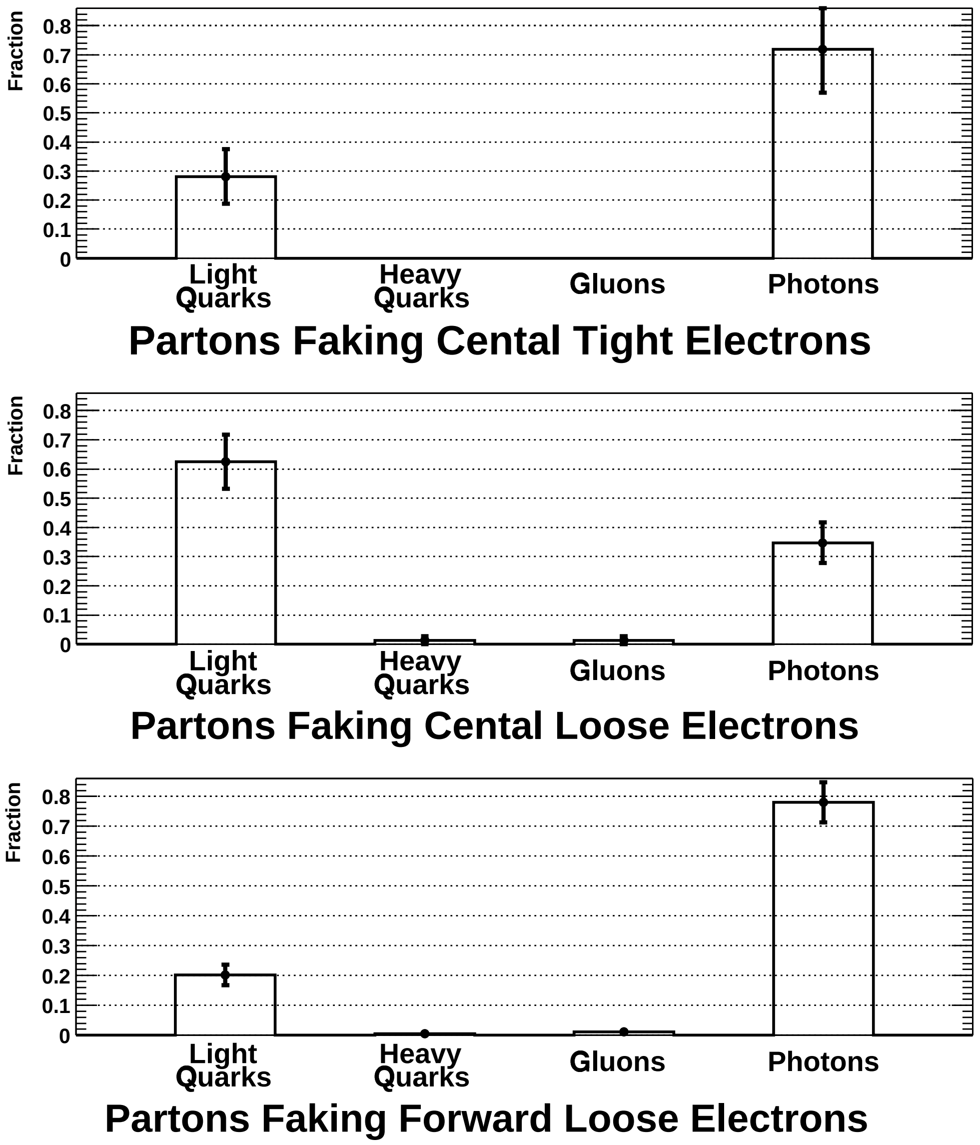

Figure 4.7: *Sources of single electron fakes found in PYTHIA Monte Carlo* $W + X \rightarrow e\nu + X$ *events where* X = *a gluon or a photon. The composition of the fakes is very different from the dijet events (Figure 4.1).*

Chapter 5

Acceptance and corrections

In order to correct the forward-backward asymmetry in Z/γ decays, any detector acceptances and event selection efficiencies that treat forward and backward events differently must be accounted for. Similarly, any sources contributing to the mismeasurement of the dielectron invariant mass must also be accounted for. Although there is very little in the detector and analysis that treats forward and backward events differently, the angular distribution of the events, photonic radiation off of the electron due to either final state radiation (FSR) or external bremsstrahlung, and detector resolution can effectively change the acceptances, the efficiencies, and the mass calculation so that net differences arise for forward and backward events. The combination of all of these effects is defined as $(a_i^{\pm})_{sel}$ in Equation 1.12. Although the simulation is ultimately used to get the correction, generator level distributions are used to separate independent effects (Sections 5.1, 5.2, and 5.3).

5.1 Fiducial and Kinematic Acceptance: $(a_i^{\pm})_{geom}$ and $(a_i^{\pm})_{kin}$

The kinematic and fiducial requirements sculpt the polar angular distribution of the outgoing electrons and positrons, especially in the very forward direction. Although the acceptance for these requirements is nearly symmetric for positive and negative $cos\theta^*$, the initial $cos\theta^*$ distributions are asymmetric, due to the forward-backward charge asymmetry. The distributions shown in Figure 5.1 show this effect for Monte Carlo events prior to the simulation of the detector and radiation effects. The invariant mass range is split into three different regions, the low mass region ($40 < M_{ee} < 78$ GeV/c^2), the Z pole region ($78 < M_{ee} < 105$ GeV/c^2), and the high mass region ($M_{ee} > 105$ GeV/c^2). These are the regions where A_{FB} is roughly at the low extremum, middle point, and high extremum, respectively. When calculating the acceptance for forward and backward events, these distributions are integrated which leads to different acceptances for forward and backward events. For example, the detector has a low acceptance for events with very high $|cos\theta^*|$ because of the polar coverage, and for high mass events, this removes a greater percentage of the forward events than the backward events. The M_{ee} dependence of the fiducial and kinematic acceptance is shown in Figure 5.2, where the forward events have a higher acceptance than the backward events below the Z pole, and vice versa above the Z pole.

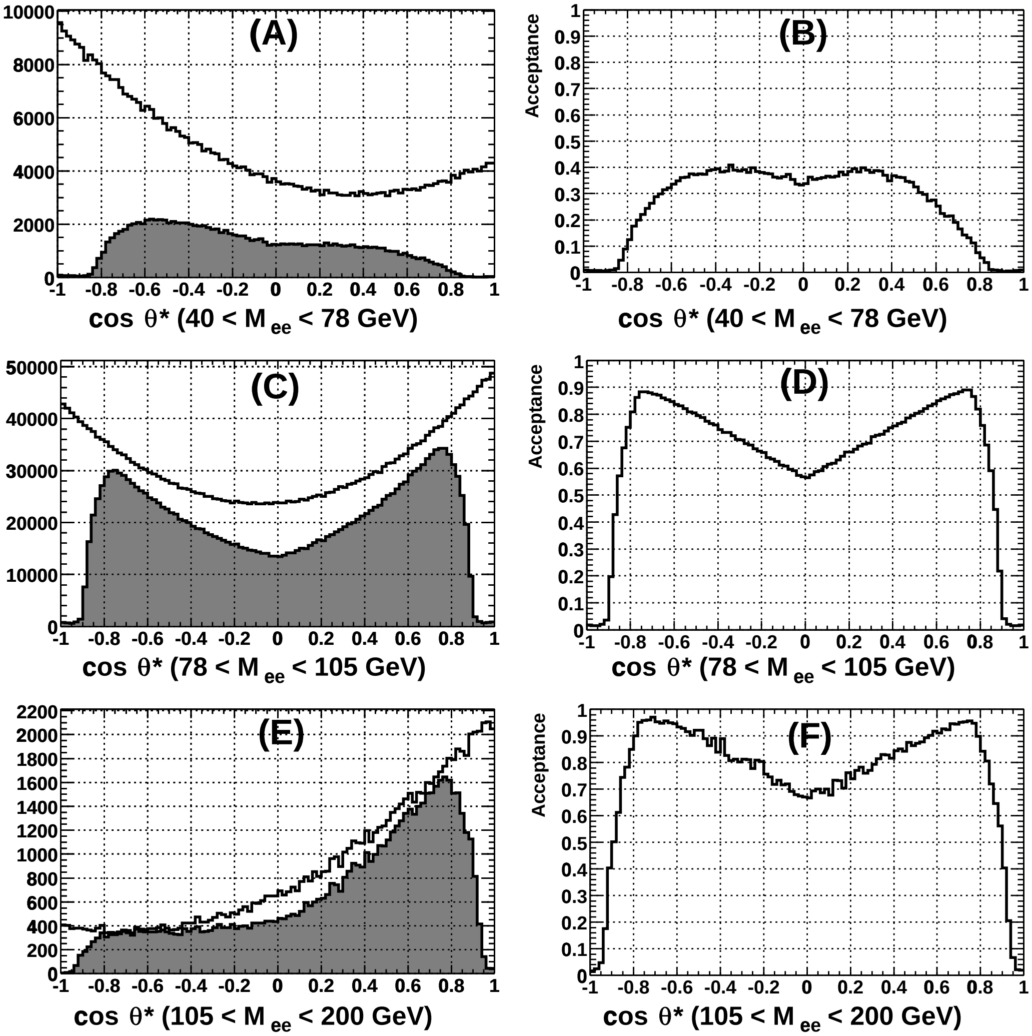

Figure 5.1: *Acceptance for geometric and kinematic* ($(a_i^{\pm})_{geom} * (a_i^{\pm})_{kin}$) *cuts on the* $cos\theta^*$ *distribution for three different mass ranges. The left column (A,C,E) shows the* $cos\theta^*$ *distribution before (empty histogram) and after (filled histogram) the cuts. The right column (B,D,F) shows the acceptance of that cut, by dividing by the total number of events in each bin.*

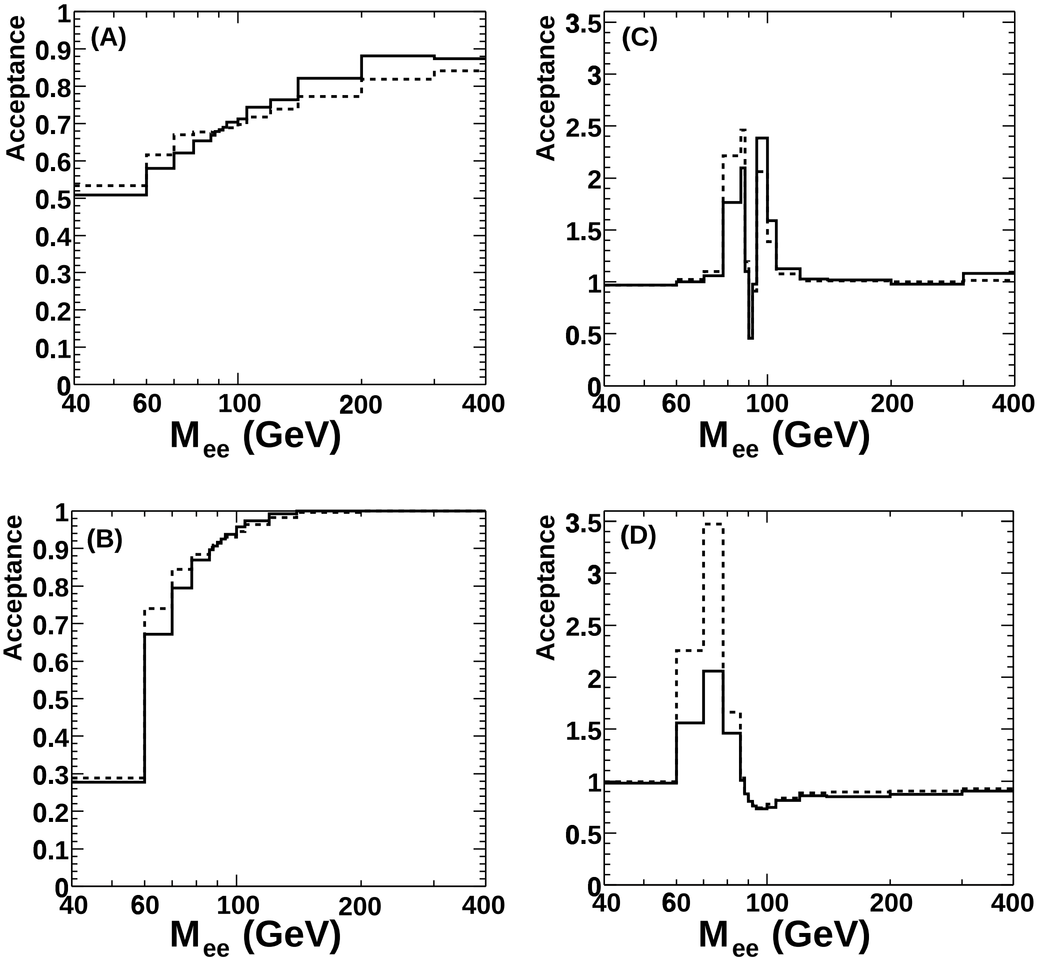

Figure 5.2: *The M_{ee} dependence for each acceptance (A:$(a_i^{\pm})_{geom}$, B:$(a_i^{\pm})_{kin}$ C:$(a_i^{\pm})_{res}$, D:$(a_i^{\pm})_{rad}$). Each acceptance is calculated with the previous acceptance applied. For example, the kinematic acceptance ($(a_i^{\pm})_{kin}$) is shown after having applied geometric cuts, the acceptance due to resolution ($(a_i^{\pm})_{res}$) is shown after having applied geometric and kinematic cuts, and so on. The dashed line is for forward events and the solid line is for backward events.*

5.2 Corrections for Energy Resolution: $(a_i^{\pm})_{res}$

The energy resolution of the calorimeter causes mis-measurements of the invariant mass which can place events in the wrong invariant mass bin. If the asymmetry is changing with the invariant mass, events placed in the wrong invariant mass bin can alter the measured asymmetry in that bin. The effect of the energy resolution on the asymmetry is therefore largest near the Z pole where $\frac{dA_{FB}}{dM_{ee}}$ is largest and the bin sizes are smallest. The effect of the energy resolution on the acceptance is shown in the top-right plot of Figure 5.2. This plot is made by smearing the energy of the electron according to the detector resolution.

5.3 Corrections for Photonic Radiation: $(a_i^{\pm})_{rad}$

The invariant mass can also be mis-measured due to final state QED radiation or external bremsstrahlung. Most of these photons are emitted co-linearly with the electrons, hence tend to fall into the electron towers, in effect recombining the energy of the electron with its radiation products. Photons which are not recombined with electrons in the energy measurement lower the measured invariant mass and can cause a candidate event to land in the wrong invariant mass bin. The effect is expected to be the most significant just below the Z pole. The bottom-right plot of

Figure 5.2 demonstrates the effect of final state QED radiation on the acceptance at the generator level (thus, no external bremsstrahlung is included in this plot), when photons are not recombined with electrons

5.4 Summary

The full simulation is used to calculate the acceptance and efficiency which includes the acceptance for fiducial and kinematic cut, the energy resolution, QED final state radiation, external radiation, and electron selection efficiency. In Figure 5.3 and Table 5.1, the product of acceptances and efficiencies is shown as a function of the invariant mass. This can be compared to the studies done at the generator level for each individual effect (see Figure 5.2). The overall acceptance is lower due to more detailed fiducial cuts and the electron identification efficiencies in the full simulation. Aside from the expected differences, the similarity in the shapes confirm the understanding of the effects noted above and point to sources of systematic uncertainties.

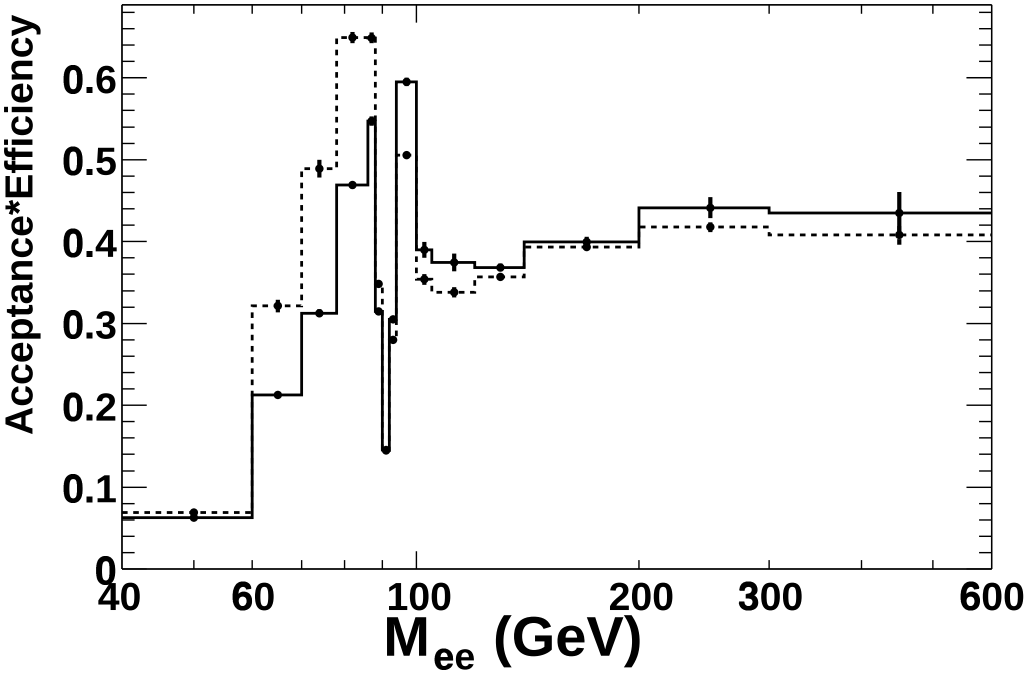

Figure 5.3: *The product of acceptances and efficiencies,* $(a_i^{\pm})_{sel}$*, is defined as the number of forward/backward events passing the cuts divided by the number of forward/backward generator level events in each bin. The generator level events do not include QED FSR. The dashed line is for forward events and the solid line is for backward events.*

Table 5.1: *The product of acceptances and efficiencies,* $(a_i^{\pm})_{sel}$*, for the different mass bins. It is defined as the number of forward/backward events passing the cuts divided by the number of forward/backward generator level events in each bin. The generator level events do not include QED FSR.*

Mass Range	Forward	Backward
$40 < M_{ee} < 60$ GeV/c^2	0.08 ± 0.00	0.07 ± 0.00
$60 < M_{ee} < 70$ GeV/c^2	0.36 ± 0.01	0.25 ± 0.00
$70 < M_{ee} < 78$ GeV/c^2	0.54 ± 0.01	0.36 ± 0.00
$78 < M_{ee} < 86$ GeV/c^2	0.72 ± 0.01	0.53 ± 0.00
$86 < M_{ee} < 88$ GeV/c^2	0.73 ± 0.01	0.60 ± 0.00
$88 < M_{ee} < 90$ GeV/c^2	0.39 ± 0.00	0.35 ± 0.00
$90 < M_{ee} < 92$ GeV/c^2	0.16 ± 0.00	0.16 ± 0.00
$92 < M_{ee} < 94$ GeV/c^2	0.31 ± 0.00	0.33 ± 0.00
$94 < M_{ee} < 100$ GeV/c^2	0.56 ± 0.00	0.66 ± 0.00
$100 < M_{ee} < 105$ GeV/c^2	0.39 ± 0.01	0.43 ± 0.01
$105 < M_{ee} < 120$ GeV/c^2	0.37 ± 0.01	0.40 ± 0.01
$120 < M_{ee} < 140$ GeV/c^2	0.39 ± 0.00	0.40 ± 0.00
$140 < M_{ee} < 200$ GeV/c^2	0.42 ± 0.00	0.43 ± 0.00
$200 < M_{ee} < 300$ GeV/c^2	0.45 ± 0.00	0.46 ± 0.01
$300 < M_{ee} < 600$ GeV/c^2	0.42 ± 0.01	0.44 ± 0.02

Chapter 6

Systematic Uncertainties

The systematic uncertainties in energy scale, energy resolution, the amount of passive material in detector, and the background estimation are considered. For a given source of uncertainty, a change is made in the input value of the simulation, and the impact on the asymmetry is evaluated after that change. The difference between the asymmetry with the changed input and the nominal one is taken as the uncertainty from that source. The change in the input value is either a one standard deviation (1σ) uncertainty on the variable in question or a change in an assumption on that input. The following systematic uncertainties have been investigated and have been found to have a negligible effect on the measurement of A_{FB}: fiducial acceptance, charge mis-assignment, A_{FB}(dijet), and trigger efficiency.

6.1 Systematic Uncertainty from Energy Scale

Variations in the energy scale can cause events to be placed in the wrong invariant mass bin. For example, near the Z pole where the asymmetry is increasing monotonically with respect to the invariant mass, a positive variation in the energy scale will cause a systematic decrease in the asymmetry, and the opposite for a negative variation in the energy scale. In general, a variation in the energy scale will have an effect only in the region where the bins are of the order of the size of the variation or smaller and where the asymmetry is changing. In this analysis, uncertainties due to the energy scale are expected only near the Z pole. Figure 6.1 shows the gaussian peak of the invariant mass as a function of the η_{det} of the electron. Based on the mass variation in this figure, the central calorimeter scale is chosen to vary by 0.5% and the plug calorimeter scale is chosen to vary by 1% to estimate the systematic uncertainty. The fits for the energy scale variations are shown as lines in Figure 6.1. The corresponding shifts in A_{FB} are shown in Table 6.1.

6.2 Systematic Uncertainty from Energy Resolution

Variations in the energy resolution impact the forward-backward charge asymmetry in much the same way as variations in the energy scale. Instead of systematically shifting the events upwards or downwards, they tend to smear the forward-backward charge asymmetry to an average of the bins around the bin in question. For example a positive variation in the resolution near the Z peak will cause a systematic decrease in the asymmetry above the Z peak, and a systematic increase in the asymmetry below the Z peak. As with the energy scale, only narrow bins in the region where the $\frac{dA_{FB}}{dM_{ee}}$ is large will be affected. Figure 6.1 shows the gaussian width of the invariant mass as

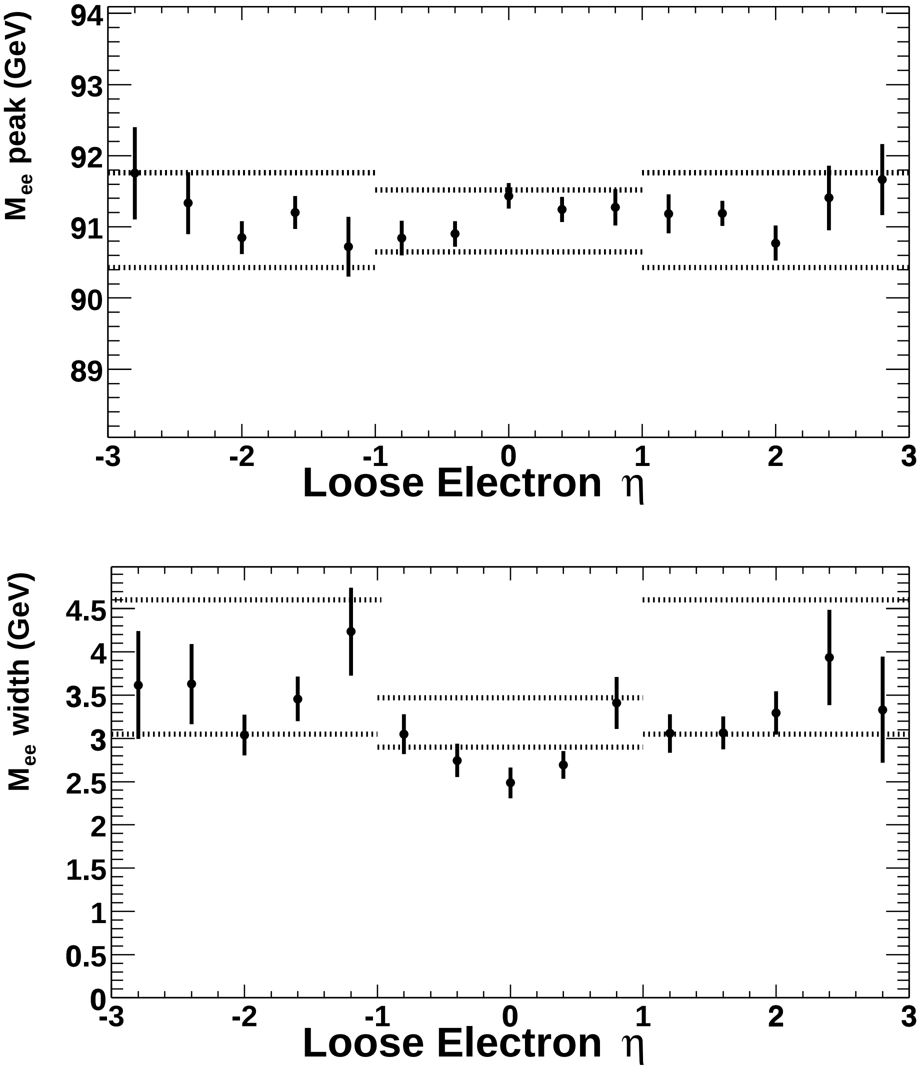

Figure 6.1: *The variation of a gaussian fit to the* M_{ee} *peak between 86 and 98 GeV with loose electron* η_{det}. *(a) The variation in the gaussian peak with the loose electron* η_{det}. *(b) The variation in the gaussian width with loose electron* η_{det}. *The points are the data, and the lines are the shifts in energy and resolution used to get the systematic uncertainty.*

a function of the η_{det} of the electron. Based on the width variation in this figure, the central and plug calorimeter resolutions are chosen to vary such that the width varies by 0.5 GeV in the central calorimeter and 1.5 GeV in the plug calorimeter. The fits for the energy scale and resolution variations are shown as lines in Figure 6.1. The corresponding shifts A_{FB} are shown in Table 6.1.

6.3 Systematic Uncertainty from Amount of Material in Detector

The material before the calorimeters affects the energy measurement of electrons. We estimate that the uncertainty in the amount of material before the tracking volume be less than 1.5% of a radiation length (X_0) and less than $\frac{1}{6}X_0$ in front of the plug calorimeter.

The systematic uncertainty on A_{FB} due to the material is measured by changing the amount of material in the simulation, and then recording the change in A_{FB}. The changes include adding and subtracting an extra $1.5\%X_0$ of copper in a cylinder at 34 cm (just before the COT) and $\frac{1}{6}X_0$ of steel on the face of the plug calorimeter. The corresponding shifts in A_{FB} are shown in Table 6.1. The bins most sensitive to the amount of material are those just below the Z pole.

6.4 Systematic Uncertainty from Background Subtraction

The central values of A_{FB} are calculated after subtracting background events. The number of events is estimated in Section 4. The systematic uncertainty due to the background is taken as shifts in A_{FB} when the estimated numbers of background events are varied by the uncertainty in their number. The corresponding shifts A_{FB} are shown in Table 6.1.

Table 6.1: *Summary of Uncertainties on A_{FB}. When a systematic shift is tested in two directions, the larger shift is chosen, and the sign of the positive shift is shown in the table. The sign of the shift is not used in the measurement of A_{FB}.*

Mass Range ($\mathrm{GeV/c^2}$)	E Scale	E Resolution	Material	Bgrnd	Tot	Stat
40 – 60	0.00 ± 0.01	+0.01 ± 0.01	−0.03 ± 0.03	−0.03	0.05	0.11
60 – 70	0.00 ± 0.01	+0.01 ± 0.01	+0.01 ± 0.03	−0.04	0.05	0.09
70 – 78	−0.01 ± 0.01	+0.01 ± 0.01	−0.01 ± 0.02	−0.01	0.03	0.07
78 – 86	−0.01 ± 0.01	+0.03 ± 0.01	+0.01 ± 0.01	0.00	0.04	0.04
86 – 88	−0.01 ± 0.01	+0.02 ± 0.01	+0.01 ± 0.01	0.00	0.02	0.05
88 – 90	−0.01 ± 0.00	0.00 ± 0.00	+0.01 ± 0.01	0.00	0.02	0.04
90 – 92	+0.01 ± 0.00	+0.01 ± 0.00	−0.01 ± 0.01	0.00	0.01	0.03
92 – 94	−0.01 ± 0.00	−0.00 ± 0.00	−0.01 ± 0.01	0.00	0.01	0.03
94 – 100	−0.01 ± 0.00	−0.02 ± 0.00	−0.01 ± 0.01	0.00	0.03	0.03
100 – 105	−0.02 ± 0.01	−0.09 ± 0.01	−0.04 ± 0.03	0.00	0.10	0.10
105 – 120	−0.01 ± 0.01	−0.02 ± 0.01	+0.02 ± 0.03	+0.01	0.04	0.09
120 – 140	−0.00 ± 0.00	−0.00 ± 0.00	0.00 ± 0.01	0.00	0.01	0.15
140 – 200	−0.00 ± 0.00	0.00 ± 0.00	0.00 ± 0.01	0.00	0.01	0.15
200 – 300	−0.00 ± 0.01	−0.01 ± 0.01	+0.01 ± 0.01	+0.02	0.03	0.22
300 – 600	−0.00 ± 0.02	0.00 ± 0.02	−0.04 ± 0.02	0.00	0.04	0.63

Chapter 7

Results

7.1 Drell-Yan M_{ee} Lineshape and $cos\theta^*$

As a final comparison and cross-check the invariant mass distribution from the data is compared to the signal and background predictions (Figure 7.1). The comparison is also made for the $cos\theta^*$ distribution (Figure 7.2) in three mass regions where A_{FB} is at extremes; $40 < M_{ee} < 75$ GeV/c^2 where A_{FB} is large and negative, $75 < M_{ee} < 105$ GeV/c^2 where A_{FB} is small, and $M_{ee} > 105$ GeV/c^2 where A_{FB} is large and positive. The background events are included using the expected invariant mass and $cos\theta^*$ distributions (as described in section 4). The distributions from the signal Monte Carlo simulation sample are normalized to the number of events in the data after subtracting the expected background contribution. The M_{ee} line shape and the $cos\theta^*$ distribution from the signal and background events agree well with the data.

7.2 The Standard Model Prediction

Currently there are a number of programs that generate Drell-Yan events at a hadron collider. PYTHIA generates events using leading-order (LO) cross sections with initial state QCD radiation and initial and final QED radiation via parton shower algorithms. HERWIG uses LO cross sections with initial state QCD radiation via

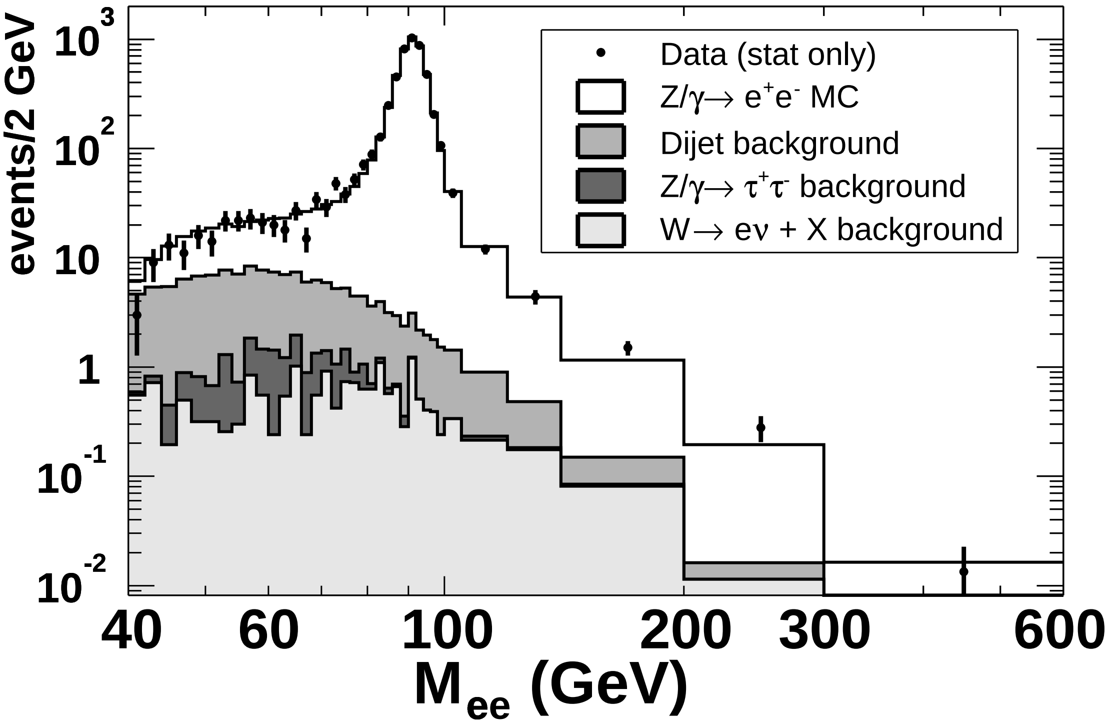

Figure 7.1: *Invariant mass distribution of the data compared to the prediction for the signal and background. The points are the data, the histogram is the signal Monte Carlo sample, and the shaded histrograms are the background predictions.*

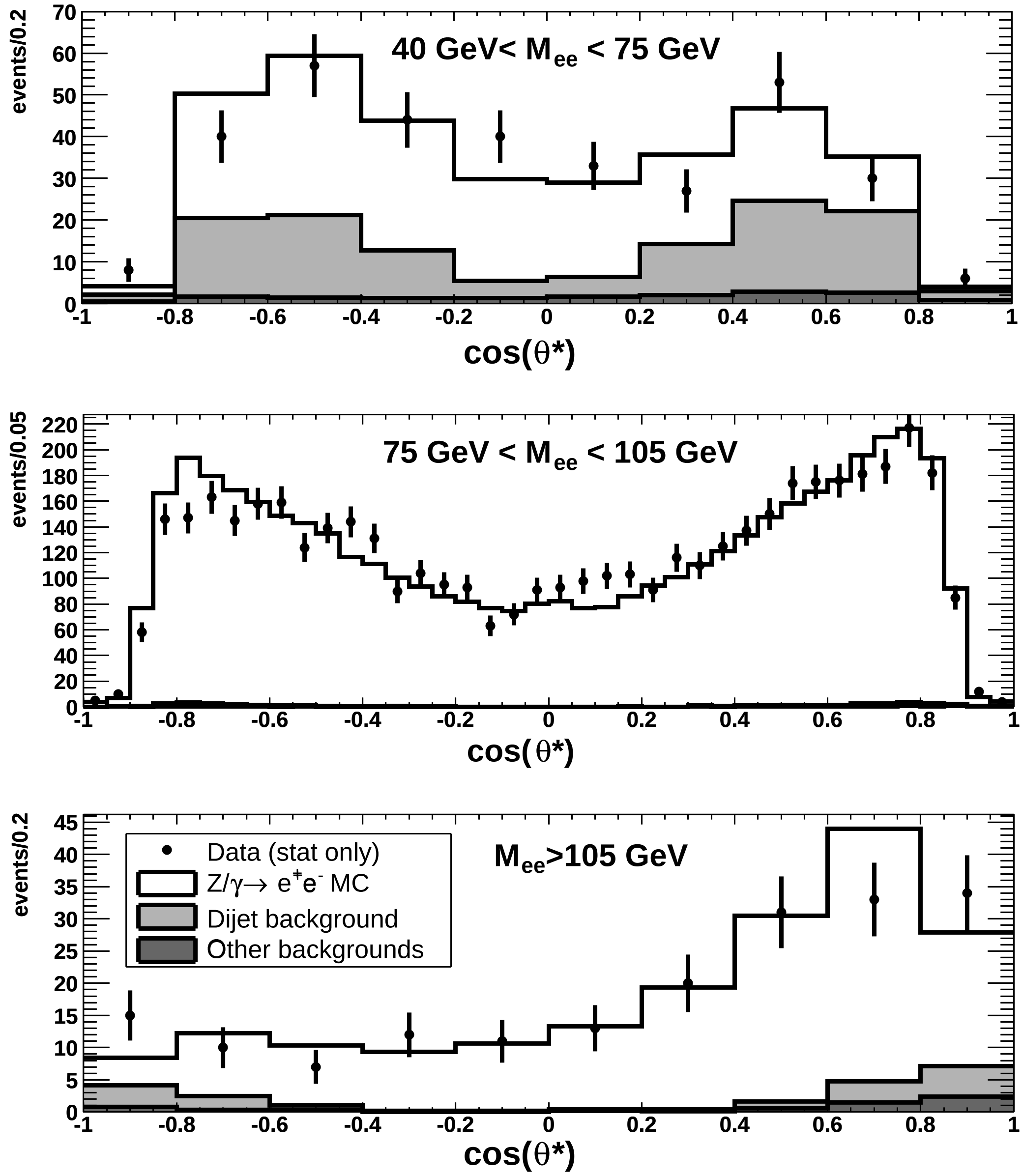

Figure 7.2: *cosθ* distributions for the different mass regions of the data compared to the predictions for the signal and background. The points are the data, the histogram is the signal Monte Carlo sample, and the shaded histrograms are the background predictions.*

Table 7.1: *Summary of observed events and estimated backgrounds in the dielectron sample from 72 pb^{-1} of Run II data.*

	Observed Events		Background	
Mass Range	$cos\theta^* > 0$	$cos\theta^* < 0$	$cos\theta^* > 0$	$cos\theta^* < 0$
$40 < M_{ee} < 60$ GeV/c^2	76	78	37.8 ± 9.8	32.4 ± 9.2
$60 < M_{ee} < 70$ GeV/c^2	46	68	19.0 ± 4.8	17.4 ± 4.6
$70 < M_{ee} < 78$ GeV/c^2	69	98	12.4 ± 2.9	9.9 ± 2.7
$78 < M_{ee} < 86$ GeV/c^2	267	266	8.2 ± 2.1	7.4 ± 2.0
$86 < M_{ee} < 88$ GeV/c^2	246	204	1.4 ± 0.5	1.6 ± 0.4
$88 < M_{ee} < 90$ GeV/c^2	420	393	1.5 ± 0.4	1.3 ± 0.3
$90 < M_{ee} < 92$ GeV/c^2	550	476	1.8 ± 0.4	1.4 ± 0.7
$92 < M_{ee} < 94$ GeV/c^2	481	392	1.4 ± 0.4	1.3 ± 0.3
$94 < M_{ee} < 100$ GeV/c^2	463	325	4.1 ± 1.1	3.1 ± 0.9
$100 < M_{ee} < 105$ GeV/c^2	59	39	2.0 ± 0.6	1.6 ± 0.5
$105 < M_{ee} < 120$ GeV/c^2	67	23	4.1 ± 1.0	3.2 ± 0.9
$120 < M_{ee} < 140$ GeV/c^2	29	15	2.2 ± 1.1	2.2 ± 0.6
$140 < M_{ee} < 200$ GeV/c^2	29	16	3.2 ± 0.6	1.9 ± 0.4
$200 < M_{ee} < 300$ GeV/c^2	11	3	0.6 ± 0.3	0.5 ± 0.3
$300 < M_{ee} < 600$ GeV/c^2	2	0	0.2 ± 0.2	0.0 ± 0.1

parton shower algorithms. ZGRAD [46] includes full $\mathcal{O}(\alpha)$ electroweak corrections but no QCD corrections, resulting in $p_T^{Z/\gamma*} \simeq 0$. The gluon resummation program VBP [47], which does the gluon resummation in the q_t space at low $p_T^{Z/\gamma*}$ and reduces to NLO QCD at high $p_T^{Z/\gamma*}$, does not include any electroweak corrections. Unfortunately there isn't one program that includes both $\mathcal{O}(\alpha)$ electroweak and NLO QCD corrections. A calculation that includes $\mathcal{O}(\alpha)$ electroweak and some QCD corrections can be obtained by running ZGRAD with the parton showering code in PYTHIA. Five calculations are used to estimate the theoretical predictions for the measurement. They are PYTHIA, VBP, ZGRAD, ZGRAD + PYTHIA, and PYTHIA with no QCD corrections, where CTEQ5L is used for the parton distribution functions. The results of the five calculations are shown as a band in Figure 7.3. The uncertainty due to the different corrections is expressed as the width of the band which is determined by the highest and lowest values of A_{FB} in each mass bin. In Figure 7.4, each calculation is compared to the center and width of the band.

7.3 The A_{FB} Measurement

The number of events in various invariant mass bins between 40 GeV/c^2 and 600 GeV/c^2 are summarized in Table 7.1. The A_{FB} measurements are corrected for

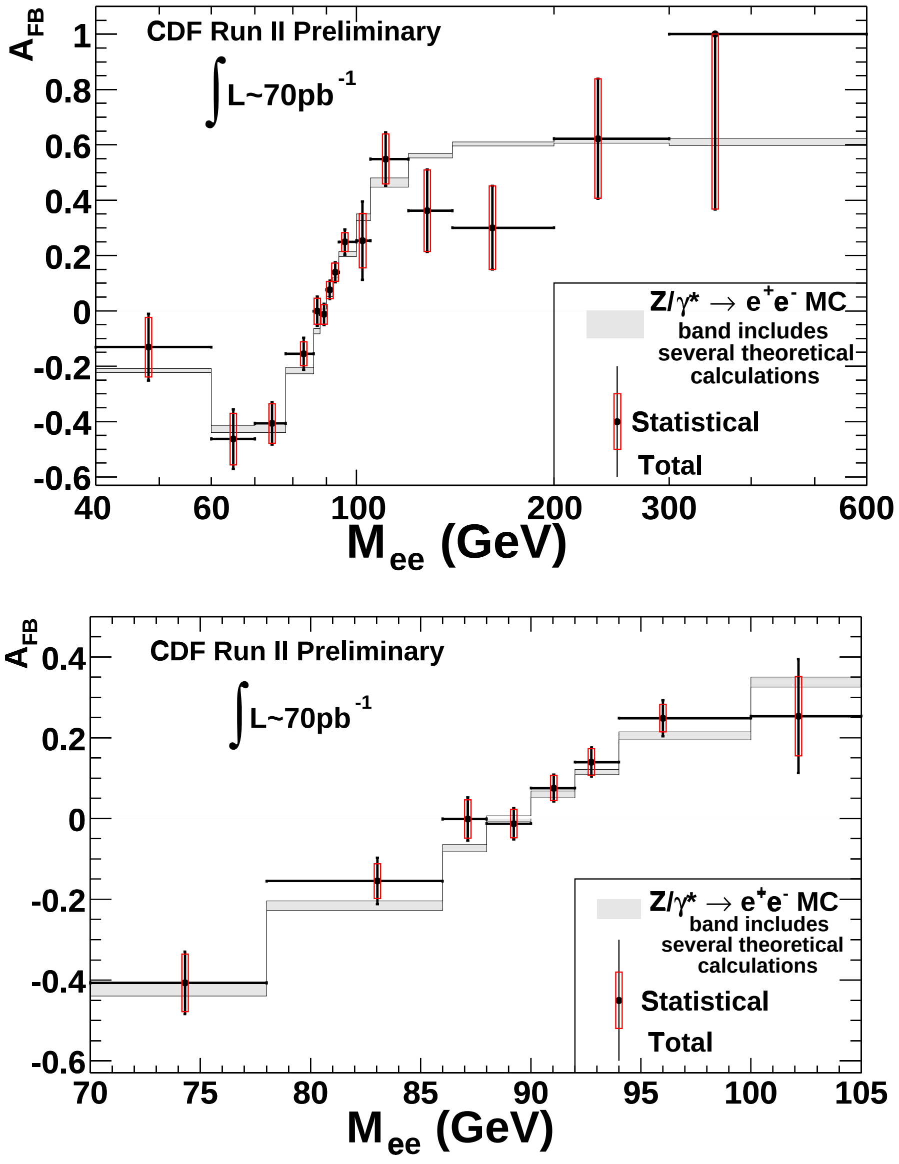

Figure 7.3: *Experimental results for* A_{FB} *with statistical and systematic uncertainties (crosses), and theoretical predictions based on five independent calculations as described in section 7.2 (bands). The measured* A_{FB} *values are corrected for acceptance, efficiency, resolution, and QED radiation.*

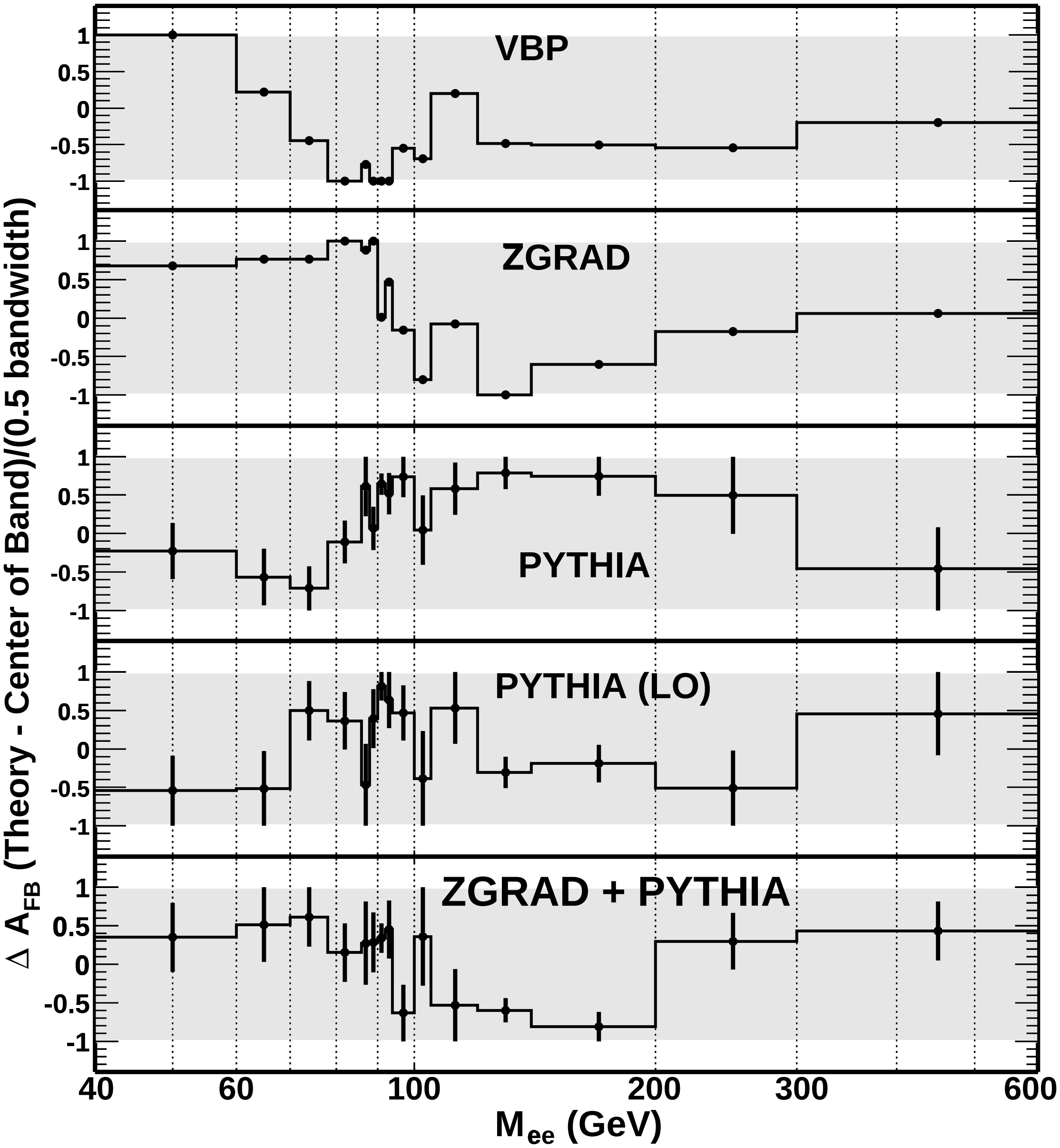

Figure 7.4: *Each of five theoretical calculations compared to the center and width of the theoretical bands.*

Table 7.2: *Experimental results for A_{FB} with statistical and systematic uncertainties, and predictions from PYTHIA with CTEQ5L. The uncertainties with PYTHIA predictions are MC statistical errors. The measured A_{FB} values are corrected for acceptance, efficiency, resolution, and QED radiation. $< M_{ee} >$ is the cross-section weighted average of the invariant mass in each bin.*

Mass Range (GeV/c^2)	$< M_{ee} >$ (GeV/c^2)	Measured A_{FB}	PYTHIA A_{FB}
$40 < M_{ee} < 60$	48.2	$-0.131 \pm 0.108 \pm 0.048$	-0.214 ± 0.003
$60 < M_{ee} < 70$	64.9	$-0.463 \pm 0.094 \pm 0.048$	-0.420 ± 0.005
$70 < M_{ee} < 78$	74.3	$-0.407 \pm 0.071 \pm 0.028$	-0.410 ± 0.005
$78 < M_{ee} < 86$	83.0	$-0.155 \pm 0.043 \pm 0.038$	-0.214 ± 0.003
$86 < M_{ee} < 88$	87.1	$-0.001 \pm 0.048 \pm 0.024$	-0.079 ± 0.004
$88 < M_{ee} < 90$	89.2	$-0.013 \pm 0.035 \pm 0.016$	-0.001 ± 0.002
$90 < M_{ee} < 92$	91.0	$+0.076 \pm 0.031 \pm 0.012$	$+0.054 \pm 0.001$
$92 < M_{ee} < 94$	92.8	$+0.140 \pm 0.033 \pm 0.014$	$+0.112 \pm 0.002$
$94 < M_{ee} < 100$	96.0	$+0.249 \pm 0.034 \pm 0.029$	$+0.198 \pm 0.003$
$100 < M_{ee} < 105$	102.2	$+0.254 \pm 0.098 \pm 0.101$	$+0.338 \pm 0.006$
$105 < M_{ee} < 120$	110.7	$+0.549 \pm 0.090 \pm 0.036$	$+0.454 \pm 0.006$
$120 < M_{ee} < 140$	128.2	$+0.362 \pm 0.148 \pm 0.010$	$+0.554 \pm 0.002$
$140 < M_{ee} < 200$	161.2	$+0.300 \pm 0.151 \pm 0.011$	$+0.598 \pm 0.002$
$200 < M_{ee} < 300$	233.6	$+0.622 \pm 0.216 \pm 0.030$	$+0.609 \pm 0.004$
$300 < M_{ee} < 600$	352.4	$+1.000 \pm 0.632 \pm 0.042$	$+0.616 \pm 0.007$

acceptance, efficiency, resolution and QED radiation. The measurements and the predictions from PYTHIA using CTEQ5L parton distribution functions are listed in Table 7.2, and the measurements are compared with the Standard Model theoretical calculations (see section 7.2) in Figure 7.3.

7.4 Conclusions

We report a measurement of the forward-backward charge asymmetry A_{FB} of electron pairs resulting from the process $\bar{p}p \rightarrow Z/\gamma^* + X$ where $Z/\gamma^* \rightarrow e^+e^-$. The data are collected with the CDF Run II detector between March 2002 and January 2003, corresponding to about 72 pb^{-1}. The experimental results are consistent with the predictions from the Standard Model.

Bibliography

[1] S. L. Glashow, Nucl. Phys. **22**, 579 (1961).

[2] A. Salam, *Proceedings of the VIII Nobel Symposium*, N. Svartholm, ed. (Almquist and Wiksells, Stockholm, 1968), p.367.

[3] S. Weinberg, Phys. Rev. Lett. **19**, 1264 (1967).

[4] F. J. Hasert *et al.* [Gargamelle Neutrino Collaboration], Phys. Lett. B **46**, 138 (1973).

[5] A. C. Benvenuti *et al.*, Phys. Rev. Lett. **32**, 800 (1974).

[6] M. Holder *et al.*, Phys. Lett. B **71**, 222 (1977).

[7] P. B. Renton, Rept. Prog. Phys. **65**, 1271 (2002) [arXiv:hep-ph/0206231].

[8] The LEP Collaborations ALEPH, DELPHI, L3, OPAL, the LEP Electroweak Working Group, and the SLD Heavy Flavour and Electroweak Groups, LEPEWWG/2003-02, December 4, 2003, [arXiv:hep-ex/0312023].

[9] S.D. Drell and T.-M. Yan, Phys. Rev. Lett **25**, 316, 902(E) (1970); Ann. Phys. (N.Y.) **66**, 578 (1971).

[10] D.J.E. Callaway, Ann. Phys. **144**, 1982 (1982); Phys. Lett. **B108**, 421 (1982).

[11] CDF Collaboration, T. Affolder *et al.*, Phys. Rev. Lett. **87**, 131802 (2001) [arXiv:hep-ex/0106047].

[12] M. S. Chanowitz, Phys. Rev. D **66**, 073002 (2002) [arXiv:hep-ph/0207123]; [arXiv:hep-ph/0304199].

[13] G. P. Zeller *et al.* [NuTeV Collaboration], Phys. Rev. Lett. **88**, 091802 (2002) [Erratum-ibid. **90**, 239902 (2003)] [arXiv:hep-ex/0110059].

[14] R. Barate *et al.* [ALEPH Collaboration], Phys. Lett. B **565**, 61 (2003) [arXiv:hep-ex/0306033].

[15] S. Davidson, S. Forte, P. Gambino, N. Rius and A. Strumia, JHEP **0202**, 037 (2002) [arXiv:hep-ph/0112302].

[16] H. Georgi and S. L. Glashow, Phys. Rev. Lett. **32**, 438 (1974).

[17] H. Georgi in *P*roceedings of the 1974 Williamsburg DPF Meeting, ed. by C.E. Carlson (New York, AIP, 1975) p.575; H. Fritzch and P.Minkowski, Ann.Phys. (N.Y.) **93**,192 (1975).

[18] J. L. Hewett and T. G. Rizzo, Phys. Rept. **183**, 193 (1989).

[19] A. Leike, Phys. Rept. **317**, 143 (1999) [arXiv:hep-ph/9805494].

[20] J. L. Rosner, Phys. Rev. D **54**, 1078 (1996) [arXiv:hep-ph/9512299].

[21] D. M. Ghilencea, L. E. Ibanez, N. Irges and F. Quevedo, JHEP **0208**, 016 (2002) [arXiv:hep-ph/0205083].

[22] R. S. Chivukula and J. Terning, Phys. Lett. B **385**, 209 (1996) [arXiv:hep-ph/9606233].

[23] N. Arkani-Hamed, A. G. Cohen, E. Katz, A. E. Nelson, T. Gregoire and J. G. Wacker, JHEP **0208**, 021 (2002) [arXiv:hep-ph/0206020];

[24] N. Arkani-Hamed, A. G. Cohen, E. Katz and A. E. Nelson, JHEP **0207**, 034 (2002) [arXiv:hep-ph/0206021].

[25] T. Han, H. E. Logan, B. McElrath and L. T. Wang, Phys. Rev. D **67**, 095004 (2003) [arXiv:hep-ph/0301040].

[26] Collins and Soper, Phys. Rev. D **16**, 2219 (1977).

[27] CDF Collaboration, F. Abe *et al.*, Nuclear Instrum. Methods Phys. Res. A, **271**, 387 (1988).

[28] CDF Collaboration, F. Abe *et al.* Phys. Rev. D **50**, 2966 (1994).

[29] CDF II Collaboration (1996), FERMILAB-PUB-96-390-E

[30] K. T. Pitts *et al.* (1996), FERMILAB-CONF-96-443-E

[31] L. Balka *et al.*, Nucl. Instrum. Methods Phys. Res. A **267**, 272 (1998); S. R. Hahn *et al., ibid.* **267**, 351 (1998); K. Yasuoka *et al., ibid.* **267**, 315 (1998); R. G. Wagner *et al., ibid.* **267**, 330 (1998); T. Devlin *et al., ibid.* **267**, 24 (1998); S. Bertolucci *et al., ibid.* **267**, 301 (1998).

[32] P. de Barbaro *et al.*, IEEE Trans. Nucl. Sci. **42**, 510 (1995).

[33] B. L. Winer, Int. J. Mod. Phys. A **16S1C**, 1169 (2001).

[34] K. Anikeev *et al.*, Comput. Phys. Commun. **140**, 110 (2001).

[35] T. Sjostrand, P. Eden, C. Friberg, L. Lonnblad, G. Miu, S. Mrenna and E. Norrbin, Comput. Phys. Commun. **135**, 238 (2001) [arXiv:hep-ph/0010017].

[36] G. Corcella *et al.*, JHEP **0101**, 010 (2001) [arXiv:hep-ph/0011363]; arXiv:hep-ph/0210213.

[37] H. L. Lai *et al.* [CTEQ Collaboration], Eur. Phys. J. C **12**, 375 (2000) [arXiv:hep-ph/9903282].

[38] T. Affolder *et al.* [CDF Collaboration], Phys. Rev. Lett. **84**, 845 (2000) [arXiv:hep-ex/0001021].

[39] U. Baur and E. L. Berger, Phys. Rev. D **41**, 1476 (1990).

[40] M. L. Mangano, M. Moretti, F. Piccinini, R. Pittau and A. D. Polosa, JHEP **0307**, 001 (2003) [arXiv:hep-ph/0206293].

[41] E. J. Thomson *et al.*, IEEE Trans. Nucl. Sci. **49**, 1063 (2002).

[42] K. Yasuoka, S. Mikamo, T. Kamon and A. Yamashita [CDF NW Wedge Group Collaboration], Nucl. Instrum. Meth. A **267**, 315 (1988).

[43] A. D. Martin *et al.*, Phys. Lett. B **531**, 216 (2002).

[44] J. M. Campbell and R. K. Ellis, Phys. Rev. D **60**, 113006 (1999) [arXiv:hep-ph/9905386].

[45] M. Cacciari, S. Frixione, M. L. Mangano, P. Nason and G. Ridolfi, [arXiv:hep-ph/0303085]; R. Bonciani, S. Catani, M. L. Mangano and P. Nason, Nucl. Phys. B **529**, 424 (1998) [arXiv:hep-ph/9801375]; S. Catani, M. L. Mangano, P. Nason and L. Trentadue, Phys. Lett. B **378**, 329 (1996) [arXiv:hep-ph/9602208].

[46] U. Baur, O. Brein, W. Hollik, C. Schappacher and D. Wackeroth, Phys. Rev. D **65**, 033007 (2002) [arXiv:hep-ph/0108274].

[47] R. K. Ellis and S. Veseli, Nucl. Phys. B **511**, 649 (1998) [arXiv:hep-ph/9706526]; R. K. Ellis, D. A. Ross and S. Veseli, Nucl. Phys. B **503**, 309 (1997) [arXiv:hep-ph/9704239].

[48] K. Hagiwara *et al.* [Particle Data Group Collaboration], Phys. Rev. D **66**, 010001 (2002)[http://pdg.lbl.gov/].